



DEPARTMENT OF INFORMATICS

TECHNISCHE UNIVERSITÄT MÜNCHEN

Master Thesis in Informatics

Out-of-distribution Detection with Energy-based Models

Sven Elflein





DEPARTMENT OF INFORMATICS

TECHNISCHE UNIVERSITÄT MÜNCHEN

Master Thesis in Informatics

Out-of-distribution Detection with Energy-based Models

Anomalieerkennung mit Energy-based Models

Author:	Sven Elflein
Supervisor:	Prof. Dr. Stephan Günnemann
Advisor:	M. Sc. Daniel Zügner, M. Sc. Bertrand Charpentier
Submission Date:	15. August 2021



I confirm that this master thesis in informatics is my own work and I have documented all sources and material used.

Munich, 15. August 2021

Sven Elflein

Abstract

Today, deep learning is increasingly applied in security-critical situations such as autonomous driving and medical diagnosis. Despite its success, the behavior and robustness of deep networks are not fully understood yet, posing a significant risk.

In particular, researchers recently found that neural networks are overly confident in their predictions, even on data they have never seen before. To tackle this issue, one can differentiate two approaches in the literature. One accounts for uncertainty in the predictions, while the second estimates the underlying density of the training data to decide whether a given input is close to the training data, and thus the network is able to perform as expected.

For the latter approach, Energy-based models (EBMs) can be used as density estimators. EBMs are freely specified by a single function mapping from the data domain to a single value. This allows the usage of existing, powerful classification architectures.

In this thesis, we investigate the capabilities of EBMs at the task of fitting the training data distribution to perform detection of out-of-distribution (OOD) inputs. For evaluation, we consider tabular as well as image data. We find that on most datasets, vanilla EBMs do not inherently outperform other density estimators at detecting OOD data despite their flexibility. Thus, we additionally investigate the effects of supervision, dimensionality reduction, and architectural modifications on the performance of EBMs.

Further, we propose Energy-Prior Network (EPN) which enables estimation of various uncertainties within an EBM for classification, bridging the gap between two approaches for tackling the OOD detection problem, i.e., fitting the data distribution and uncertainty estimation. We achieve this by identifying a connection between the concentration parameters of the Dirichlet distribution of a Dirichlet Prior Network (DPN) and the joint energy in an EBM. Additionally, this allows optimization without a held-out OOD dataset, which might not be available or costly to collect in some applications. Finally, we empirically demonstrate that Energy-Prior Network (EPN) is able to detect OOD inputs, datasets shifts, and adversarial examples while preserving good performance at the classification task. Theoretically, EPN offers favorable properties for the asymptotic case when inputs are far from the training data.

Kurzfassung

Deep Learning wird heute zunehmend in sicherheitskritischen Situationen wie dem autonomen Fahren und der medizinischen Diagnose eingesetzt. Jedoch ist dessen Verhalten und Robustheit noch nicht vollständig verstanden, was ein erhebliches Risiko darstellt.

Erst kürzlich haben Forscher herausgefunden, dass neuronale Netze übermäßige Konfidenz bei ihren Vorhersagen zeigen, selbst bei Daten, die sie zuvor noch nie gesehen haben. Um dieses Problem zu lösen, werden in der Literatur zwei Ansätze unterschieden. Der eine berücksichtigt die Unsicherheit bei der Vorhersage eines neuronalen Netzes, während der Zweite eine Wahrscheinlichkeitsverteilung über die Trainingsdaten approximiert, um zu entscheiden, ob eine Eingabe ähnlich zu den Trainingsdaten ist und das Netz somit die erwartete Leistung erbringen kann.

Für den letzteren Ansatz können Energy-based model (EBM) als Dichteschätzer verwendet werden. EBMs werden frei durch eine einzelne Funktion spezifiziert, die von den Daten auf ein Skalar abbildet. Diese Flexibilität ermöglicht die Nutzung bestehender, leistungsfähiger Architekturen von neuronalen Netzen.

In dieser Arbeit untersuchen wir EBMs und deren Fähigkeit der Erkennung von anomalen (OOD) Eingaben. Wir stellen fest, dass EBMs, trotz ihrer Flexibilität, nicht per se besser als andere Dichteschätzer bei der Erkennung von OOD-Daten funktionieren. Daher untersuchen wir zusätzlich den Fall, dass annotierte Daten zur Verfügung stehen, sowie die Auswirkungen von Dimensionsreduktion und Änderungen an der Netzwerk-Architektur auf die Leistung von EBMs.

Des Weiteren präsentieren wir Energy-Prior Network (EPN), das die Schätzung verschiedener Unsicherheiten innerhalb eines EBM ermöglicht und damit eine Brücke zwischen zwei Ansätzen zur OOD-Erkennung schlägt. Wir erreichen dies, indem wir eine Verbindung zwischen den Konzentrationsparametern der Dirichlet-Verteilung und der Energy in einem EBM identifizieren. Dieses Erkenntnis ermöglicht die Optimierung ohne einen OOD Datensatz, der in manchen Anwendungen nicht verfügbar oder teuer zu beschaffen wäre. Schlussendlich zeigen wir mit Experimenten, dass EPN in der Lage ist, diverse OOD-Eingaben zu erkennen. Weiterhin zeigen wir, dass EPN günstige theoretische Eigenschaften für den asymptotischen Fall von Eingaben weit entfernt von den Trainingsdaten, aufweist.

Contents

Abstract	iii
Kurzfassung	iv
1. Introduction	1
1.1. Problem statement	2
1.2. Related Work	2
2. Background	5
2.1. Classification	5
2.2. Uncertainty Estimation	5
2.2.1. Monte Carlo Dropout	6
2.2.2. Deep Ensemble	7
2.2.3. Dirichlet-based Models	7
2.2.4. Uncertainty measures.	10
2.3. Density Estimation	11
2.3.1. Normalizing Flows	11
2.3.2. Energy-based Models	13
2.3.3. Energy-based out-of-distribution detection	16
3. Method	18
3.1. Derivation of Joint View	18
3.2. Energy-PriorNet	19
3.2.1. Training	21
3.2.2. Properties of Energy-Prior Network	24
3.2.3. Enforcing asymptotic behavior	26
4. Results	28
4.1. Evaluation of Energy-Prior Network	28
4.1.1. Toy Dataset	28
4.1.2. Out-of-distribution detection	31
4.1.3. Detecting dataset shifts	35
4.1.4. Detecting adversarial examples	36
4.1.5. Classifier Evaluation	38
4.1.6. Ablations	40
4.1.7. Conclusion	40

4.2. Investigation of OOD Detection with EBMs	40
4.2.1. Are EBMs better than baselines in general?	41
4.2.2. Does supervision improve OOD detection?	42
4.2.3. Can we encourage semantic features?	46
4.2.4. Low-level features in EBMs	47
4.2.5. Conclusion	49
5. Conclusion	50
5.1. Summary	50
5.2. Future Work	50
A. General Addenda	52
A.1. Proof of Theorem 1	52
A.2. Training details	53
A.2.1. Implementation & Configuration	55
A.3. Additional results	55
A.4. Other directions	60
A.4.1. Noise Contrastive Estimation for Energy-based model training	60
A.4.2. Role of transformation in Normalizing Flows for out-of-distribution detection	60
A.4.3. Generating low-entropy samples using SGLD	63
List of Figures	65
List of Tables	67
Bibliography	68

1. Introduction

In recent years, the number of applications leveraging machine learning has risen significantly. In particular, deep learning has become the standard for many applications, outperforming traditional machine learning by large margins in the sub-fields of computer vision [OMa+20] and natural language processing [Tor+21]. Nowadays, security-critical applications such as autonomous driving and medical diagnosis [Gri+20; SWS17] leverage neural networks. However, their behavior and robustness is not fully understood yet [Zha+21], posing a significant risk. One particular finding is that deep learning models often assign confident predictions to data on which they were not initially trained [HAB19; LPB17], i.e., they make wrong predictions with high confidence. The overconfidence hinders the adoption of these models in real-world applications since one cannot be sure whether to trust the predictions.

Recent research aims to solve this problem: on the one hand, by accounting for uncertainty in the prediction of a neural network [Gal16] and, on the other hand, by estimating the underlying density of the training data to decide whether a given input is likely under the training data distribution and therefore the model will perform according to its specification [Ruf+21].

For the latter task, recent work proposes increasingly powerful density estimators, e.g., Normalizing Flows [RM15]. Normalizing Flows transform a base distribution with a series of invertible transformations allowing the computation of exact likelihoods. However, Nalisnick et al. [Nal+19a] and Kirichenko et al. [KIW20] recently showed that Normalizing Flows trained to estimate the density of the training data, assign higher likelihood to other data, termed out-of-distribution (OOD), than the in-distribution (ID) data. This renders Normalizing Flows unsuitable for the task of detecting inputs that the models cannot confidently predict. One particular issue could be that Normalizing Flows rely on transformations for which the determinant of the Jacobian is easy to compute to be tractable, restricting the expressiveness of individual transformations [Ver+21].

Another promising class of density estimators are EBMs [Lec+06]. EBMs are not restricted to invertible transformations since EBMs use a single, flexible function mapping from the data domain to the scalar energy value. This allows the usage of existing, powerful neural network architectures without modification. To this end, W. Grathwohl et al. [Gra+20] demonstrate good performance at detecting OOD samples using EBMs based on the finding that discriminative models can be interpreted as EBMs.

Overall, these findings encourage that EBMs might be better suited for the task of OOD detection. Therefore, we aim to leverage EBMs in order to improve OOD detection in this work. Further, we aim to study the main factors facilitating superior OOD detection of EBMs

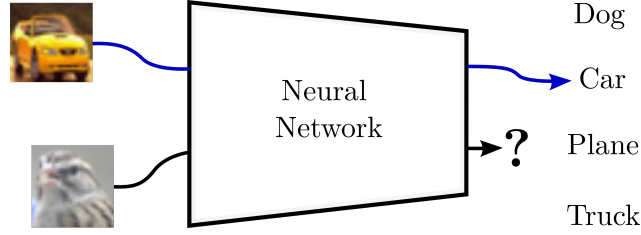


Figure 1.1.: Inference in a classification model for an ID input (*car*) and OOD input (*bird*).

versus other generative models such as Normalizing Flows.

1.1. Problem statement

Our focus in this thesis is on the classification setting. In more detail, we consider a neural network taking an input, e.g., an image, and classifying the input into a predefined set of classes. We illustratively visualize this setting in Figure 1.1. Here, the network is successfully able to predict the class of the image containing the car.

However, the second image is not similar to the training data of the model. Intuitively, one would expect that in the case of an input that is not similar to any data the model has seen, the model would be maximally uncertain, i.e., it assigns every existing class the same probability. However, theoretical [HAB19] (for neural networks with ReLU activations) and empirical [LPB17; GG16] results show that the model assigns *one of the existing classes* high probability. Thus, the model makes confident, wrong predictions which could lead to disastrous outcomes when deploying this model in security-critical applications. The goal of OOD detection is to detect such inputs.

1.2. Related Work

As the main focus is reliable OOD detection, relevant prior work mainly revolves around the tasks of OOD detection and uncertainty estimation in the classification setting.

Uncertainty Estimation. Malinin et al. [MG18; MG19] obtain uncertainty estimates for OOD detection by predicting parameters of a Dirichlet distribution for classification. Charpentier et al. [CZG20] extended this approach to not rely on a separate OOD dataset by learning density-based pseudo counts. Other methods obtain uncertainty estimates based on a Bayesian framework by learning a distribution over model parameters given the data [Blu+15; Mad+19; RBB18], approximating that distribution with samples [LPB17] or with a variational approximation [GG16]. Another line of approaches estimates uncertainty with a single deterministic neural network. Van Amersfoort et al. [Van+20] leverage Radial Basis Function (RBF) networks [BL88] to provide uncertainty estimates by ensuring smoothness of the

networks through a gradient penalty. Instead, J. Liu et al. [Liu+20a] use spectral normalization for enforcing smoothness and a Gaussian Process in the output layer enabling probabilistic reasoning. Finally, van Amersfoort et al. [vAme+21] improve this approach by using a point approximation of the Gaussian process [Tit09] enabling accuracy similar to modern discriminative methods.

Classifier-based OOD detection. Hendrycks et al. [HG17] initially proposed to use the maximum softmax probability as OOD score. Liang et al. [LLS18] and Hsu et al. [Hsu+20] augment this approach by temperature scaling. Several methods add additional loss terms to the objective based on a separate OOD dataset [HMD19], a generative model [Lee+18a; SS18] or a uninformative noise distribution [HAB19] to encourage maximum entropy predictions for OOD inputs.

Density-based OOD detection. Other methods estimate the distribution over feature activations of a pre-trained network at multiple layers with class conditional Gaussian distributions [Lee+18b] or with Normalizing Flows [ZT20]. Another set of methods aims to learn the density over the input data directly. Nalisnick et al. [Nal+19a] discovered that the density learned by generative models cannot distinguish between in-distribution and OOD inputs but focus their analysis on flow-based models. Instead, Ren et al. [Ren+19] find that the likelihood in generative models is heavily affected by background statistics and instead propose a likelihood ratio-based score. Similarly, [Ser+20] find a significant influence of input complexity and propose a likelihood ratio based on a complexity estimate. Nalisnick et al. [Nal+19b] discover a mismatch between the typical set and high-density regions which is tackled in Choi et al. [CJA19] by estimating the epistemic uncertainty through an ensemble of generative models, in Morningstar et al. [Mor+21] through multiple summary statistics of the generative model, and in Nalisnick et al. [Nal+19b] through a statistical test of typicality. However, these methods focus on flow-based and autoregressive density methods with tractable likelihood.

Energy-based models for OOD detection. Recently, there has been increasing interest in leveraging EBMs as generative models for OOD detection. Du et al. [DM19] investigate the generative capabilities and generalization of EBMs to OOD inputs based on approximate maximum-likelihood training. Zhai et al. [Zha+16] introduces EBM architectures for different types of data and a score matching objective for training EBMs for anomaly detection. W. Grathwohl et al. [Gra+20] and W. S. Grathwohl et al. [Gra+21] derive optimization procedures for hybrid EBMs and investigate their OOD detection performance.

Differentiation to prior work. In contrast to prior work, the research conducted in this thesis aims to connect the two aforementioned, seemingly unrelated research directions of EBMs and Dirichlet-based models. While existing work on EBMs reports great OOD detection

results, it does not study the factors leading to improved OOD detection with EBMs compared to other generative models.

Most relevant to the latter is the work by Kirichenko et al. [KIW20] and Schirrmeister et al. [Sch+20] which found that Normalizing Flows learn low-level features common to image datasets and thus struggle with detecting OOD inputs. We aim to provide similar insight for EBMs.

2. Background

In this section, we introduce key terminology and concepts which are required for comprehension of the work conducted in this thesis. Further, we expand on specific prior work and fundamental knowledge relevant for the proposed method introduced in Chapter 3 and comparisons in Chapter 4.

2.1. Classification

In the classification setting, we consider a function $f_\theta : \mathbb{R}^D \mapsto \mathbb{R}^C$, which in our case is a neural network with parameters θ , assigning real values, so called logits, for a fixed amount of classes $C \in \mathbb{N}, C \geq 2$ given a datapoint $\mathbf{x} \in \mathbb{R}^D$. The probabilities over the individual classes $y \in \{1, \dots, C\}$ are defined using the softmax transfer function [GBC16] as

$$p_\theta(y \mid \mathbf{x}) = \frac{\exp(f_\theta(\mathbf{x})[y])}{\sum_{y'} \exp(f_\theta(\mathbf{x})[y'])} \quad (2.1)$$

where we use $f_\theta(\mathbf{x})[y]$ to denote the y -th logit.

Traditionally, one uses a labeled dataset $\mathcal{D} = \{(\mathbf{x}^{(i)}, y^{(i)})\}_{i=1}^N$ to optimize the parameters θ of the neural network f using the cross-entropy objective [GBC16]

$$\min_{\theta} \mathbb{E}_{(\mathbf{x}^{(i)}, y^{(i)}) \sim \mathcal{D}} \left[- \sum_{c=1}^C \delta_{y^{(i)}, c} p_\theta(c \mid \mathbf{x}) \right] \quad (2.2)$$

where δ denotes the Kronecker delta.

2.2. Uncertainty Estimation

In security-critical applications, one often considers the notion of uncertainty. In the context of machine learning, uncertainty refers to the confidence of the model being correct. In particular, we expect that the model reports increasing uncertainty as the model performance degrades such that uncertainty is meaningful in practice.

For classification models describing a conditional density $p_\theta(y \mid \mathbf{x})$ over the classes y given the data \mathbf{x} , uncertainty is divided into *aleatoric* and *epistemic* uncertainty.

Aleatoric uncertainty or *data uncertainty* refers to the uncertainty inherent to the data-generating process. Aleatoric uncertainty is *irreducible*, i.e., collecting additional training data or increasing the capacity of the model does not reduce aleatoric uncertainty. Using the example of flipping a coin, we cannot predict the outcome of a coin toss with higher accuracy than 50% - assuming a perfect coin - due to the inherent aleatoric uncertainty in the outcome.

On the other hand, *epistemic uncertainty* or *model uncertainty* describes the uncertainty in the model parameters given the training dataset. Therefore, one can reduce epistemic uncertainty by collecting more data or increasing the model capacity.

Bayesian view on uncertainty. Current approaches use a Bayesian view on uncertainty estimation [MG18; GG16]. For this, consider a finite dataset $\mathcal{D} = \{\mathbf{x}_i, y_i\}_{i=1}^N$ and a classification model $p(y|\mathbf{x}, \mathcal{D})$.

One defines the aleatoric uncertainty as the uncertainty in the posterior distribution over classes given the parameters of the model θ , while uncertainty in the posterior distribution over the model parameters θ given the finite dataset \mathcal{D} represents the epistemic uncertainty:

$$p(y | \mathbf{x}, \mathcal{D}) = \int \underbrace{p(y|\mathbf{x}, \theta)}_{\text{Data}} \underbrace{p(\theta | \mathcal{D})}_{\text{Model}} d\theta \quad (2.3)$$

Since the true posterior distribution over parameters $p(\theta | \mathcal{D})$ is intractable, various approximations $q(\theta)$ have been proposed. Bayesian Neural Networks (BNNs) [Blu+15; Mad+19; RBB18] allow estimating a full distribution over weights, however, BNNs are typically restricted to simple architectures. Two popular approaches which scale to complex tasks and show good performance in practice are Monte Carlo Dropout [GG16] and Deep Ensembles [LPB17].

2.2.1. Monte Carlo Dropout

Gal et al. [GG16] propose to use Dropout [Sri+14] in order to obtain a variational approximation of the true weight posterior $p(\theta | \mathcal{D})$. In more detail, they define their approximation $q(\theta)$ as

$$W_i = M_i \cdot \text{diag}(\mathbf{z}_i) \quad (2.4)$$

$$\mathbf{z}_i \sim \text{Bernoulli}(p_i) \quad \text{for } i = 1, \dots, L \quad (2.5)$$

with $\theta = \{\mathbf{W}_i\}_{i=1}^L$, the Dropout probability p_i and weight matrices M_i as variational parameters.

Gal et al. [GG16] obtain the predictive distribution by plugging $q(\boldsymbol{\theta})$ into Equation (2.3), yielding

$$q(y | \mathbf{x}) = \int p(y | \mathbf{x}, \boldsymbol{\theta}) q(\boldsymbol{\theta}) d\boldsymbol{\theta}. \quad (2.6)$$

The epistemic uncertainty is estimated as the empirical variance of $q(y | \mathbf{x})$ given by T stochastic forward passes with realizations of the Dropout configurations $\{\mathbf{z}_1^t, \dots, \mathbf{z}_L^t\}_{t=1}^T$.

2.2.2. Deep Ensemble

With a similar goal, Lakshminarayanan et al. [LPB17] train an ensemble of neural networks to estimate uncertainty. From a probabilistic view, the ensemble approximates $p(\boldsymbol{\theta} | \mathcal{D})$ through samples. Similar to Monte Carlo Dropout, Lakshminarayanan et al. [LPB17] define the expected predictive distribution as

$$p(y | \mathbf{x}, \mathcal{D}) \approx M^{-1} p(y | \mathbf{x}, \boldsymbol{\theta}_m) \quad (2.7)$$

where $\{\boldsymbol{\theta}_i\}_{i=1}^M$ are the parameters of the M individual models of the ensemble. Deep Ensembles leverage the Maximum Softmax Probability (MSP) of the expected predictive distribution $\max p(y | \mathbf{x})$ to measure uncertainty.

2.2.3. Dirichlet-based Models

Malinin et al. [MG18] propose to decompose the *epistemic uncertainty* by introducing *distributional uncertainty*, which emerges due to mismatch between train and test data distributions. This decomposition allows to further differentiate between the sources of uncertainty: The *aleatoric* uncertainty captures the uncertainty in situations of class overlap or noise, e.g., semantically similar classes such as cars and trucks, which means that the model knows both classes and is uncertain about the actual class (*known-unknown*). On the other hand, *distributional uncertainty* reflects an *unknown-unknown*, e.g., the input does not belong to any of the classes of the training dataset, i.e., OOD inputs.

Malinin et al. [MG18] capture distributional uncertainty through a prior over categorical distributions. Incorporating the additional prior leads to the following predictive distribution:

$$p(y | \mathbf{x}, \mathcal{D}) = \int \int p(y | \boldsymbol{\mu}) p(\boldsymbol{\mu} | \mathbf{x}, \boldsymbol{\theta}) p(\boldsymbol{\theta} | \mathcal{D}) d\boldsymbol{\mu} d\boldsymbol{\theta} \quad (2.8)$$

Dirichlet Prior Networks. A instance of models incorporating distributional uncertainty estimates at the task of classification are DPNs [MG18; MG19]. They propose to parameterize the prior distribution $p(\boldsymbol{\mu} | \mathbf{x}, \mathcal{D})$ with a Dirichlet distribution which is the conjugate

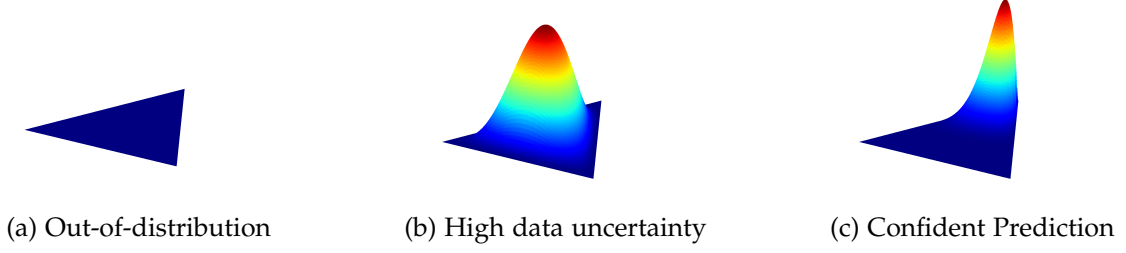


Figure 2.1.: Posterior Dirichlet distributions $p(\boldsymbol{\mu} \mid \mathbf{x}, \mathcal{D})$ with desired behavior.

prior [Bis06] to the categorical distribution and thus has nice analytic properties. A Dirichlet distribution is parameterized by a vector of concentration parameters $\boldsymbol{\alpha} = [\alpha_1, \dots, \alpha_C]^T$.

$$\text{Dir}(\boldsymbol{\mu} \mid \boldsymbol{\alpha}) = \frac{\Gamma(\alpha_0)}{\prod_{c=1}^C \Gamma(\alpha_c)} \prod_{c=1}^C \mu_c^{\alpha_c - 1}, \quad \alpha_c > 0 \quad (2.9)$$

where $\alpha_0 = \sum_{c=1}^C \alpha_c$ is the *precision* of the distribution and Γ denotes the Gamma function. Higher precision leads to sharper distributions as shown in Figure 2.1.

In DPN, one aims to obtain a flat Dirichlet distribution (Figure 2.1a) where all categorical distributions are equiprobable (unknown-unknown) for OOD data, while for known-unknown inputs (aleatoric uncertainty) uniform categorical distributions should be more likely (Figure 2.1b). Finally, in the case of a confident prediction with little uncertainty, the categorical distributions in the corner of the respective class should be likely under the Dirichlet prior as visualized in Figure 2.1c.

A DPN predicts the concentration parameters $\boldsymbol{\alpha}$, parameterizing the Dirichlet prior as

$$p(\boldsymbol{\mu} \mid \mathbf{x}, \boldsymbol{\theta}) = \text{Dir}(\boldsymbol{\mu} \mid \boldsymbol{\alpha} = \exp(f_{\boldsymbol{\theta}}(\mathbf{x}))) \quad (2.10)$$

where \mathbf{f} is a neural network. Malinin et al. [MG18] use the exponential as activation function to ensure $\alpha_c > 0$.

As a result, the posterior over classes is given by

$$p(y_c \mid \mathbf{x}, \boldsymbol{\theta}) = \int p(y \mid \boldsymbol{\mu}) p(\boldsymbol{\mu} \mid \mathbf{x}, \boldsymbol{\theta}) d\boldsymbol{\mu} \quad (2.11)$$

$$= \frac{\alpha_c}{\alpha_0} \quad (2.12)$$

$$= \frac{\exp(f(\mathbf{x}; \boldsymbol{\theta})[c])}{\sum_{c'=1}^C \exp(f(\mathbf{x}; \boldsymbol{\theta})[c'])} \quad (2.13)$$

which is equivalent to the output of a neural network with Softmax activation. Thus, standard cross-entropy training, as described in Section 2.1, can be seen as optimizing the expected categorical distribution under a Dirichlet prior [MG18]. Unfortunately, the mean $\frac{\alpha_c}{\alpha_0}$ is insensitive to arbitrary scaling of the concentration parameters, which means the precision α_0 and therefore uncertainty estimates are meaningless under cross-entropy training.

In order to achieve the expected behavior, Malinin et al. [MG18] propose to train the DPN by minimizing the Kullback-Leibler divergence (KL divergence) [KL51] between the predicted distribution and a sharp Dirichlet distribution with concentration parameters $\hat{\alpha}$ for the in-distribution dataset p_{in} and a flat Dirichlet with parameters $\tilde{\alpha}$ for out-of-distribution data p_{out} where all categorical distributions are equiprobable.

$$L(\theta) = \mathbb{E}_{p_{in}(\mathbf{x})} [D_{KL} [\text{Dir}(\mu | \hat{\alpha}) || p(\mu | \mathbf{x}, \theta)]] \quad (2.14)$$

$$+ \mathbb{E}_{p_{out}(\mathbf{x})} [D_{KL} [\text{Dir}(\mu | \tilde{\alpha}) || p(\mu | \mathbf{x}, \theta)]] \quad (2.15)$$

Training with Equation (3.9) objective requires an OOD dataset p_{out} which ideally covers the entire domain outside of the in-distribution dataset. Since this is unfeasible, Malinin et al. [MG18] propose to use a different, real dataset as OOD samples. Further, they fix the parameters of the target Dirichlet distributions $\tilde{\alpha} = [1, \dots, 1]$ and

$$\hat{\alpha}_c = \begin{cases} 1, & \text{if } c \neq y, \\ \alpha + 1, & \text{otherwise} \end{cases} \quad (2.16)$$

where y is the index of the target class and α is a manually tuned hyperparameter [MG19].

Based on Equation (2.8), Malinin et al. [MG18] compute the *Differential Entropy* of the Dirichlet distribution¹ in order to measure *distributional* uncertainty.

$$\mathcal{H}[p(\mu | \mathbf{x}, \mathcal{D})] = - \int_{\mathcal{S}^{C-1}} p(\mu | \mathbf{x}, \mathcal{D}) \ln(p(\mu | \mathbf{x}, \mathcal{D})) d\mu \quad (2.17)$$

Intuitively, differential entropy measures the flatness of the distribution and therefore indicates OOD samples in the DPN framework.

Posterior Network. Charpentier et al. [CZG20] use a Bayesian update of a categorical distribution based on a prior Dirichlet distribution $\text{Dir}(\beta^{\text{prior}})$ and learned pseudo counts β to form the concentration parameters α of the Dirichlet distribution as

$$\alpha = \beta^{\text{prior}} + \beta \quad (2.18)$$

¹Note that differential entropy is not the correct continuous analog to discrete entropy as it loses certain properties of discrete entropy [Jay57]. We will use it since it has shown to yield consistent results [MG18].

Posterior Network defines the pseudo counts $\beta = [\beta_1, \dots, \beta_C]$ as

$$\beta_c = N_c \cdot p(\mathbf{z}|c, \boldsymbol{\phi}) \quad (2.19)$$

where N_c are the number of observations of class c and $p(\mathbf{z}|c, \boldsymbol{\phi})$ is the density of a Normalizing Flow with parameters $\boldsymbol{\phi}$ at the position of the low-dimensional encoding \mathbf{z} which is the output of an encoder neural network $f(\mathbf{x}, \boldsymbol{\theta})$.

2.2.4. Uncertainty measures.

Based on Equation (2.3), one can derive multiple quantities measuring the *total*, *aleatoric*, or *epistemic* uncertainty.

To measure the overall uncertainty in the prediction, Hendrycks et al. [HG17] use the MSP

$$\max_y p(y | \mathbf{x}, \mathcal{D}) \quad (2.20)$$

and Gal et al. [GG16] use the entropy of the predictive distribution

$$\mathcal{H}(p(y | \mathbf{x}, \mathcal{D})) = - \sum_{c=1}^C p(c | \mathbf{x}, \mathcal{D}) \ln(p(c | \mathbf{x}, \mathcal{D})). \quad (2.21)$$

For measuring *model uncertainty*, Depeweg et al. [Dep+18] consider the *Mutual Information* (MI) [Sha48] between the categorical label t and the parameters of the model $\boldsymbol{\theta}$ measuring the spread of an ensemble $\{p(y | \mathbf{x}, \boldsymbol{\theta}_i)\}_{i=1}^M$ [Gal16]. One can write the model uncertainty as the difference in total uncertainty and data uncertainty measured as the expected entropy of the members of the ensemble following [Dep+18] as

$$\underbrace{\mathcal{I}[y, \boldsymbol{\theta} | \mathbf{x}, \mathcal{D}]}_{\text{Model Uncertainty}} = \underbrace{\mathcal{H}[\mathbb{E}_{p(\boldsymbol{\theta}|\mathcal{D})}[p(y | \mathbf{x}, \boldsymbol{\theta})]]}_{\text{Total Uncertainty}} - \underbrace{\mathbb{E}_{p(\boldsymbol{\theta}|\mathcal{D})}[\mathcal{H}[p(y | \mathbf{x}, \boldsymbol{\theta})]]}_{\text{Data Uncertainty}} \quad (2.22)$$

Further, one can consider another decomposition [MG18] based on marginalizing $\boldsymbol{\theta}$ in Equation (2.3) suitable for DPN models

$$\underbrace{\mathcal{I}[y, \boldsymbol{\mu} | \mathbf{x}, \mathcal{D}]}_{\text{Distributional Uncertainty}} = \underbrace{\mathcal{H}[\mathbb{E}_{p(\boldsymbol{\mu}|\mathbf{x}, \mathcal{D})}[p(y | \boldsymbol{\mu})]]}_{\text{Total Uncertainty}} - \underbrace{\mathbb{E}_{p(\boldsymbol{\mu}|\mathbf{x}, \mathcal{D})}[\mathcal{H}[p(y | \boldsymbol{\mu})]]}_{\text{Data Uncertainty}} \quad (2.23)$$

Here, the distributional uncertainty, as a part of epistemic uncertainty, is explicitly considered as the spread of categorical distributions under the Dirchlet prior similar to differential entropy in Equation (2.17). For simplicity of notation, we will omit the dependence on the dataset \mathcal{D} in the following.

2.3. Density Estimation

Another approach to out-of-distribution detection is to estimate the underlying density of the training data $p(\mathbf{x})$. Then, one considers inputs with sufficiently low density to be out-of-distribution [Pim+14].

Density estimation is the task of approximating the underlying distribution of a dataset while only observing samples from that particular distribution [Sil17]. More formally, consider a finite set of data points $\{\mathbf{x}^{(i)}\}_{i=1}^N, \mathbf{x}^{(i)} \in \mathbb{R}^D$ where the individual data points are sampled independently and identically from an underlying, unknown random variable $\mathbf{x}_i \sim X$ with probability density function $p(\mathbf{x} = \mathbf{x})$. Then, the task is to recover a probability density function $p_\theta(\mathbf{x})$ from the finite dataset $\{\mathbf{x}^{(i)}\}_{i=1}^N$ which is close to the true $p(\mathbf{x})$.

Afterwards, we can evaluate the density $p_\theta(\hat{\mathbf{x}})$ for a particular, novel datapoint $\hat{\mathbf{x}}$ together with a threshold to determine if that datapoint comes from the underlying distribution $p(\mathbf{x})$.

Figure 2.2 shows an illustrative example of a density estimate of a dataset of images containing cars and trucks. Consequently, regions of high density surround the samples of cars and trucks. On the other hand, samples not belonging to the dataset, e.g., the image of a deer, are assigned low density. Thus, one can differentiate between in-distribution data, i.e., cars and trucks, and out-of-distribution data by comparing the density evaluated at the position of the data points.

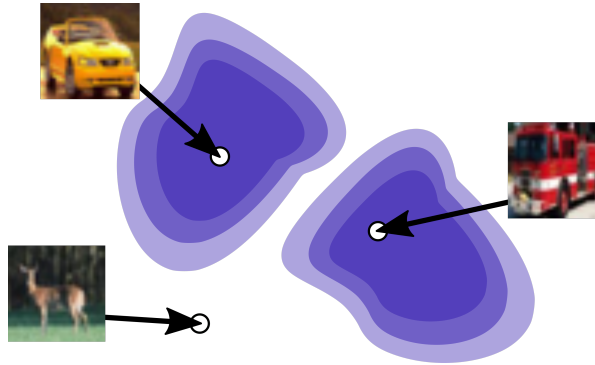


Figure 2.2.: Example density estimate of dataset of images of cars and trucks. Darker shades of blue indicates higher density.

2.3.1. Normalizing Flows

A particular class of density estimators are Normalizing Flows introduced in Rezende et al. [RM15]. Normalizing Flows transform a base distribution $p(\mathbf{z})$ into another distribution $p(\mathbf{x})$ based on the change of variable formula

$$p_2(\mathbf{x}) = p_1(f^{-1}(\mathbf{x})) \cdot \left| \det \left(\frac{\partial f^{-1}(\mathbf{x})}{\partial \mathbf{x}} \right) \right| \quad (2.24)$$

where $f : \mathbb{R}^D \mapsto \mathbb{R}^D, f(\mathbf{z}) = \mathbf{x}$ is an invertible and differentiable transformation.

These transformations can be stacked obtaining a series of differentiable and invertible transformations f_1, \dots, f_n transforming a base density $p_0(\mathbf{z}_0)$ into a potentially complex target density $p_n(\mathbf{x})$

$$\log p_n(\mathbf{x}) = p_0(\mathbf{z}_0) + \sum_{i=1}^n \log \left| \det \left(\frac{\partial f_i}{\partial \mathbf{z}_i} \right) \right| \quad (2.25)$$

where $\mathbf{z}_i = f_i(\mathbf{z}_{i-1})$.

In order to speed up the computation of the determinant, various transformations with triangular Jacobian structure have been proposed [RM15] at the cost of reducing the expressiveness of individual transformations.

Affine Coupling Layers. A popular instance of the transformations are Affine Coupling layers [DSB17; KD18; DKB15] which allow efficient determinant computation while being expressive. For this, the input \mathbf{x} is split into two disjoint subsets $\mathbf{x}_a, \mathbf{x}_b$ and the output $\mathbf{y} = [\mathbf{y}_a, \mathbf{y}_b]$ is defined as

$$(\mathbf{s}, \mathbf{t}) = \text{NN}(\mathbf{x}_b) \quad (2.26)$$

$$\mathbf{y}_a = \mathbf{s} \odot \mathbf{x}_a + \mathbf{t} \quad (2.27)$$

$$\mathbf{y}_b = \mathbf{x}_b \quad (2.28)$$

where NN can be an arbitrary neural network. As a result of this choice of transformation the Jacobian

$$\frac{\partial f}{\partial \mathbf{x}} = \begin{pmatrix} \mathbb{I}_d & 0 \\ \frac{\partial \mathbf{y}_a}{\partial \mathbf{x}_a} & \text{diag}(\exp(\mathbf{s})) \end{pmatrix} \quad (2.29)$$

has triangular structure. Thus, the determinant can be computed efficiently as

$$\det \left(\frac{\partial f}{\partial \mathbf{x}} \right) = \prod_{i=1}^D \left(\frac{\partial f}{\partial \mathbf{x}} \right)_{ii}. \quad (2.30)$$

Training. In order to optimize the parameters θ of the transformations f_1, \dots, f_n , one uses maximum likelihood estimation [RM15]. That is, one optimizes

$$\max_{\theta} \sum_{i=1}^N \log p_{\theta}(\mathbf{x}^{(i)}) \quad (2.31)$$

given a set of data points $\{\mathbf{x}^{(i)}\}_{i=1}^N$

We compare against Normalizing Flows based on affine coupling layers in the experimental section.

2.3.2. Energy-based Models

EBMs [Lec+06] use the energy-function E_θ which defines a density over the data \mathbf{x} as

$$p_\theta(\mathbf{x}) = \frac{\exp(-E_\theta(\mathbf{x}))}{Z(\theta)} \quad (2.32)$$

where θ are learnable parameters and $Z(\theta) = \int \exp(-E_\theta(\mathbf{x}))d\mathbf{x}$ is the normalizing constant of the EBM. Z_θ ensures that the induced density function Equation (2.32) integrates to 1. However, Z_θ is often hard to compute or even approximate since it is a high-dimensional integral. On the positive side, E_θ can be any function $E_\theta : \mathbb{R}^D \mapsto \mathbb{R}$ placing no restrictions on the transformations compared to Normalizing Flows.

Note that we can directly use the energy for OOD detection. That is, since a data point having high probability is equivalent to having low energy as $p_\theta(\mathbf{x}) \propto -E_\theta(\mathbf{x})$. This means we are not required to estimate the normalizing constant $Z(\theta)$ in practice by considering a decision threshold τ and binary classifier G for OOD data as

$$G(\mathbf{x}, \tau, \theta) = \begin{cases} 0, & \text{if } -E_\theta(\mathbf{x}) \leq \tau, \\ 1, & \text{if } -E_\theta(\mathbf{x}) > \tau \end{cases} \quad (2.33)$$

where 1 corresponds to ID and 0 to OOD data.

Joint Energy-based model. We additionally consider Joint Energy-based models (JEMs) for discriminative EBMs [Gra+20]. Suppose $f_\theta : \mathbb{R}^D \mapsto \mathbb{R}^C$ is a classifier assigning logits for C classes for a data point $\mathbf{x} \in \mathbb{R}^D$ as in Section 2.1. W. Grathwohl et al. [Gra+20] interpret the logits as unnormalized probabilities of the joint distribution

$$p_\theta(\mathbf{x}, y) = \frac{\exp(f_\theta(\mathbf{x})[y])}{Z(\theta)} \quad (2.34)$$

yielding the marginal distribution over \mathbf{x} as

$$p_\theta(\mathbf{x}) = \sum_y p_\theta(\mathbf{x}, y) \quad (2.35)$$

For training, W. Grathwohl et al. [Gra+20] use the factorization

$$\log p_{\theta}(\mathbf{x}, y) = \log p_{\theta}(\mathbf{x}) + \log p_{\theta}(y | \mathbf{x}) \quad (2.36)$$

using Equation (2.1) and Equation (2.35). In particular, W. Grathwohl et al. [Gra+20] use a standard Cross Entropy objective to optimize $p_{\theta}(y | \mathbf{x})$ weighted with hyperparameter γ .

Training EBMs

Since the normalizing constant $Z(\theta)$ is intractable, plain maximum likelihood training is not feasible. As a result, research proposes different methods to optimize EBMs. For optimizing $p_{\theta}(\mathbf{x})$, we consider several approaches that scale to high-dimensional data. In the following, we briefly discuss these approaches.

Sliced Score Matching. Hyvärinen [Hyv05] propose to learn an unnormalized density by approximating the gradient of the distribution $\psi(\mathbf{x}) = \nabla_{\mathbf{x}} p(\mathbf{x})$, i.e., the score of the distribution, instead of the distribution itself by minimizing

$$L(\theta) = \frac{1}{2} \mathbb{E}_{p(\mathbf{x})} [\|\nabla_{\mathbf{x}} \log p_{\theta}(\mathbf{x}) - \nabla_{\mathbf{x}} p(\mathbf{x})\|^2] \quad (2.37)$$

Note that this objective does not depend on the normalizing constant $Z(\theta)$ as

$$\nabla_{\mathbf{x}} \log p_{\theta}(\mathbf{x}) = \nabla_{\mathbf{x}} E_{\theta}(\mathbf{x}) - \underbrace{\nabla_{\mathbf{x}} Z(\theta)}_{=0} \quad (2.38)$$

However, Equation (2.37) relies on the unknown groundtruth density $p(\mathbf{x})$ we are trying to recover. Instead, Hyvärinen [Hyv05] propose an optimization scheme requiring only samples from the groundtruth distribution, leveraging integration by parts, yielding

$$L(\theta) = \mathbb{E}_{p(\mathbf{x})} \left[\sum_{i=1}^D \left(\partial_i \psi_i(\mathbf{x}, \theta) + \frac{1}{2} \psi_i(\mathbf{x}, \theta)^2 \right) \right] + \text{constant} \quad (2.39)$$

$$= \mathbb{E}_{p(\mathbf{x})} \left[\frac{1}{2} \sum_{i=1}^D \left(\frac{\partial^2 E_{\theta}}{(\partial x_i)^2} + \frac{1}{2} \left(\frac{\partial E_{\theta}}{\partial x_i} \right)^2 \right) \right] + \text{constant} \quad (2.40)$$

The optimization of Equation (2.40) involves computing matrix Hessian-products which are expensive for high dimensional data.

In order to circumvent this problem, Song et al. [Son+20] propose Sliced Score Matching (SSM), an alternative update formula based on a random projection. The update only involves vector-Hessian products which one can compute in constant time w.r.t. the dimensionality of the data. This change allows the training of models on high-dimensional data such as images.

$$\mathbb{E}_{p_{\mathbf{v}}} \mathbb{E}_{p(\mathbf{x})} \left[\mathbf{v}^T \nabla_{\mathbf{x}} \boldsymbol{\psi}_{\boldsymbol{\theta}}(\mathbf{x}) \mathbf{v} + \frac{1}{2} \|\boldsymbol{\psi}_{\boldsymbol{\theta}}(\mathbf{x})\|_2^2 \right] \quad (2.41)$$

where $\mathbf{v} \sim p_{\mathbf{v}}$ is a simple distribution of random vectors, e.g. Gaussian.

Contrastive Divergence. As mentioned before, direct maximum likelihood estimation is not possible with EBMs due to the intractable normalizing constant $Z(\boldsymbol{\theta})$. However, it is possible to estimate the gradient of the maximum likelihood objective.

$$\nabla_{\boldsymbol{\theta}} \log p_{\boldsymbol{\theta}}(\mathbf{x}) = -\nabla_{\boldsymbol{\theta}} E_{\boldsymbol{\theta}}(\mathbf{x}) - \nabla_{\boldsymbol{\theta}} \log Z(\boldsymbol{\theta}) \quad (2.42)$$

$\nabla_{\boldsymbol{\theta}} \log Z(\boldsymbol{\theta})$ is intractable to compute directly, though, one can rewrite the expressions as the following expectation [SK21]:

$$\nabla_{\boldsymbol{\theta}} \log Z(\boldsymbol{\theta}) = \mathbb{E}_{\mathbf{x} \sim p_{\boldsymbol{\theta}}(\mathbf{x})} [\nabla_{\boldsymbol{\theta}} E_{\boldsymbol{\theta}}(\mathbf{x})] \quad (2.43)$$

Following recent literature [DM19], we approximate the expectation in Equation (2.43) using samples obtained through Stochastic Gradient Langevin Dynamics (SGLD) [WT11].

Welling et al. [WT11] use an Langevin diffusion process with step size α and K steps in order to sample from $p_{\boldsymbol{\theta}}(\mathbf{x})$:

$$\mathbf{x}^{(k+1)} = \mathbf{x}^{(k)} + \frac{\alpha^2}{2} \nabla_{\mathbf{x}} \log p_{\boldsymbol{\theta}}(\mathbf{x}^{(k)}) + \alpha \mathbf{z}^{(k)}, \quad \mathbf{z}^{(k)} \sim N(\mathbf{0}, \mathbf{I}), \quad k = 0, \dots, K-1 \quad (2.44)$$

Under some regularity conditions, $\mathbf{x}^{(K)}$ is guaranteed to be a sample from $p_{\boldsymbol{\theta}}(\mathbf{x})$ as $\alpha \mapsto 0$ and $K \mapsto \infty$.

Contrastive Divergence [Hin02] approximates the gradient of the maximum likelihood objective using the SGLD Markov Chain Monte Carlo (MCMC) sampler with a finite K by

$$\nabla_{\boldsymbol{\theta}} p_{\boldsymbol{\theta}}(\mathbf{x}) = \mathbb{E}_{\mathbf{x}' \sim p_{\boldsymbol{\theta}}(\mathbf{x})} [\nabla_{\boldsymbol{\theta}} E_{\boldsymbol{\theta}}(\mathbf{x}')] - \nabla_{\boldsymbol{\theta}} E_{\boldsymbol{\theta}}(\mathbf{x}) \quad (2.45)$$

Further, $\mathbf{x}^{(0)}$ is initialized from a replay buffer [Tie08]. Overall, this leads to samples which are only approximately distributed according to $p_{\boldsymbol{\theta}}(\mathbf{x})$. However, [Gra+20; DM19] show this approximation to be sufficient for training EBMs in practice.

Variational Entropy Regularized Approximate Maximum Likelihood. Lastly, we consider the recently proposed Variational Entropy Regularized Approximate Maximum Likelihood (VERA) training [Gra+21]. W. S. Grathwohl et al. [Gra+21] propose to learn the parameters ϕ of an auxiliary distribution q_ϕ as the optimum of

$$\log Z(\theta) = \max_{q_\phi} \mathbb{E}_{q_\phi(\mathbf{x})} [f_\theta(\mathbf{x})] + \mathcal{H}(q_\phi) \quad (2.46)$$

which one can plug into Equation (2.34) to obtain an alternative method for training EBMs. W. S. Grathwohl et al. [Gra+21] choose a generator distribution of the form $q_\phi(\mathbf{x}) = \int_{\mathbf{z}} q_\phi(\mathbf{x} | \mathbf{z}) q_\phi(\mathbf{z}) d\mathbf{z}$. To estimate the entropy term $\mathcal{H}(q_\phi)$, they propose a variational approximation circumventing the need for sampling as in prior work [Die+19; TR19] and thus speed up training.

Finally, note that there exist more approaches [GH10; CG18] for training EBMs. However, they do not scale to high-dimensional data as they make strong assumptions about the data. We conduct initial experiments with these approaches in Appendix A.4.

2.3.3. Energy-based out-of-distribution detection

In contrast to training full EBMs, W. Liu et al. [Liu+20b] found the energy $E_\theta(\mathbf{x})$ of a model, trained with cross-entropy loss only, to be effective for OOD detection. In particular, they find that the energy score outperforms other scores in the literature such as the MSP $\max_y p_\theta(y | \mathbf{x})$ [HG17]. To motivate this, W. Liu et al. [Liu+20b] show that the MSP score loses relevant information in the scale of the logits as

$$\begin{aligned} \max_y p_\theta(y | \mathbf{x}) &= \max_y \frac{\exp(f_\theta(\mathbf{x})[y])}{\sum_{y'} \exp(f_\theta(\mathbf{x})[y'])} \\ &= \frac{1}{\sum_{y'} \exp(f_\theta(\mathbf{x})[y'] - \max_y f_\theta(\mathbf{x})[y])} \end{aligned} \quad (2.47)$$

W. Liu et al. [Liu+20b] proceed to rewrite Equation (2.48) using Equation (2.35) and obtain

$$\log \max_y p_\theta(y | \mathbf{x}) = E_\theta(\mathbf{x}) + \max_y f_\theta(\mathbf{x})[y] \quad (2.48)$$

$$= -\log p_\theta(\mathbf{x}) - \log Z(\theta) + \underbrace{\max_y f_\theta(\mathbf{x})[y]}_{\text{Not constant w.r.t. } \mathbf{x}} \quad (2.49)$$

$$\not\propto -\log p_\theta(\mathbf{x}), \quad (2.50)$$

i.e., the MSP is not aligned with the marginal density of the model. This motivates the usage of the energy score $E_\theta(\mathbf{x})$ for OOD detection instead.

To further improve the OOD detection, they propose a margin loss based on a separate dataset with OOD data \mathcal{D}_{OOD} as

$$\begin{aligned} L_{\text{Energy}} = & \mathbb{E}_{(\mathbf{x}, y) \sim \mathcal{D}} [\max(0, E_{\theta}(\mathbf{x}) - m_{\text{in}})]^2 \\ & + \mathbb{E}_{(\mathbf{x}, y) \sim \mathcal{D}_{\text{OOD}}} [\max(0, m_{\text{out}} - E_{\theta}(\mathbf{x}))]^2 \end{aligned} \quad (2.51)$$

Intuitively, Equation (2.51) regularizes the energy function E_{θ} to output energy of at most m_{in} for ID data and at least m_{out} for OOD data. In other words, the objective encourages high $p_{\theta}(\mathbf{x})$ for ID and low $p_{\theta}(\mathbf{x})$ for OOD datapoints. m_{in} , m_{out} , and the weighting λ of the loss term L_{Energy} are hyperparameters that need to be tuned.

3. Method

In this chapter, we introduce our model which builds upon existing work discussed in Chapter 2. In particular, we establish a connection between EBMs and Dirichlet Prior Network in Section 3.1. Based on our findings, we introduce Energy-Prior Network together with a training objective in Section 3.2. Finally, we discuss the properties of EPN in Section 3.2.2 where we also highlight theoretical advantages our model compared to prior work.

3.1. Derivation of Joint View

In the following, we derive a connection between a Joint Energy-based model (JEM) [Gra+20] and a Dirichlet Prior Network (DPN) [MG18]. For this, we start from a discriminative model $f_\theta : \mathbb{R}^D \mapsto \mathbb{R}^C$ mapping datapoints $\mathbf{x} \in \mathbb{R}^D$ to logits. The categorical distribution over classes is given by the softmax function as

$$p_\theta(y | \mathbf{x}) = \frac{\exp(f_\theta(\mathbf{x})[y])}{\sum_{y'} \exp(f_\theta(\mathbf{x})[y'])} \quad (3.1)$$

Next, let us shortly recall the definition of JEM and DPN from Section 2.3.2 and Section 2.2.3, respectively.

Joint Energy-based model. In JEM, we consider the logits to introduce a joint distribution over data \mathbf{x} and labels y as

$$p_\theta(\mathbf{x}, y) = \frac{\exp(f_\theta(\mathbf{x})[y])}{Z(\theta)}.$$

We can marginalize y using $p_\theta(\mathbf{x}) = \sum_y p_\theta(\mathbf{x}, y)$ and obtain for the unnormalized marginal data distribution

$$\tilde{p}_\theta(\mathbf{x}) = \sum_y \tilde{p}_\theta(\mathbf{x}, y) \quad (3.2)$$

$$= \sum_y \exp(f_\theta(\mathbf{x})[y]) \quad (3.3)$$

where we use \tilde{p} to denote that the distribution is unnormalized.

Dirichlet Prior Network. For DPN, we follow Malinin et al. [MG18] and use the exponential function for predicting the concentration parameters of the Dirichlet distribution to ensure $\alpha_c > 0, c \in \{1, \dots, C\}$

$$\alpha_c = \exp(f_{\theta}(\mathbf{x})[c])$$

We then use the predicted concentration parameters $\boldsymbol{\alpha} = [\alpha_1, \dots, \alpha_C]^T$ to parameterize the Dirichlet prior over categorical distributions $p(\boldsymbol{\mu} \mid \mathbf{x}, \boldsymbol{\theta}) = \text{Dir}(\boldsymbol{\alpha})$.

As a result, the *precision* of the Dirichlet distribution is given by

$$\begin{aligned} \alpha_0 &= \sum_y \alpha_y \\ &= \sum_y \exp(f_{\theta}(\mathbf{x})[y]) \end{aligned}$$

Joint view. Observe that we arrive at the same quantity $\sum_y \exp(f_{\theta}(\mathbf{x})[y])$ in DPN and JEM with different interpretations based on the considered model. In JEM, $\sum_y \exp(f_{\theta}(\mathbf{x})[y])$ corresponds to the unnormalized, marginal data density $\tilde{p}_{\theta}(\mathbf{x})$, while in DPN the same quantity corresponds to the *precision* α_0 of the Dirichlet prior over categorical distributions $p(\boldsymbol{\mu} \mid \mathbf{x}, \boldsymbol{\theta})$:

$$\tilde{p}_{\theta}(\mathbf{x}) = \sum_y \exp(f_{\theta}(\mathbf{x})[y]) = \alpha_0 \tag{3.4}$$

From Section 2.2.3, we remember that the *precision* α_0 influences the sharpness of Dirichlet distribution which measures *distributional uncertainty*. We recall that distributional uncertainty is supposed to increase in the case of OOD inputs. On the other hand, the same quantity interpreted in the scope of JEM describes the unnormalized, marginal density $\tilde{p}_{\theta}(\mathbf{x})$ which is expected to decrease for OOD data.

We conclude that both models leverage the same quantity in order to perform OOD detection. Further note that this joint view is consistent: When the precision α_0 is low in DPN, the distributional uncertainty becomes high indicating OOD input. In that case, the marginal density $\tilde{p}_{\theta}(\mathbf{x})$ of JEM is low as well by Equation (3.4) which indicates OOD samples from the perspective of EBMs. We build upon this identification in the following section to construct a novel model.

3.2. Energy-PriorNet

Based on our insights in Section 3.1, we derive our model, Energy-Prior Network (EPN), and an optimization objective leveraging the connection. Coincidentally, this enables us to

naturally combine both methods to alleviate the disadvantages present in the individual approaches: While EBM’s have shown to be powerful density estimators enabling OOD detection based on the marginal data distribution, their discriminative formulation JEM [Gra+20] lacks a Bayesian decomposition of uncertainty estimates. We find that we can use the Dirichlet-based perspective to equip an JEM with additional uncertainty estimates.

Similarly, Dirichlet Prior Networks [MG18] suffer issues w.r.t. data availability and hyperparameter choice. The energy-based view on Prior Networks allows us to perform training using energy-based optimization resolving two issues in the optimization of DPN in Equation (2.14), i.e.,

- **Requirement of separate out-of-distribution dataset p_{OOD} .** A dataset consisting of inputs considered as OOD might not be readily available. Further, sometimes it might even be hard to define what constitutes OOD inputs. Thus, it becomes hard to cover the entire domain of out-of-distribution inputs.
- **Hyperparameter choice of β_y .** Malinin et al. [MG18] use manual specification of the concentration parameter corresponding to the target class of Dirichlet distribution β_y which is set based on empirical results in the experiments.

In the following, we derive the model based on our prior insights on DPNs and EBM’s from Section 3.1 in order to tackle aforementioned issues.

We again consider a discriminative model $f_\theta : \mathbb{R}^D \mapsto \mathbb{R}^C$. In particular, we do not require any architectural changes since our insights from Section 3.1 simply rely on different interpretations of $\exp(f_\theta(\mathbf{x})[y])$.

In a first step, we incorporate an uninformative prior $\text{Dir}(\boldsymbol{\alpha}^{\text{prior}})$ with $\boldsymbol{\alpha}^{\text{prior}} = [1, \dots, 1]^T$ following Charpentier et al. [CZG20] and Malinin et al. [MG18]. The setting of the prior corresponds to a flat Dirichlet distributions where all categorical distributions are equally likely which is a reasonable assumption in the presence of no observations. To incorporate the prior, remember that we can interpret the exponentiated logits $\{e^{f_\theta(\mathbf{x})[c]}\}_{c=1}^C$ as the concentration parameters $\hat{\boldsymbol{\alpha}} = [e^{f_\theta(\mathbf{x})[1]}, \dots, e^{f_\theta(\mathbf{x})[C]}]^T$ of a Dirichlet distribution $\text{Dir}(\hat{\boldsymbol{\alpha}})$ based on Section 3.1.

We can now use a Bayesian update of the prior distribution which is given in closed form as $\text{Dir}(\boldsymbol{\alpha}^{\text{prior}} + \hat{\boldsymbol{\alpha}})$ [CZG20], i.e, we have for the concentration parameters

$$\alpha_c = \alpha_c^{\text{prior}} + \hat{\alpha}_c \tag{3.5}$$

$$= 1 + \exp(f_\theta(\mathbf{x})[c]) \tag{3.6}$$

to parameterize $p(\boldsymbol{\mu} \mid \mathbf{x}, \theta) = \text{Dir}(\boldsymbol{\alpha})$. In the context of Charpentier et al. [CZG20], we treat the exponentiated logit $\exp(f_\theta(\mathbf{x})[c])$ as learned *pseudo-count* for class c given an input \mathbf{x} .

Next, note that EPN still embeds an Energy-based model similar to JEM. For this, let $f_\theta(\mathbf{x})[c]$ be the classification logit for class c . We can interpret $f_\theta(\mathbf{x})[y]$ as the (negative) joint energy

$E_\theta(\mathbf{x}, y)$ over data and labels yielding the joint distribution of EPN as

$$p_\theta(\mathbf{x}, y) = \frac{\exp(f_\theta(\mathbf{x})[y])}{Z(\theta)} \quad (3.7)$$

The marginal distribution $p_\theta(\mathbf{x})$ is given by marginalizing y . Thus, we obtain

$$p_\theta(\mathbf{x}) = \sum_c p_\theta(\mathbf{x}, c) = \frac{\sum_c \exp(f_\theta(\mathbf{x})[c])}{Z(\theta)} \quad (3.8)$$

where the energy function is now given as $E_\theta(\mathbf{x}) = -\log \sum_c \exp(f_\theta(\mathbf{x})[c])$.

3.2.1. Training

After specifying the model, we introduce a method for training EPN. For this, we take inspiration from Malinin et al. [MG18] for optimizing the predictive performance of our model using the KL divergence between the Dirichlet distribution parameterized using Equation (3.5) and a target Dirichlet distribution we specify in the following. Further, we leverage EBM training as discussed in Section 2.3.2. Overall, we consider the following objective

$$\min - \underbrace{p_\theta(\mathbf{x})}_{\text{Density optimization}} + \underbrace{\text{KL}(\text{Dir}(\boldsymbol{\beta}) \parallel \text{Dir}(\boldsymbol{\alpha}))}_{\text{Classification term}} + \lambda \underbrace{\mathcal{H}(\text{Dir}(\hat{\boldsymbol{\alpha}}))}_{\text{Smoothness Regularizer}} \quad (3.9)$$

where λ is a weighting hyperparameter.

Next, we define the concentration parameters of the target Dirichlet distribution $\boldsymbol{\beta}^{(y)} = [\beta_1, \dots, \beta_C]$ as

$$\beta_c^{(y)} = \begin{cases} 1, & c \neq y \\ \hat{\beta}_0 = \sum_{i=1}^C \hat{\beta}_i = \sum_{i=1}^C 1 + \exp(f_\theta(\mathbf{x})[i]) = C + \tilde{p}_\theta(\mathbf{x}), & c = y \end{cases} \quad (3.10)$$

where y is label of the target class and C is the number of classes.

This objective consists of two main terms which overall contribute to EPN having good predictive performance while retaining reliable uncertainty estimates even far from the training data. In the following, we will analyze both terms and how they are optimized within EPN.

Optimizing the marginal data distribution $p_\theta(\mathbf{x})$. To optimize the marginal data density $p_\theta(\mathbf{x})$, we can leverage EBM training techniques based on our findings in Section 3.1, i.e., that EPN defines a density over θ in Equation (3.8).

That means we can optimize the marginal energy $E_\theta(\mathbf{x})$ with methods introduced in Section 2.3.2. In particular, we consider two versions of our model: *EPN-V* uses VERA for optimizing $p_\theta(\mathbf{x})$, while *EPN-M* uses contrastive divergence instead.

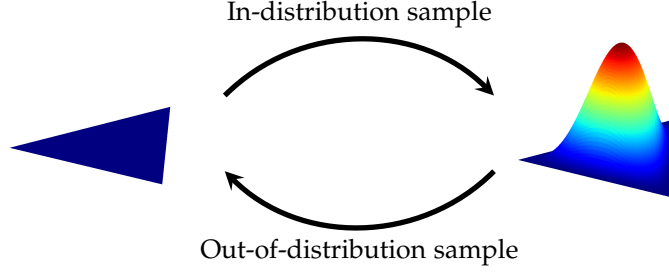


Figure 3.1.: Illustrative example on how the EBM training acts on the posterior $p(\boldsymbol{\mu} \mid \mathbf{x}, \mathcal{D})$ for ID and OOD samples.

In EPN, EBM training allows the interpretation of pushing down on the precision of the Dirichlet distribution $p(\boldsymbol{\mu} \mid \mathbf{x}, \theta)$ for out-of-distribution datapoints while increasing the precision for ID data points as shown in Figure 3.1.

Optimizing classification performance $p_\theta(y \mid \mathbf{x})$. With the second term of Equation (3.9), we aim to optimize the discriminative performance of EPN. Intuitively, our objective forces the model to assign all probability mass of categorical distributions under the Dirichlet prior to be in the corner of the target class y as visualized in Figure 3.2.

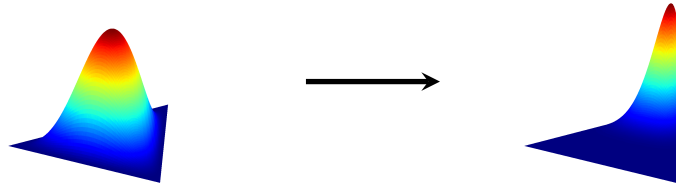


Figure 3.2.: Illustrative example on how the KL divergence term acts on the posterior $p(\boldsymbol{\mu} \mid \mathbf{x}, \mathcal{D})$ for a particular sample with target class in the corner of the Dirichlet distribution.

For further analysis, consider the predicted $q = \text{Dir}(\boldsymbol{\alpha})$ and target $p = \text{Dir}(\boldsymbol{\beta})$ with concentration parameters $\boldsymbol{\alpha} = [\alpha_1, \dots, \alpha_C]^T$ and $\boldsymbol{\beta} = [\beta_1, \dots, \beta_C]^T$ as defined in Equation (3.5) and Equation (3.10), respectively. Further, let $\alpha_0 = \sum_{c=1}^C \alpha_c$ and $\beta_0 = \sum_{c=1}^C \beta_c$ denote the precision of the distributions.

Since the KL-divergence between two Dirichlet distribution is given in closed form, we can expand the term:

$$\begin{aligned}
\text{KL}(\text{Dir}(p \parallel q) &= \\
&\stackrel{(1)}{=} \log \Gamma(\alpha_0) - \sum_{c=1}^C \log \Gamma(\alpha_c) - \underbrace{\log \Gamma(\beta_0)}_{=\log \Gamma(\alpha_0)} + \sum_{c=1}^C \log \Gamma(\beta_k) + \sum_{c=1}^C (\alpha_c - \beta_c)(\psi(\alpha_c) - \psi(\alpha_0)) \\
&\stackrel{(2)}{=} - \sum_{c=1}^C \log \Gamma(\alpha_c) + \sum_{\substack{c=1 \\ c \neq t}}^C \underbrace{\log \Gamma(1)}_{=0} + \log \Gamma(\alpha_0 - K - 1) + \sum_{\substack{c=1 \\ c \neq t}}^C (\alpha_c - 1)(\psi(\alpha_c) - \psi(\alpha_0)) \\
&\quad + (\alpha_t - \alpha_0 - K - 1)(\psi(\alpha_t) - \psi(\alpha_0)) \\
&\stackrel{(3)}{=} - \sum_{c=1}^C \log \Gamma(\alpha_c) + \log \Gamma(\alpha_0 - K - 1) + \sum_{\substack{c=1 \\ c \neq t}}^C (\alpha_c - 1)(\psi(\alpha_c) - \psi(\alpha_0)) \\
&\quad + \sum_{\substack{c=1 \\ c \neq t}}^C \alpha_c(\psi(\alpha_0) - \psi(\alpha_t)) + (K - 1) \underbrace{(\psi(\alpha_0) - \psi(\alpha_t))}_{\text{Uncertainty cross-entropy}}
\end{aligned} \tag{3.11}$$

where ψ denotes the Digamma function. In more detail, (1) uses $\beta_0 = C + \sum_{i=1}^C \exp(f_\theta(\mathbf{x}[i])) = \alpha_0$, (2) uses definition of β_i , and (3) uses $\alpha_t - \alpha_0 = -\sum_{c=1, c \neq t}^C \alpha_c$.

Overall, we arrive at an equation where one term corresponds to the uncertainty cross-entropy loss [BCG19] instantiated for two Dirichlet distributions. In contrast to the cross-entropy loss, this objective incorporates uncertainty by taking the variance of the Dirichlet prior distribution into account. We find that this further motivates the usage of our objective in Equation (3.9).

As an alternative, we also consider the forward KL divergence $\text{KL}(q \parallel p)$. When expanding the terms, we arrive at

$$\begin{aligned}
\text{KL}(q \parallel p) &= -\log \Gamma(\alpha_0 - (K - 1)) \\
&\quad + \sum_{k=1}^K \log \Gamma(\alpha_k) \\
&\quad + \sum_{k=1, k \neq t}^K (1 - \alpha_k)(\psi(1) - \psi(\alpha_0)) \\
&\quad + \left(\left(\sum_{k=1, k \neq t}^K \alpha_k \right) - (K - 1) \right) ((\psi(\alpha_0 - (K - 1)) - \psi(\alpha_0)))
\end{aligned} \tag{3.12}$$

which does not allow the interpretation of minimizing the uncertainty cross-entropy objective.

Furthermore, we can directly consider results from Malinin et al. [MG19] as the only difference is the parameterization of the value of the concentration parameter corresponding to the

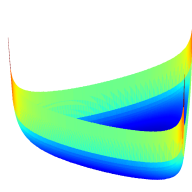


Figure 3.3.: Induced target Dirichlet distribution for the forward KL-divergence.

target class t in Equation (3.10). Instead, Malinin et al. [MG19] use a fixed value for the in-distribution dataset as discussed in Equation (2.14). From results in Malinin et al. [MG19], we know that the KL divergence induces a *mixture of Dirichlet distributions* in expectation

$$\mathcal{L}(\theta, \mathcal{D}) = \mathbb{E}_{(\mathbf{x}, y) \sim \mathcal{D}} \left[\text{KL} \left[\sum_{c=1}^C (\delta_{y,c}) p(\boldsymbol{\pi} \mid \boldsymbol{\beta}^{(c)}) \parallel p_{\theta}(\boldsymbol{\pi} \mid \mathbf{x}) \right] \right] \quad (3.13)$$

Due to the *forward* KL-divergence being *zero-avoiding*, Malinin et al. [MG19] conclude that forward KL divergence objective induces a target distribution with probability mass distributed over all modes in the presence of significant data uncertainty, i.e., when multiple classes are feasible for an data point. Thus, the induced target becomes a Dirichlet distribution with "inverted" shape having low precision as shown in Figure 3.3. However, we aim for EPN to assign density to a single mode within the Dirichlet similar to DPN in Figure 2.1 to enable consistent uncertainty estimation.

Finally, the entropy term in Equation (3.9) acts as a regularizer ensuring smoothness of the predicted Dirichlet distribution $p_{\theta}(\boldsymbol{\mu} \mid \mathbf{x})$.

3.2.2. Properties of Energy-Prior Network

After specifying the model and investigating its training, we explore the characteristics of EPN. Hein et al. [HAB19] discovered that neural networks with ReLU activations converge to high confidence predictions far from the training data. Further, Ulmer et al. [UC21] prove based on results in Hein et al. [HAB19] that various uncertainty measures discussed in Section 2.2.4, i.e., the class variance, predictive entropy, and approximate mutual information, converge to fixed scores. In the following, we demonstrate that EPN does not suffer such issues even for data far from the training data distribution.

To show this, consider a trained EPN $E_{\theta} : \mathbb{R}^D \mapsto \mathbb{R}^C$ where the energy increases for inputs $\gamma \odot \mathbf{x}, \gamma \in \mathbb{R}$

$$\lim_{\gamma \rightarrow \infty} E_{\theta}(\gamma \odot \mathbf{x}) = \infty \quad (3.14)$$

This is a reasonable assumption since the objectives used for training the underlying EBM embedded within EPN in Section 2.3.2 are consistent in the limit [SK21].

As a consequence of the definition of an EBM, the marginal density $p_\theta(\mathbf{x})$ learned by the model decreases as one moves from the training data:

$$\lim_{\gamma \rightarrow \infty} \exp(-E_\theta(\gamma \odot \mathbf{x})) = \lim_{\gamma \rightarrow \infty} \tilde{p}_\theta(\gamma \odot \mathbf{x}) \quad (3.15)$$

$$= 0 \quad (3.16)$$

Thus, one obtains for the concentration parameters $\alpha = [\alpha_1, \dots, \alpha_C]$ of the Dirichlet distribution in Section 3.2 parameterizing the posterior $p(\mu \mid \mathbf{x}, \theta)$

$$\lim_{\gamma \rightarrow \infty} \alpha_c = \lim_{\gamma \rightarrow \infty} \alpha_c^{\text{prior}} + \hat{\alpha}_c \quad (3.17)$$

$$= \alpha_c^{\text{prior}} + \underbrace{\lim_{\gamma \rightarrow \infty} \exp(f_\theta(\gamma \odot \mathbf{x})[c])}_{=0} \quad (3.18)$$

$$= \alpha_i^{\text{prior}} \quad (3.19)$$

which corresponds to a flat Dirichlet distribution for our choice of prior $\alpha^{\text{prior}} = \mathbf{1}$. Thus, the *distributional uncertainty* as measured by differential entropy is maximal, as desired for OOD inputs.

Furthermore, for the expected predictive distribution, we obtain

$$p(y \mid \mathbf{x}, \theta) = \int p(y \mid \mu) p(\mu \mid \mathbf{x}, \theta) d\mu \quad (3.20)$$

$$= \frac{\alpha_y}{\sum_i \alpha_i} \quad (3.21)$$

$$= \frac{1}{C} \quad (3.22)$$

Thus, EPN converges to a uniform prediction over the classes far from the training data. This allows reliable uncertainty estimates for OOD data since, in contrast to ReLU networks for classification [HAB19], the predictive distribution converges to a maximally uncertain prediction. For example, the *maximum softmax probability* score [LPB17; HG17] for EPN becomes $\max p_\theta(y \mid \mathbf{x}) = 1/C$ which is the lowest possible, indicating maximum uncertainty.

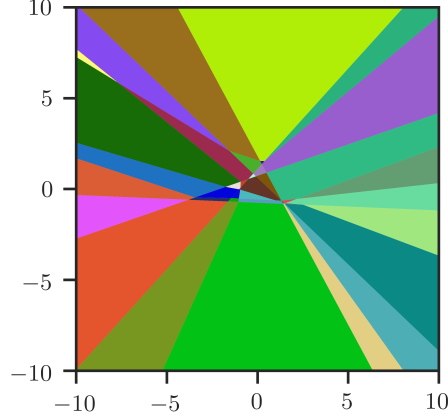


Figure 3.4.: Visualization of the regions in \mathbb{R}^2 on which the output of a 2-layer ReLU-network is an affine transformation of the input. We use code from Jordan et al. [JLD19] for plotting.

3.2.3. Enforcing asymptotic behavior

In Equation (3.14), we assume that the energy increases far from the training data based on the consistency of the EBM training approaches [SK21]. However, we can consider a slight adaptation of the neural network architecture to enforce this behavior. This change provably ensures that the energy $E_\theta(\mathbf{x})$ increases and thus the density $p_\theta(\mathbf{x})$ defined by the EBM decreases moving away from the training data. For this, we consider ReLU-networks [HAB19], i.e., neural networks using ReLU or LeakyReLU activations only. Originally, Meinke et al. [MBH21] introduce the considered parameterization to ensure that the classifier converges to uniform predictions over classes far from the training data.

Similar to Meinke et al. [MBH21], we use an established result by Hein et al. [HAB19] which shows that by scaling a datapoint, one arrives at a region (convex polytope), extending to infinity, on which the output of the ReLU-network is an affine transformation of the input. For a visualization of the polytopes of a simple 2-layer neural network, see Figure 3.4. Note that the outermost polytopes extend to infinity.

Lemma 1 ([HAB19]). *Let $\{Q_r\}_{r=1}^R$ be the set of convex polytopes associated with the ReLU-network $f : \mathbb{R}^D \mapsto \mathbb{R}^C$ such that for every $k \in \{1, \dots, R\}$ and $\mathbf{x} \in Q_k$, there exists $V^k \in \mathbb{R}^{C \times D}$ and $\mathbf{d}^k \in \mathbb{R}^C$ with $f(\mathbf{x}) = V^k \mathbf{x} + \mathbf{d}^k$. For any $\mathbf{x} \in \mathbb{R}^D, \mathbf{x} \neq 0$ there exists $\alpha \in \mathbb{R}$ and $t \in \{1, \dots, R\}$ such that $\beta \mathbf{x} \in Q_t$ for all $\beta \geq \alpha$.*

Based on Lemma 1, the following theorem shows that the marginal energy $E_\theta(\mathbf{x})$ for a JEM with a slightly adapted architecture increases as one moves away from the training data. Correspondingly, this means that the marginal data density $p_\theta(\mathbf{x})$ decreases as one would expect from any reasonable density estimate.

Theorem 1. Let $\mathbf{x} \in \mathbb{R}^D, \mathbf{x} \neq \mathbf{0}$ and let $g : \mathbb{R}^D \mapsto \mathbb{R}^K$ be a ReLU-network with parameters $\boldsymbol{\phi}$ where the last layer explicitly contains a ReLU activation. By Lemma 1, there exists a finite set of polytopes $\{Q_r\}_r$ on which g is affine. Denote by Q_t the polytope such that $\beta\mathbf{x} \in Q_t$ for all $\beta \geq \alpha$ with $\alpha \in \mathbb{R}$ and by $g(\mathbf{z}) = U\mathbf{z} + \mathbf{d}$ with $U \in \mathbb{R}^{K \times D}$ and $\mathbf{d} \in \mathbb{R}^K$ be the output of g for $\mathbf{z} \in Q_t$. Finally, let $f : \mathbb{R}^D \mapsto \mathbb{R}^C, f(\mathbf{x}) = Wg(\mathbf{x}) + \mathbf{b}$ be the Energy-based model where the last weight matrix $W \in \mathbb{R}^{C \times K}$ is component-wise negative and $\mathbf{b} \in \mathbb{R}^C$. If $U\mathbf{x} \neq \mathbf{0}$, then

$$\lim_{\beta \rightarrow \infty} E_{\theta}(\beta\mathbf{x}) = \lim_{\beta \rightarrow \infty} -\log \sum_{c=1}^C e^{(f(\beta\mathbf{x}))_c} = \infty$$

where $\theta = \{\boldsymbol{\phi}, W, \mathbf{b}\}$ are the learnable parameters.

Furthermore, $\lim_{\beta \rightarrow \infty} p_{\theta}(\beta\mathbf{x}) = 0$.

We proof this statement in Appendix A.1. Based on Theorem 1, we can achieve that the data density $p_{\theta}(\mathbf{x})$ defined by the EBM decays by ensuring that the last weight matrix of the ReLU-network is component-wise negative.

We find that leveraging this result is not necessary in our model since EPN always provided increasing energy in our experiments. However, we discover that Theorem 1 is useful for JEMs [Gra+20] in Section 4.2.2 to ensure that the density decreases.

4. Results

One focus of this chapter is to provide experimental evaluation of Energy-Prior Network (EPN) introduced in Chapter 3. We provide empirical analysis in Section 4.1. Secondly, we dive deeper into the density estimation capabilities of EBMs in Section 4.2 where we compare against Normalizing Flows as a density estimation baseline. Moreover, we investigate the reasons for OOD detection capabilities of EBMs in recent work [Gra+20; Gra+21].

4.1. Evaluation of Energy-Prior Network

In this section, we provide an experimental study of the properties of EPN. In particular, we demonstrate the characteristics of our model, established in Section 3.2.2, on a toy dataset. Further, we compare EPN against a model trained with cross-entropy loss as a baseline.

4.1.1. Toy Dataset

To investigate and visualize the properties of our model discussed in Section 3.2.2, we first consider a small toy dataset. This dataset consists of samples drawn from three Gaussian distributions as shown in Figure 4.1. The class labels correspond to the index of the Gaussian that produced a particular sample. The task is to classify the data points into the correct classes. To demonstrate the issues of the conventional approach for classification, we additionally compare against a model trained with cross-entropy objective introduced in Section 2.1 as a baseline. While this task is simple since the dataset is only two-dimensional, it allows us to visualize the behavior of a classification model in terms of its confidence and out-of-distribution detection capabilities.

Setup. We use an existing dataset from Charpentier et al. [CZG20] with 1500 samples uniformly generated from each Gaussian distribution $N(\boldsymbol{\mu}, \sigma \mathbb{I}_2)$. The means of the Gaussians $\boldsymbol{\mu}$ are $[0, 2]^T$, $[\sqrt{3}, -1]^T$, and $[-\sqrt{3}, -1]^T$, respectively, while the standard deviation is $\sigma = 0.2$. Each model uses 5 fully connected, hidden layers using ReLU activation with dimensionality 100, input size 2 and output size 3 corresponding to the three classes.

Cross-entropy baseline. We use a softmax activation on the logits and train the model using the cross-entropy objective. As expected, the accuracy converges to 100% quickly due to the

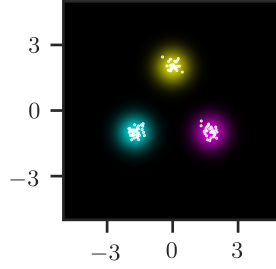


Figure 4.1.: Visualization of the 3-Gaussian dataset with a subset of the dataset samples plotted in white.

simplicity of the task. We proceed to investigate the uncertainty estimates and OOD detection scores.

Figure 4.2 shows the confidence $\max_y p_\theta(y | \mathbf{x})$ of the classifier. As recent theoretical results [HAB19] predict, the confidence increases when moving away from the training data, while confidence is low on the decision boundary only. When comparing with the dataset in Figure 4.1, the model predicts confidently on data it was not trained on, which potentially leads to confident, wrong predictions.

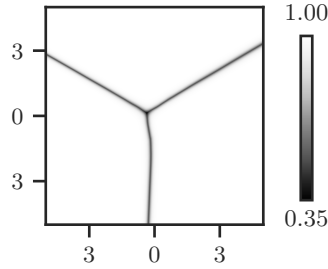


Figure 4.2.: Visualization of the confidence of the cross-entropy baseline.

Further, Figure 4.3 shows the unnormalized marginal and class-conditional densities for the cross-entropy baseline interpreted in the framework of W. Grathwohl et al. [Gra+20]. Note that the marginal data distribution $\tilde{p}_\theta(\mathbf{x})$ increases with larger distance to the training data. As a result, one is not able to detect OOD data based on the density. Note that this is also holds for the recently proposed energy score $E_\theta(\mathbf{x})$ [Liu+20b] in Section 2.3.3 which relates to the visualized quantity as $\tilde{p}_\theta(\mathbf{x}) = \exp(-E_\theta(\mathbf{x}))$.

Energy-Prior Network. On the other hand, we consider EPN. In contrast to the cross-entropy baseline, the confidence decreases for EPN with increasing distance to the training data as shown in Figure 4.4. Thus, the confidence, as a measure of total uncertainty, allows EPN to differentiate ID from OOD data. Moreover, the confidence is only high in the regions

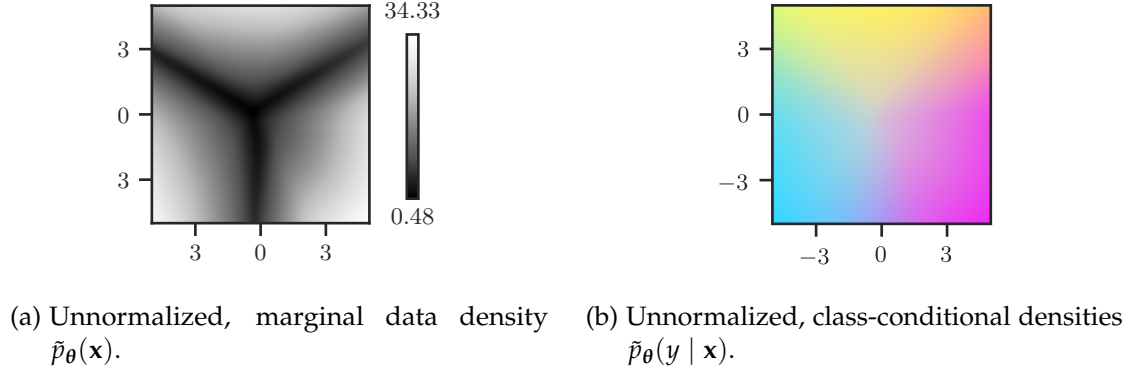


Figure 4.3.: Visualization of distributions of the cross-entropy baseline using the interpretation of logits in W. Grathwohl et al. [Gra+20]. Colors correspond to the different classes.

of the individual classes. As expected, the confidence is low in between the classes since it is unknown whether a sample in this region belongs to either class.

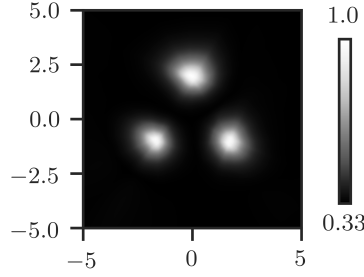


Figure 4.4.: Visualization of the confidence of EPN.

Similar results hold for the marginal and class-conditional distributions shown in Figure 4.5. The estimated distributions follow closely the underlying data generating distribution of the 3-Gaussians dataset in Figure 4.1. The result demonstrates that EPN produces satisfactory density estimates useful for OOD detection.

Additionally, we can leverage the view on EPN predicting the parameters of a Dirichlet distribution derived in Section 3.1 in order to estimate uncertainty. Therefore, we can, similar to DPN [MG18], consider the differential entropy to measure distributional uncertainty. In Figure 4.6, we observe that EPN is able to produce distributional uncertainty estimates which are low for regions with training data and increasing uncertainty for OOD data as desired.

Finally, we consider another version of the 3-Gaussian dataset in Figure 4.7. We move the Gaussian distributions closer together such that the Gaussians overlap on the borders, which introduces *data uncertainty* within the overlapping regions. As a result, we can use this dataset to investigate whether EPN can differentiate between different sources of uncertainty.

In Figure 4.8, we visualize the different types of uncertainty as introduced in Equation (2.3).

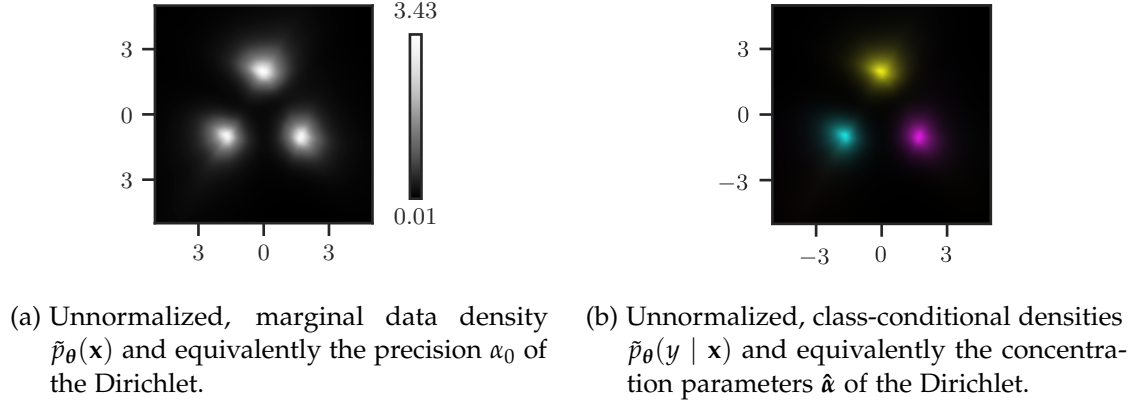


Figure 4.5.: Visualization of distributions of EPN which also corresponds to the parameters of the predictive Dirichlet distribution as shown in Section 3.1. Colors correspond to the different classes.

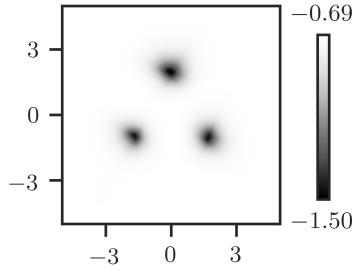


Figure 4.6.: Visualization of the differential entropy of EPN on the 3-Gaussians dataset.

For measuring *model uncertainty*, we use the mutual information between the categorical label and the Dirichlet prior $\mathcal{I}[y, \boldsymbol{\mu} | \mathbf{x}]$, for *data uncertainty*, we use the expected entropy under the Dirichlet prior $\mathbb{E}_{p(\boldsymbol{\mu} | \mathbf{x}, \mathcal{D})}[\mathcal{H}[p(y | \boldsymbol{\mu})]]$, and to measure the total uncertainty, we use the entropy of the predictive distribution $\mathcal{H}[p_\theta(y | \mathbf{x})]$.

We observe in Figure 4.8b that EPN is able to assign high data uncertainty to the overlapping regions as desired. Furthermore, the model uncertainty is low in the overlapping regions and high outside the data as shown in Figure 4.8a. This behavior is desired since the cause of uncertainty in the overlapping regions is the data generating process, i.e., the uncertainty is irreducible even when observing more data points. Overall, we conclude that EPN can estimate different types of uncertainties on the toy dataset.

4.1.2. Out-of-distribution detection

After demonstrating that EPN can provide accurate density and uncertainty estimates on the toy dataset, we evaluate the capability of EPN at detecting OOD inputs and compare with

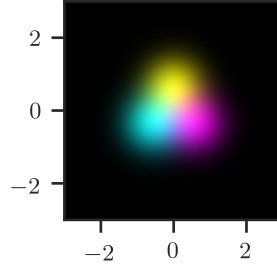


Figure 4.7.: Variant of the 3-Gaussians dataset with overlapping classes.

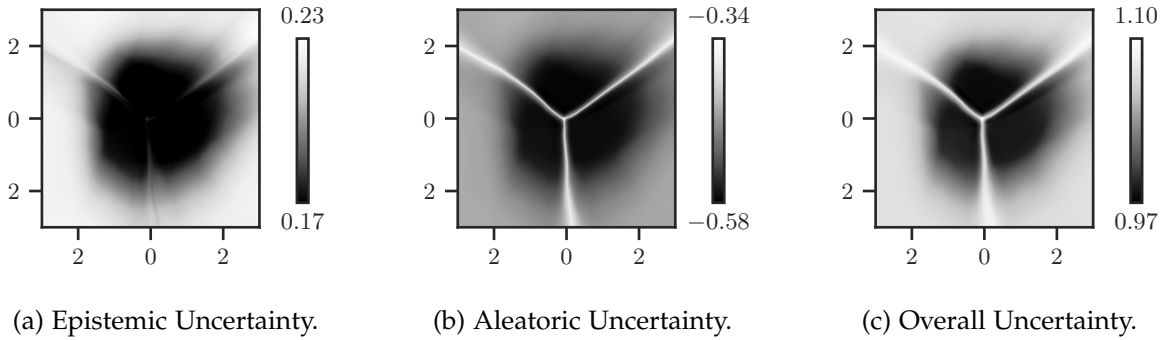


Figure 4.8.: Different types of uncertainty estimated by EPN.

other methods in the literature on more realistic datasets. For evaluation, we train models on one dataset and then test the capability of the model to detect samples from other datasets. We consider OOD detection as a binary classification problem with labels 1 for ID and 0 for OOD and report the Area under the Precision-Recall curve (AUC-PR) as commonly done in the literature [HG17].

Datasets. Following [CZG20], we consider the tabular datasets *Sensorless drive* [DG17] and *Segment* [DG17], with dimensionality 18 and 49, and 4 and 11 classes, respectively. To obtain a representative OOD dataset, we remove one class (*sky*) from the *Segment* and two classes (10, 11) from the *Sensorless drive* dataset.

Further, we evaluate on image datasets. We use FMNIST [XRV17] as ID dataset and MNIST [Lec+98], NotMNIST [Bul11], KMNIST [Cla+18] as OOD datasets. Further, we train on CIFAR-10 [Kri09] and use LSUN [Yu+16], Textures [Hua+20], CIFAR-100 [Kri09], SVHN [Net+11] and Celeb-A [Liu+15] as out-of-distribution.

Finally, we generate OOD datasets with *Noise*, *Constant* samples and an *OODomain* dataset as proposed by Charpentier et al. [CZG20], where the input data is not normalized into the range $[0, 1]$. We visualize samples in Figure 4.9. For the *Noise* dataset, we use an equal amount of samples from a standard normal distribution $N(0, 1)$ and an uniform distribution $\mathcal{U}(-1, 1)$.

The *Constant* dataset is sampled by drawing a scalar from $\mathcal{U}(-1, 1)$ and then filling a tensor with the same shape as the input data with that value. Finally, *OODomain* inputs are the SVHN dataset and KMNIST dataset, where we apply no normalization for the in-distribution datasets of CIFAR-10 and FMNIST, respectively. As a result, the data is in the range $[0, 255]$.

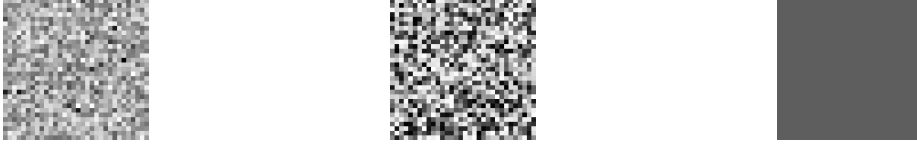


Figure 4.9.: Examples for the Gaussian noise, Uniform noise, and Constant images.

Baselines. We compare EPN with the baseline of a classifier trained with cross-entropy objective (*CE Baseline*). Further, we compare against several state-of-the-art approaches for OOD detection also considered in Chapter 2: *EnergyOOD* [Liu+20b], JEM [Gra+20] (*JEM*), Outlier-Exposure [HMD19] (*OE*), Reverse Prior Networks [MG19] (*R-PriorNet*), *Ensemble* [LPB17], Monte Carlo Dropout [GG16] (*MC Dropout*), and Posterior Network [CZG20] (*PostNet*).

To perform OOD detection, we use the (inverse) variance of the predictions for sampling-based models (*Ensemble*, *MC Dropout*). *OE* and *PostNet* use the confidence $\max_y p(y | \mathbf{x}, \theta)$. For *EnergyOOD*, *JEM* and EPN, we use the marginal energy $E_\theta(\mathbf{x})$ which is equal to the unnormalized probability in EBMs $\tilde{p}_\theta(\mathbf{x})$. Finally, *R-PriorNet* uses the differential entropy $\mathcal{H}(p(\boldsymbol{\mu} | \mathbf{x}, \theta))$ to determine distributional uncertainty. We consider differential entropy for EPN as well to demonstrate that EPN provides consistent distributional uncertainty estimates.

For all models, we use 5-layer Multi-Layer Perceptrons (MLPs) with ReLU activations and hidden layers with dimensionality 100 on the tabular datasets and WideResNet-16-8 [ZK16] for the image datasets. We train each approach with 5 different random seeds except for the Ensemble model where we use $M = 5$ models to form the Ensemble. For *PostNet*, we use aforementioned encoder networks mapping to a latent space of dimensionality 10. We then fit Normalizing Flow models with Radial transforms [RM15] of depth 8 on the latent space. We use a Dropout rate of $p = 0.3$ for the *MC Dropout* models as recommended in Gal et al. [GG16]. For the models which require an OOD dataset for training (*EnergyOOD*, *OE*, *R-PriorNet*), we use uniform noise $\mathcal{U}(0, 1)$. Uniform noise as OOD dataset ensures a fair comparison since a real OOD dataset might not be available in practice. We provide additional training details in Appendix A.2.

Results. We show the AUC-PR for OOD detection on the Segment dataset in Table 4.1 and for the FMNIST dataset in Table 4.2. We observe that EPN is able to perform similarly to other methods on these datasets using the marginal density as an OOD score as well as using differential entropy. We provide additional results on the CIFAR-10 and Sensorless dataset in Appendix A.3.

Table 4.1.: AUC-PR for OOD detection on the Segment dataset.

Model	OOD dataset Score	Constant	Noise	Segment OOD
CE Baseline	$\max p(y \mid \mathbf{x})$	51.27 ± 3.88	41.05 ± 2.49	50.6 ± 7.04
EnergyOOD	$p_{\theta}(\mathbf{x})$	97.74 ± 0.37	100.0 ± 0.0	99.98 ± 0.02
Ensemble	Variance	92.95	81.5 ± 0.47	74.31
JEM	$p_{\theta}(\mathbf{x})$	99.71 ± 0.05	99.99 ± 0.03	99.94 ± 0.08
MC Dropout	Variance	93.05 ± 0.58	55.92 ± 2.76	52.23 ± 11.46
OE	$\max p(y \mid \mathbf{x})$	96.46 ± 0.05	99.99 ± 0.01	91.44 ± 1.21
PostNet	$\max p(y \mid \mathbf{x})$	100.0 ± 0.01	100.0 ± 0.0	100.0 ± 0.0
R-PriorNet	$\mathcal{H}(p(\boldsymbol{\mu} \mid \mathbf{x}, \boldsymbol{\theta}))$	98.96 ± 0.25	100.0 ± 0.0	99.93 ± 0.1
EPN-M	$\mathcal{H}(p(\boldsymbol{\mu} \mid \mathbf{x}, \boldsymbol{\theta}))$	99.64 ± 0.24	100.0 ± 0.0	99.51 ± 0.69
	$p_{\theta}(\mathbf{x})$	99.97 ± 0.03	100.0 ± 0.0	99.96 ± 0.05
EPN-V	$\mathcal{H}(p(\boldsymbol{\mu} \mid \mathbf{x}, \boldsymbol{\theta}))$	100.0 ± 0.0	100.0 ± 0.0	93.2 ± 0.94
	$p_{\theta}(\mathbf{x})$	100.0 ± 0.0	100.0 ± 0.0	97.49 ± 0.97

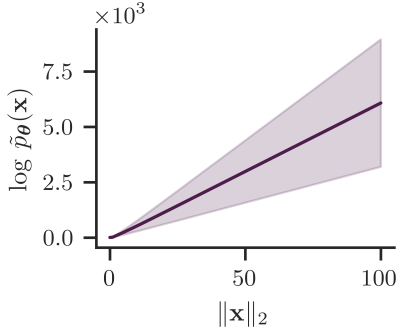
Overall, we conclude that indeed the (distributional) uncertainty estimates provided by EPN are consistent with its density estimates for detecting OOD samples. This result encourages that the connection, we derived between EBMs and Dirichlet Prior Network in Equation (3.2), is meaningful. Further, note that EPN is able to outperform JEM which does use EBM training while lacking the interpretation of logits as concentration parameters of a Dirichlet distribution. Interestingly, *R-PriorNet* is very competitive with EPN despite using uniform noise as OOD training data. We expect EPN to clearly outperform *R-PriorNet* based on using the guided process of EBM training instead of randomly sampling. However, in our experiments this advantage shows only on the *OODomain* dataset.

Next, we like to raise attention to the results of *EnergyOOD* in Table 4.2. *EnergyOOD* uses the same score as EPN, i.e., the marginal unnormalized probability $\tilde{p}_{\theta}(\mathbf{x})$, and is able to perform similarly to EPN except on the *OODomain* dataset.

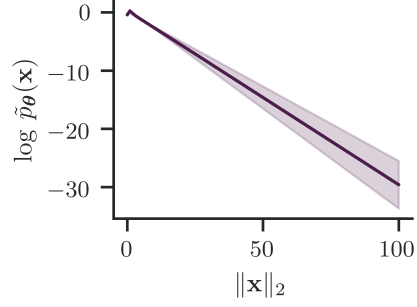
In Figure 4.10, we find that *EnergyOOD* assigns increasing density for inputs moving away from the training data, causing bad performance on the *OODomain* dataset. We hypothesize that the objective in Equation (2.51) of *EnergyOOD* does not ensure that the energy function converges to the groundtruth density. That is since their objective is motivated from a contrastive learning point of view and is not provably consistent as the EBM training approaches in Section 2.3.2. Further, since the unnormalized probability for *EnergyOOD* increases exponentially in the observed domain in Figure 4.10a, we can assume that $\tilde{p}_{\theta}(\mathbf{x})$ increases indefinitely. This means that *EnergyOOD* does not obtain a valid distribution in terms of the learned energy function since the normalizing constant $Z(\boldsymbol{\theta})$ becomes ∞ . Thus, our finding conflicts with the probabilistic arguments in W. Liu et al. [Liu+20b] which assume that a valid distribution $p_{\theta}(\mathbf{x})$ is learned.

Table 4.2.: AUC-PR for OOD detection on the FMNIST dataset.

Model	OOD dataset Score	KMNIST	MNIST	NotMNIST	Constant	Noise	OODomain
CE Baseline	$\max p(y \mathbf{x})$	97.54 ± 0.17	88.35 ± 0.38	88.56 ± 0.86	98.15 ± 0.5	87.07 ± 1.6	33.71 ± 0.24
EnergyOOD	$p_\theta(\mathbf{x})$	100.0 \pm 0.0	88.81 ± 1.62	93.89 ± 1.66	100.0 \pm 0.0	82.67 ± 1.86	30.69 ± 0.0
Ensemble	Variance	49.35	53.03	48.64	65.17 ± 20.3	53.54	97.98
JEM	$p_\theta(\mathbf{x})$	48.94 ± 3.66	78.75 ± 9.06	79.24 ± 6.95	45.33 ± 17.65	67.4 ± 11.0	95.14 ± 6.88
MC Dropout	Variance	92.12 ± 0.79	90.87 ± 0.74	90.54 ± 0.25	95.82 ± 0.52	90.88 ± 0.56	57.12 ± 4.6
OE	$\max p(y \mathbf{x})$	97.46 ± 0.87	83.1 ± 0.24	86.3 ± 5.15	100.0 \pm 0.0	90.52 ± 1.08	32.65 ± 0.2
PostNet	$\max p(y \mathbf{x})$	97.25 ± 0.2	95.14 \pm 1.16	93.18 ± 0.76	98.93 ± 0.72	93.45 ± 0.14	100.0 \pm 0.0
R-PriorNet	$\mathcal{H}(p(\boldsymbol{\mu} \mathbf{x}, \boldsymbol{\theta}))$	96.7 ± 0.67	94.52 ± 0.64	95.98 \pm 0.28	100.0 \pm 0.0	93.91 ± 2.65	71.12 ± 5.31
EPN-M	$\mathcal{H}(p(\boldsymbol{\mu} \mathbf{x}, \boldsymbol{\theta}))$	94.2 ± 0.55	93.4 ± 1.92	87.51 ± 0.31	100.0 \pm 0.0	97.37 \pm 0.35	100.0 \pm 0.0
	$p_\theta(\mathbf{x})$	79.9 ± 0.1	91.84 ± 3.45	78.36 ± 3.18	100.0 \pm 0.0	97.03 ± 0.37	100.0 \pm 0.0
EPN-V	$\mathcal{H}(p(\boldsymbol{\mu} \mathbf{x}, \boldsymbol{\theta}))$	94.97 ± 1.23	85.46 ± 2.57	90.51 ± 3.1	100.0 \pm 0.0	91.46 ± 0.35	100.0 \pm 0.0
	$p_\theta(\mathbf{x})$	94.31 ± 0.28	85.53 ± 1.32	89.69 ± 1.72	100.0 \pm 0.0	91.26 ± 0.25	100.0 \pm 0.0



(a) EnergyOOD



(b) EPN

Figure 4.10.: $\tilde{p}_\theta(\mathbf{x})$ for inputs \mathbf{x} moving away from the training data.

Finally, we qualitatively visualize the t-SNE [vdMH08] embeddings of the outputs of the penultimate convolutional layer of EPN together with the estimated unnormalized density in Figure 4.11. We observe that the individual classes of MNIST [LCB10] successfully cluster, while EPN assigns lower densities to KMNIST as the OOD dataset.

4.1.3. Detecting dataset shifts

A significant problem of neural networks in real applications is that the data distribution on which one evaluates the model might change during deployment. This phenomenon is known as *dataset shift* in the machine learning literature. Dataset shift results in degraded performance, however, is hard to detect in practice since the test dataset, which one uses to determine the model to deploy, might not be updated accordingly. Further, these perturbations

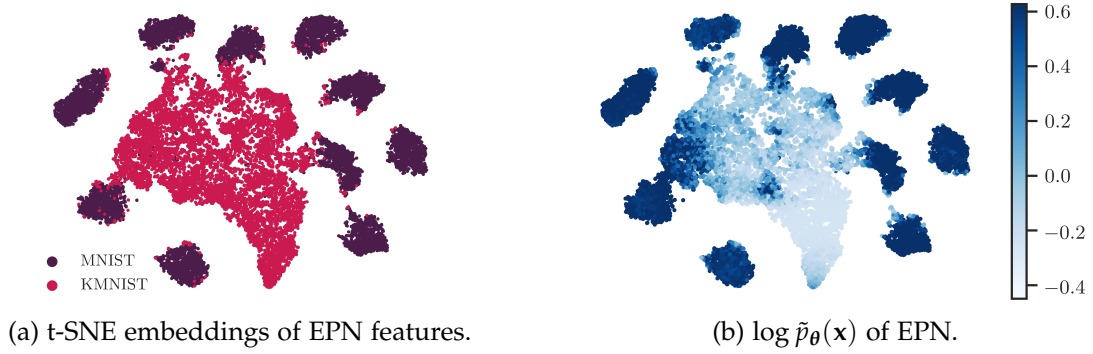


Figure 4.11.: Embeddings and respective density for MNIST vs. KMNIST datasets.

are often subtle and thus hard to detect.

In order to evaluate the models capability to detect dataset shifts, Hendrycks et al. [HD19] propose 15 dataset shifts based on various augmentations with 5 different severity levels of the CIFAR-10 dataset.



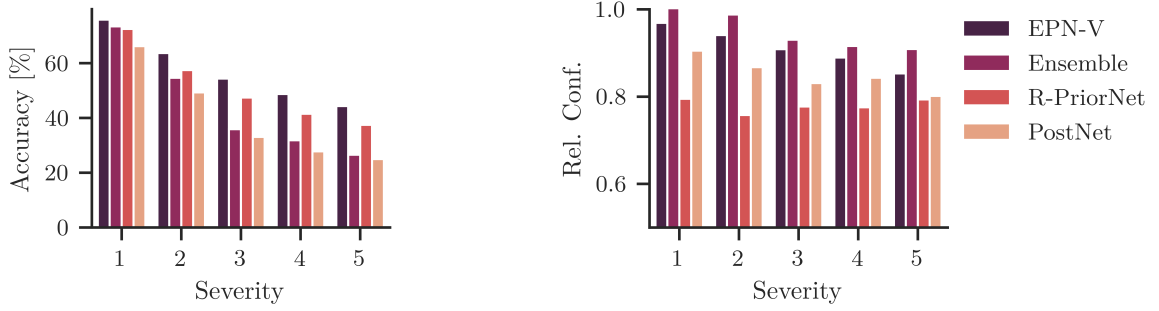
Figure 4.12.: Example of a dataset shift of the *fog* augmentation for severity 1 to 5.

We visualize the accuracy and respective relative confidence of EPN and various baselines in Figure 4.13. In Figure 4.13a, we observe that EPN is more robust than the baselines w.r.t. the dataset shifts since it retains higher accuracy even under augmentations with strong severity. Further, we find that the relative confidence decreases with the increasing severity of the dataset shift in Figure 4.13b.

We conclude that EPN is able to detect dataset shifts to a similar degree as *PostNet*. In particular, note that *R-PriorNet* does not provide proportional decreases in confidence w.r.t. the accuracy of the model. Concerning the better robustness of the classifier to dataset shifts, we hypothesize that the EBM training of EPN confronts the model not only with clean but also perturbed images leading to better robustness to the perturbations found in the considered dataset shifts.

4.1.4. Detecting adversarial examples

Another interesting case is to detect when one specifically changes inputs in a way that the classifier makes wrong predictions. These perturbed inputs, called adversarial examples, are often indistinguishable from real images as shown in Figure 4.14 but cause the classifier to make decisions that might be catastrophic in security-critical applications.



(a) Accuracy under dataset shifts.

(b) Confidence under dataset shifts.

Figure 4.13.: Accuracy and relative confidence for different models under dataset shift.

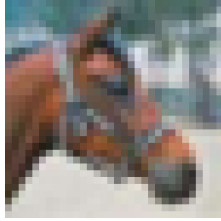
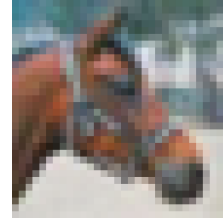
(a) Prediction: *Horse*(b) Prediction: *Truck*

Figure 4.14.: Example for adversarial attack with PGD on image (a) transformed to image (b).

We consider two common attacks, Projected Gradient Descent (PGD) [Mad+18] and Fast Gradient Method (FGM) [GSS15], with different attack budgets ϵ . Note that in general, FGM is a weaker attack than PGD. In order to investigate whether EPN can detect these adversarial inputs, we treat the adversarially perturbed images for the ID dataset as an OOD dataset and report AUC-PR as before in Section 4.1.2. Here, we consider *EPN-V* on the CIFAR-10 dataset.

We show the marginal density $\tilde{p}_\theta(\mathbf{x})$ for PGD attacked images over different attack budgets ϵ in Figure 4.15. For L_2 attacks, we observe that our model is able to detect attacks with some reliability based on the marginal density of EPN. However, L_∞ attacks with increasing ϵ lead to an increase in the density EPN assigns to adversarial samples and therefore adversarial examples become almost undetectable.

Table 4.3.: AUC-PR for adversarial attacks generated using PGD and FGM.

ϵ	L_∞			L_2		
	0.3	0.5	1.0	0.3	0.5	1.0
FGM	95.37	99.97	100.00	64.29	69.33	70.31
PGD	33.82	34.64	34.59	65.30	70.76	51.61

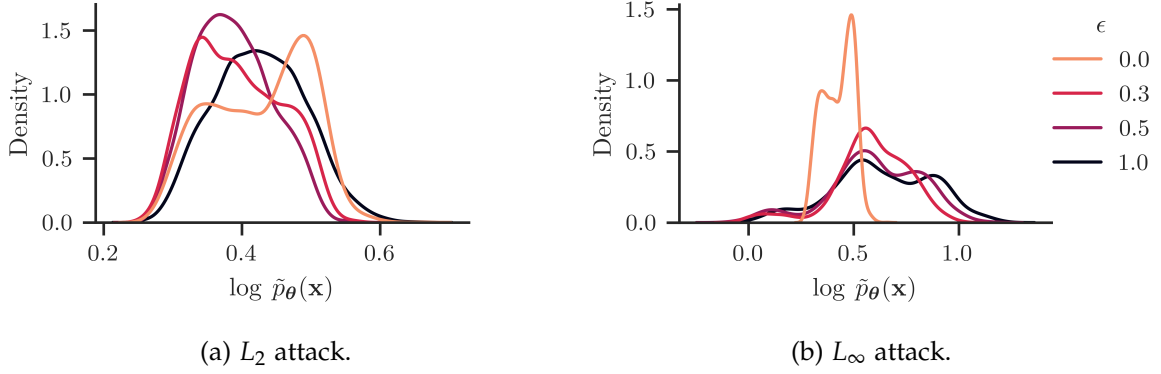


Figure 4.15.: Histograms of unnormalized density $\tilde{p}_\theta(\mathbf{x})$ for the clean dataset and with PGD adversarially attacked samples.

Table 4.4.: Accuracy (\uparrow) and calibration in terms of ECE (\downarrow).

	CIFAR-10		FMNIST		Segment		Sensorless	
	Accuracy	ECE	Accuracy	ECE	Accuracy	ECE	Accuracy	ECE
CE Baseline	92.26 ± 0.03	5.69 ± 1.16	93.99 ± 0.18	2.3 ± 0.27	97.22 ± 0.36	2.39 ± 0.98	98.6 ± 0.15	0.45 ± 0.14
EnergyOOD	90.85 ± 0.42	5.52 ± 0.78	93.82 ± 0.02	2.45 ± 0.49	97.47 ± 0.0	1.73 ± 0.5	96.32 ± 0.5	2.21 ± 0.0
Ensemble	93.35	16.22	94.39	16.71	96.97	15.73	99.12	18.78
JEM	88.44 ± 0.1	2.58 ± 0.01	91.75 ± 0.12	1.23 ± 0.08	96.72 ± 0.36	1.72 ± 0.01	98.33 ± 0.09	7.2 ± 0.03
MC Dropout	92.54 ± 0.35	3.98 ± 0.54	93.84 ± 0.03	2.33 ± 0.14	97.73 ± 0.36	0.98 ± 0.12	96.21 ± 0.43	2.13 ± 0.04
OE	91.02 ± 0.28	4.73 ± 0.45	93.98 ± 0.13	1.44 ± 0.18	97.98 ± 0.0	1.07 ± 0.29	99.12 ± 0.06	0.54 ± 0.05
PostNet	90.93 ± 0.06	2.71 ± 0.19	93.85 ± 0.36	0.75 ± 0.18	95.2 ± 0.36	27.7 ± 6.38	99.28 ± 0.04	1.08 ± 0.16
R-PriorNet	91.82 ± 0.45	83.3 ± 0.57	93.92 ± 0.05	72.17 ± 20.17	96.97 ± 0.71	84.48 ± 2.52	98.81 ± 0.21	91.38 ± 0.24
EPN-M	90.37 ± 0.03	17.32 ± 0.92	90.17 ± 0.09	15.26 ± 0.03	97.98 ± 0.71	1.58 ± 0.3	97.27 ± 0.81	2.78 ± 0.29
EPN-V	83.36 ± 0.42	68.81 ± 0.03	91.55 ± 0.03	76.37 ± 0.0	97.22 ± 0.36	4.13 ± 0.92	92.75 ± 0.18	12.52 ± 0.47

Additionally, we include AUC-PR results for FGM and PGD in Table 4.3. We find that EPN is able to provide a signal for detecting adversarial examples in all cases but attacks with PGD and L_∞ norm.

4.1.5. Classifier Evaluation

Next to the OOD detection capabilities, our model does provide competitive classification performance as well. For this, we evaluate the accuracy and calibration on the four datasets introduced in the previous section. To measure calibration, we consider the Expected Calibration Error (ECE) [Guo+17]. Intuitively, ECE measures whether a model reports meaningful confidences, e.g., if the model’s accuracy is 70%, it reports confidences of 70% on these samples.

In Table 4.4, we report the accuracy and the calibration in terms of ECE for EPN and the baselines models. Overall, we find that our model provides competitive discriminative results

comparable to the baselines. However, EPN is not calibrated in some cases, even comparing with the baseline cross-entropy model (*CE Baseline*). We investigate this behavior of EPN in the next section.

Tackling miscalibration. We find that underconfidence of EPN causes large calibration errors on some datasets. The underconfidence is a result of the normalizing constant $Z(\theta)$ of EPN being a free parameter. That is, $Z(\theta)$ can be scaled which causes the respective energy $E_\theta(\mathbf{x})$ to proportionally decrease or the unnormalized probability $\tilde{p}_\theta(\mathbf{x})$ to increase. This scaling affects the precision of the Dirichlet distribution, and the model becomes more or less confident depending on scaling the energy up or down.

One approach proposed in the literature to tackle this problem is temperature scaling [Guo+17]. For this, Guo et al. [Guo+17] learn a single parameter T to rescale the logits in the softmax activation. We adapt this approach for our case where the expected predictive distribution in Equation (3.20) for $T = 1$ is given as

$$p_\theta(y \mid \mathbf{x}, \theta) = \frac{\alpha^{\text{prior}} + \hat{\alpha}_y}{\sum_{y'} \alpha^{\text{prior}} + \hat{\alpha}_{y'}} \quad (4.1)$$

$$= \frac{1 + \exp(f_\theta(\mathbf{x})[y]/T)}{\sum_{y'} 1 + \exp(f_\theta(\mathbf{x})[y']/T)}. \quad (4.2)$$

In order to learn T , we use the validation set to minimize the negative log-likelihood between the groundtruth labels and the categorical distribution defined in Equation (4.1).

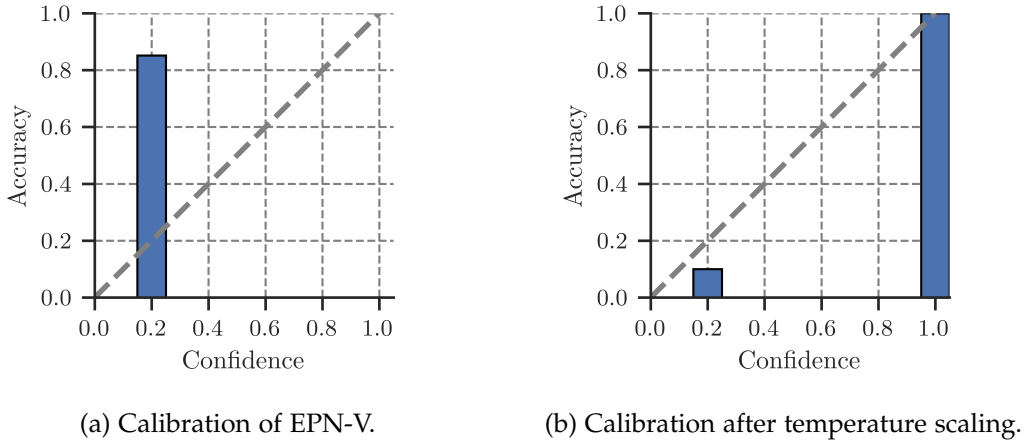


Figure 4.16.: Calibration curves of EPN-V before and after temperature scaling.

In Figure 4.16, we find that temperature scaling resolves the issues of underconfidence of EPN on the CIFAR-10 dataset.

Table 4.5.: Ablation experiments on the Sensorless dataset. Gray cells denote significant drops in performance.

	Classification	OOD Detection		
	Accuracy	Constant	Noise	Sensorless OOD
No $p_\theta(\mathbf{x})$	95.24 \pm 3.6	44.75 \pm 2.79	42.07 \pm 5.38	78.89 \pm 3.83
No $p_\theta(y \mathbf{x})$	10.81 \pm 0.58	100.0 \pm 0.0	100.0 \pm 0.0	94.71 \pm 0.64
Full model	93.21 \pm 4.21	99.99 \pm 0.0	99.99 \pm 0.0	95.57 \pm 1.87

4.1.6. Ablations

To determine the merit of individual components of EPN, we consider several ablation experiments on the Sensorless dataset.

In Table 4.5, we report the accuracy as well as OOD detection performance of EPN when omitting terms of the loss function proposed in Section 3.2.1. We observe that when omitting the optimization of the $p_\theta(\mathbf{x})$ term, the OOD detection severely degrades. Similarly, EPN is not able to perform classification without the KL divergence term optimizing $p_\theta(y | \mathbf{x})$ introduced in Equation (3.9). Further, we see small gains in OOD detection when leveraging additional supervised information on the *Sensorless OOD* dataset. We expand on this finding in Section 4.2.

4.1.7. Conclusion

In this section, we evaluated our proposed model EPN. We found that EPN can detect OOD samples with high accuracy, sometimes outperforming baselines. Further, we found that EPN can identify dataset shifts and adversarial examples with some fidelity. Finally, we evaluated the discriminative capabilities of EPN and found competitive results with the baselines in this setting. Additionally, we uncovered an issue with underconfident predictions of EPN on complex datasets, which we were able to resolve in parts through post-hoc calibration.

4.2. Investigation of OOD Detection with EBMs

In the second part of the experiments, we shift our focus from a particular model to an investigation of the general properties that allow superior OOD detection with EBMs. This is interesting since while EBMs, such as EPN proposed in this work and JEM [Gra+20], have shown good OOD detection performance based on the learned marginal density $p(\mathbf{x})$, other generative models, e.g., Normalizing Flows, struggle with that task.

In particular, Kirichenko et al. [KIW20] and Schirrmeister et al. [Sch+20] showed that Normalizing Flows are incapable of differentiating ID and OOD data on high-dimensional datasets

due to learning low-level features and those features being present in all natural images. To this end we provide similar analysis for the generative model class of EBMs

In particular, we verify the following hypotheses improving OOD detection with EBMs in recent works [Gra+20; Gra+21] compared to Normalizing Flows:

- **Dimensionality reduction.** The manifold hypotheses [FMN16] states that high dimensional data such as images reside on a low dimensional manifold. Normalizing Flows require invertible transformations and thus operate in the original data space. We hypothesize that this hinders OOD detection as they need to model off-manifold directions. Contrarily, there is no such restriction imposed on EBMs which allows to prune redundant dimensions without semantic content.
- **Supervision.** Kirichenko et al. [KIW20] and Schirrmeister et al. [Sch+20] show that Normalizing Flows learn low-level features without semantic meaning (smoothness, etc.). We hypothesize that label information encourages semantic, high-level features improving OOD detection.

Datasets. We use the datasets as described in Section 4.1.2. For the analysis in this section, we split the OOD datasets into groups according to their characteristics: *natural* and *non-natural* OOD datasets. Natural datasets include the data with samples from a similar domain as the ID, e.g., images from classes the model was not trained on. On the other hand, *non-natural* datasets contain irregular data patterns, e.g., noise. Note that the differentiation of *natural* and *non-natural* datasets allows evaluating distinct properties of the learned density: A model able to distinguish *natural* inputs can recognize semantic features of the high-level content of images, e.g., corresponding to classes, while *non-natural* inputs are easily detected semantically but lie farther away from the data manifold, thus, require the model to decrease the density when moving away from the data distribution.

Architectures. We use a 5-layer MLP with ReLU activations and hidden layers with dimensionality on the tabular datasets and WideResNet-10-2 [ZK16] for the image datasets. For the Normalizing Flow models on the image datasets, we use Glow [KD18] with $L = 3$ layers, $K = 32$ steps, and $C = 512$ channels. For the tabular datasets, we use 20 stacked radial transforms [RM15].

4.2.1. Are EBMs better than baselines in general?

Experiment 1. We establish baseline results by training EBMs and baseline models. In Table 4.6, we find that EBMs consistently outperform the *CE* baseline by 62.9%, 55.0%, and 36.4% for *CD*, *VERA*, and *SSM* respectively. The improvements are moderate in comparison to the Normalizing Flow baselines with 11.9%, 4.3%, and -4.3% respectively. Notably, improvements are mostly on *natural* datasets.

4. Results

Table 4.6.: AUC-PR for OOD detection on the respective ID datasets.

ID	CIFAR-10					FMNIST			Segment	Sensorless
OOD	CIFAR-100	CelebA	LSUN	SVHN	Textures	KMNIST	MNIST	NotMNIST	OOD	OOD
CE	62.76 \pm 1.46	64.47 \pm 2.44	65.18 \pm 5.79	47.51 \pm 4.58	39.17 \pm 2.28	69.07 \pm 6.73	82.5 \pm 12.27	50.9 \pm 6.73	33.35 \pm 1.82	33.02 \pm 1.32
NF	58.34	74.68	62.99	31.58	50.23	62.22	49.03	93.68	99.45 \pm 0.18	94.35
CD	50.51 \pm 2.13	43.86 \pm 5.85	54.43 \pm 11.37	60.72 \pm 24.59	76.21 \pm 17.44	50.52 \pm 9.39	31.69 \pm 0.9	76.85 \pm 2.66	98.18 \pm 2.18	72.83 \pm 16.19
SSM	53.82 \pm 3.12	57.72 \pm 7.0	52.79 \pm 3.16	45.75 \pm 7.24	48.82 \pm 4.34	58.98 \pm 5.48	67.86 \pm 11.4	57.27 \pm 13.73	79.43 \pm 24.29	67.14 \pm 20.31
VERA	55.95 \pm 2.68	73.97 \pm 2.63	67.39 \pm 2.57	37.27 \pm 4.66	46.29 \pm 8.1	78.11 \pm 21.05	67.53 \pm 21.63	76.22 \pm 22.11	94.63 \pm 7.22	45.66 \pm 10.55

ID	CIFAR-10			FMNIST			Segment		Sensorless	
OOD	Constant	Noise	OODomain	Constant	Noise	OODomain	Constant	Noise	Constant	Noise
CE	45.26 \pm 8.8	61.13 \pm 21.02	30.69 \pm 0.0	35.5 \pm 3.08	55.84 \pm 22.32	30.74 \pm 0.11	41.74 \pm 18.57	33.66 \pm 2.77	32.38 \pm 1.19	31.97 \pm 1.26
NF	30.87	83.65	100.0	71.07	98.04	100.0	99.95	100.0	100.0	100.0
CD	58.75 \pm 28.17	100.0 \pm 0.0	58.41 \pm 37.96	70.59 \pm 12.84	100.0 \pm 0.0	100.0 \pm 0.0	95.47 \pm 2.34	95.14 \pm 3.71	100.0 \pm 0.0	100.0 \pm 0.0
SSM	47.24 \pm 15.56	70.28 \pm 31.39	68.57 \pm 25.2	47.57 \pm 15.18	49.45 \pm 21.19	76.76 \pm 21.1	73.91 \pm 25.44	81.1 \pm 17.87	69.79 \pm 6.62	64.61 \pm 17.35
VERA	31.51 \pm 0.66	100.0 \pm 0.0	63.48 \pm 34.37	53.24 \pm 22.65	79.34 \pm 27.34	72.42 \pm 37.61	100.0 \pm 0.0	100.0 \pm 0.0	100.0 \pm 0.0	99.85 \pm 0.31

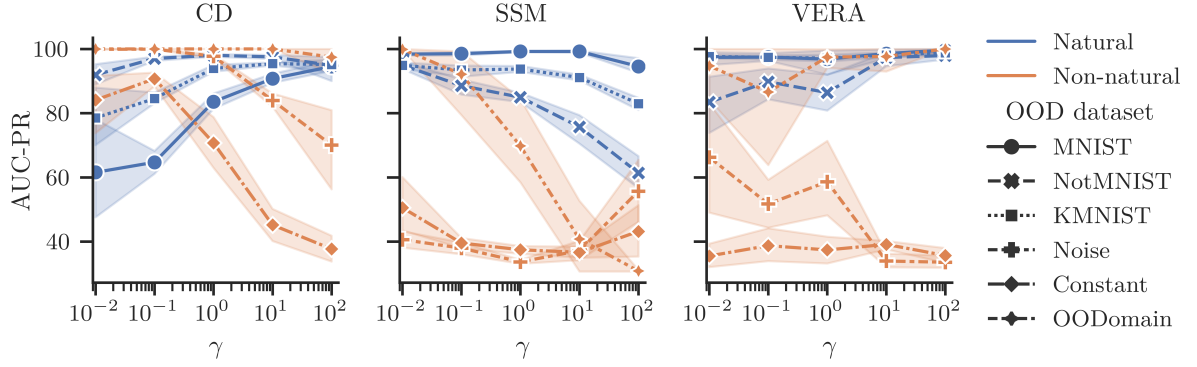


Figure 4.17.: AUC-PR for OOD detection for different settings of the weighting hyperparameter γ of the cross entropy objective. We use FMNIST as the ID dataset.

As EBMs perform dimensionality reduction since the EBM is specified by a function $\mathbb{R}^D \mapsto \mathbb{R}$ mapping to the scalar energy and do not consistently outperform Normalizing Flows in this experiment across all training methods, we conclude that dimensionality reduction plays a minor role in the OOD detection performance of recent EBMs [Gra+20]. Slight improvements on *natural* data can be attributed to the ability to discard non-semantic dimensions in EBMs.

4.2.2. Does supervision improve OOD detection?

Next, we consider two ways of incorporating labels to investigate the influence of supervision. Firstly, by applying an additional loss term as in [Gra+20] which affects the optimization directly, and secondly, performing density estimation on embeddings of a classification model which incorporates supervision indirectly through class-related features.

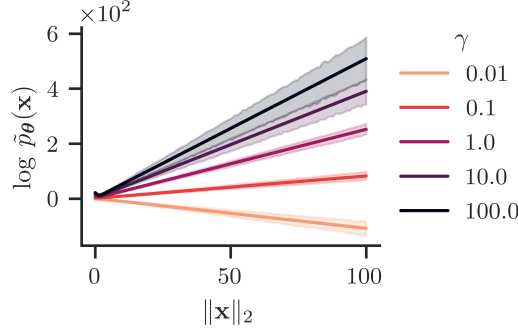


Figure 4.18.: Unnormalized density $\tilde{p}_\theta(\mathbf{x})$ of inputs with increasing L_2 -norm computed with models trained with SSM and supervision with different γ .

Experiment 2. We consider JEMs as introduced in Section 2.3.2 and apply a cross entropy objective with weighting hyperparameter γ optimizing $p_\theta(y | \mathbf{x})$.

In Table 4.7, we find substantial improvements in OOD detection on most datasets compared to the baseline models. Using label information within the model encourages discriminative features relevant for classification improving detection of *natural*, OOD inputs by 29.61%. These results indicate that EBM training tends to assign high-likelihood to all natural, structured images, an issue also observed in other generative models [Ren+19]. Note however that supervision decreases performance on some *natural* datasets and consistently worsens results at differentiating *non-natural* inputs (−11.74%).

Experiment 3. Investigating the difference in results between *natural* and *non-natural* datasets, we observe in Figure 4.17 that the OOD detection on *non-natural* images is negatively impacted by increasing the weighting γ of the cross-entropy objective. Additionally, we find that setting γ too high degrades performance at detecting *natural* OOD data in some cases as well. Further, we observe in Figure 4.18 that JEMs assign exponentially increasing density to data points far from the training data distribution for higher settings of γ , similar to results for the confidence in ReLU networks [HAB19].

As a result of the increasing density, *non-natural* inputs, which are farther from the training data than *natural* images, become increasingly harder to detect. Similar to the results of *EnergyOOD* in Section 4.1.2, we conclude that since the density increases indefinitely, the learned energy function probably **does not describe a valid distribution at all** as the normalizing constant $Z(\theta)$ in the EBM becomes ∞ . Intuitively, we hypothesize that this is caused by the cross-entropy objective "focusing" on the decision boundary only (see Figure 4.2). That is, since $L_{\text{CE}} = \sum_y \log p_\theta(y | \mathbf{x})$ is independent of $p_\theta(\mathbf{x})$. Thus, higher values of λ lead to relative less importance in optimizing $p_\theta(\mathbf{x})$ which is important for reliable OOD detection. This fact is demonstrated when comparing EPN with the cross-entropy baseline in Section 4.1.1.

Table 4.7.: % relative improvement in AUC-PR for OOD detection when using additional supervision during training.

Model	ID dataset	Natural	Non-natural
CD	CIFAR-10	-10.82	-9.11
	FMNIST	47.17	3.24
	Segment	1.85	0.89
	Sensorless	29.72	-0.02
SSM	CIFAR-10	7.33	-27.94
	FMNIST	50.61	-20.26
	Segment	25.89	-21.94
	Sensorless	22.13	-40.73
VERA	CIFAR-10	-1.16	-3.00
	FMNIST	33.66	-15.53
	Segment	4.98	-0.57
	Sensorless	97.93	0.07

Overall, we conclude that training with this factorization requires tuning of γ to achieve high OOD detection performance on both *natural* and *non-natural* inputs.

Tackling asymptotic behavior. In Section 3.2.3, we found that we can use a slightly adapted architecture to enforce increasing energy for EBMs far from the training data by ensuring that the last weight matrix has component-wise negative weights. Thus, we follow Meinke et al. [MBH21] and parameterize the elements of the weight matrix as $(W)_{ck} = -e^{(V)_{ck}}$ where $V \in \mathbb{R}^{C \times K}$.

We repeat *Experiment 3* and train the adjusted model with different settings of the weighting hyperparameter γ . In Figure 4.19, we find that our adjustments indeed leads to decaying density far from the training data for all values of γ compared to the prior results in Figure 4.18.

The guaranteed asymptotic convergence also contributes to the OOD detection results. In Table 4.8, we find that training the adjusted model with SSM and supervision leads to large, consistent improvements on the *non-natural* OOD data compared the model not leveraging Theorem 1 in Table 4.7. We explain this result with the intuition that *non-natural* data lies further away from the training data, thus, the asymptotic behavior plays a more important role.

Surprisingly, the OOD detection on CIFAR-10 improves with the adjusted model as well which cannot be explained by the asymptotic behavior alone. Thus, we hypothesize that the constraint, that enforces the asymptotic behavior, introduces some regularization into the EBM training. We leave the investigation of this observation for future work.

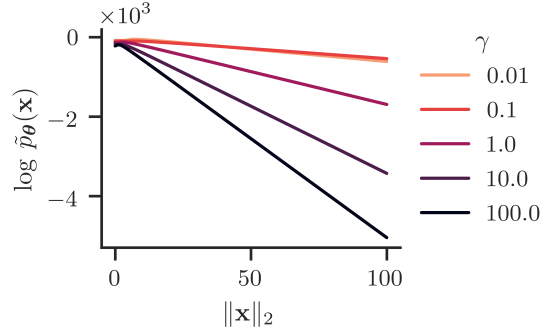


Figure 4.19.: Unnormalized density $\tilde{p}_\theta(\mathbf{x})$ of inputs with increasing L_2 -norm for EBMs with the adjusted architecture trained with different values of γ .

Table 4.8.: % relative improvement in AUC-PR for OOD detection with SSM training when using supervision and the parameterization with asymptotic guarantee.

Model	ID dataset	Natural	Non-natural
SSM	CIFAR-10	40.96	48.34
	FMNIST	50.48	78.07

Experiment 4. As an alternative, we sidestep the issue of tuning γ by following Kirichenko et al. [KIW20] who noticed that training Normalizing Flows on high-level features improves OOD detection. As EBMs do not require architectural restrictions, they should be able to extract these semantic features without additional processing. To investigate this behavior for EBMs, we store the features from a classifier trained with cross-entropy objective after convolutional layers. Subsequently, we train EBMs on these embeddings. Note that the dimensionality of the embeddings is not significantly lower than that of the input images. As a result, one cannot expect significant contributions from the dimensionality reduction capabilities of EBMs. For FMNIST, we obtain embeddings of size 640 while the original dimensionality is $28 \times 28 = 784$.

In Table 4.9, we observe that density estimation on embeddings significantly improves results on *natural* datasets compared to the baseline trained on images directly (+53.65%). Further, performance on *non-natural* datasets does not deteriorate and even increases by 10.98% on average with this approach.

As training on discriminative features directly improves OOD detection, this supports our hypotheses that EBMs trained on high-dimensional data such as images struggle to learn semantic features by themselves.

Table 4.9.: % relative improvement in AUC-PR for OOD detection when training on embeddings.

Model	ID dataset	Natural	Non-natural
CD	CIFAR-10	48.60	3.37
	FMNIST	95.79	-13.52
SSM	CIFAR-10	53.84	-2.31
	FMNIST	58.40	59.59
VERA	CIFAR-10	50.16	16.97
	FMNIST	15.12	1.80

Table 4.10.: % relative improvement in AUC-PR for OOD detection after introducing bottlenecks.

Model	ID dataset	Natural	Non-natural
CD	CIFAR-10	20.18	20.38
	FMNIST	67.95	10.88
SSM	CIFAR-10	14.76	33.34
	FMNIST	1.75	-5.92
VERA	CIFAR-10	19.66	33.22
	FMNIST	26.84	32.94

4.2.3. Can we encourage semantic features?

While EBMs inherently perform dimensionality reduction, the previous experiments suggest that this is insufficient to capture semantic features within the data. As shown by Kirichenko et al. [KIW20], introducing a bottleneck in the coupling transforms of Normalizing Flows enforces the network to learn semantic features improving OOD detection. One can also interpret this change in the frame of compression [Ser+20], i.e., one removes redundant information.

Experiment 5. To study the effect, we introduce bottlenecks after every block of the Wide-ResNet through a set of 1×1 convolutions mapping to $0.2 \times$ the original dimensionality. We experiment with different values of the downscaling factor and find 0.2 to yield the best results. However, other settings did improve OOD detection as well. We present the full results for other choices of the bottleneck factor in Table A.6.

In Table 4.10, we observe that this simple adjustment yields improvements in OOD detection on *natural* images for all training methods.

The bottlenecks force the network to compress the features, removing redundant information. Thus, the bottlenecks enable improved OOD detection and support the hypotheses that generic EBMs retain non-semantic features. We provide further investigation on low-level features in Section 4.2.4.

4.2.4. Low-level features in EBMs

In Section 4.2.2 and Section 4.2.3, we argue that supervision and bottlenecks encourage semantic features, while unsupervised EBMs learn generic local pixel correlations (low-level features) common to all *natural* images as shown by Schirrmeister et al. [Sch+20] which results in worse OOD detection.

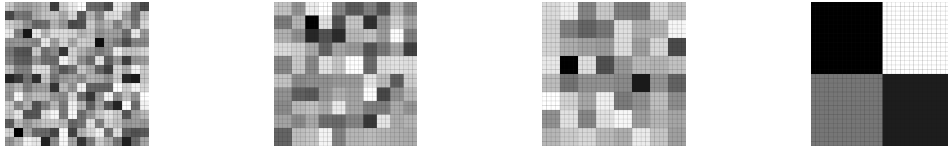


Figure 4.20.: Example images generated with pooling sizes 2, 3, 4, and 16. Note that the images become smoother with higher pooling sizes.

Experiment 6. To provide further evidence for our observation that low-level features affect the likelihood of unsupervised EBMs, we include density histograms for datasets with varying low-level features. We take inspiration from Serrà et al. [Ser+20] and generate images with varying smoothness properties, which Serrà et al. [Ser+20] show to affect the likelihood of samples in other generative models. To obtain images with different smoothness, we sample uniform noise at each pixel independently, apply average pooling with different pooling sizes, and resize to the original image dimensions with nearest neighbor upsampling. Images after this processing procedure are shown in Figure 4.20. Subsequently, we estimate the density of 1000 images generated at each smoothing fidelity under our models. Note that we use average pooling instead of max-pooling in Serrà et al. [Ser+20] since max-pooling leads to images with different statistics (higher mean) with increasing pooling sizes. Average pooling allows us to isolate the contribution of the change of smoothness independently of image statistics.

In Figure 4.21a, we observe that unsupervised EBMs assign higher likelihood to smoother versions of the dataset (corresponding to higher pooling sizes), while the supervised EBM is not affected by the change of low-level features in Figure 4.21b. This demonstrates that unsupervised EBMs are susceptible to low-level features affecting the likelihood of samples, while supervised EBMs rely on higher-level, semantic features to assign likelihoods.

In Figure 4.22a and Figure 4.22b, we investigate the effect of applying the bottleneck to the architecture of the unsupervised EBMs. We observe that the EBM with bottleneck assigns higher relative likelihood to the FMNST test set vs. the artificial noise datasets containing

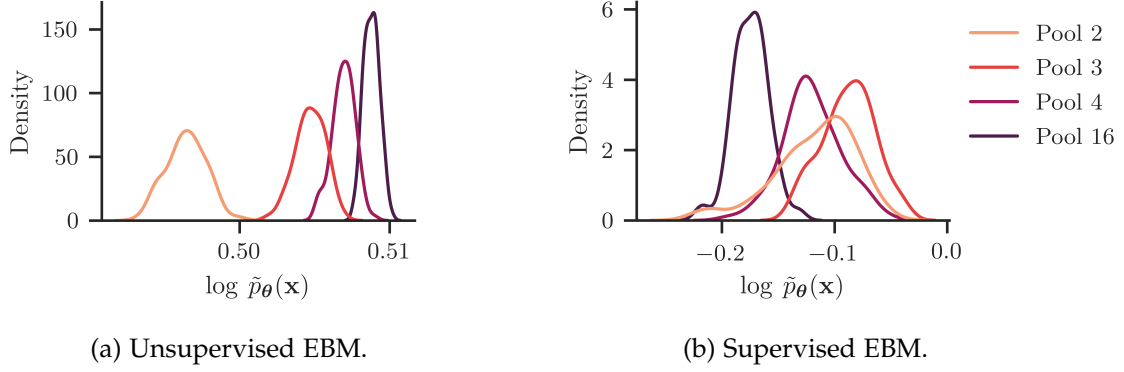


Figure 4.21.: Density histograms of generated dataset of noise images with different smoothness under different EBM. Higher pooling corresponds to higher smoothness of the input images as visualized in Figure 4.20.

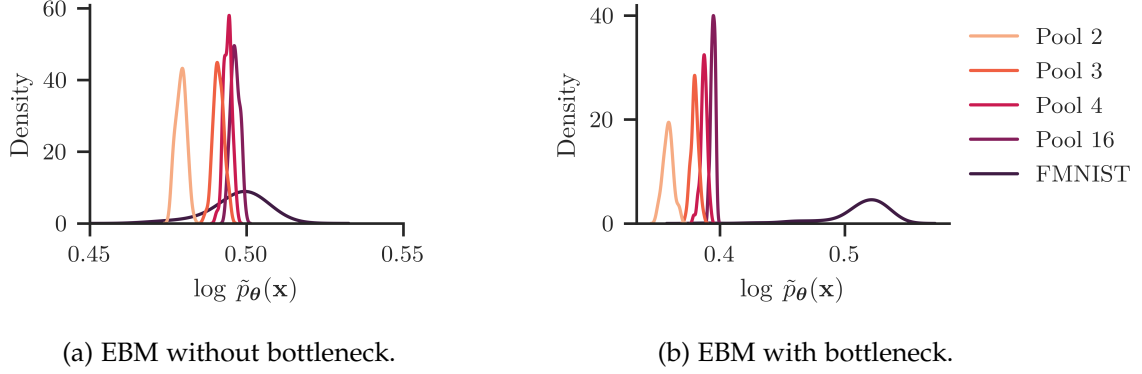


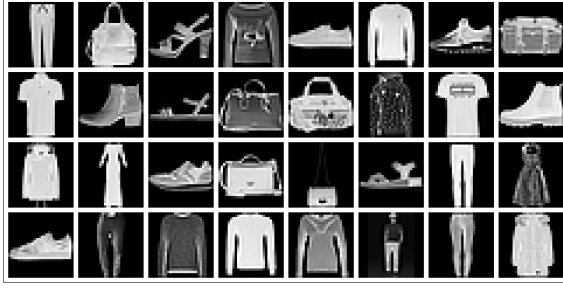
Figure 4.22.: Comparison of density histogram of ID test set of FMNIST vs. low-level features for unsupervised EBMs with and without bottleneck.

low-level features only. This supports our observation that including bottlenecks within the EBM helps the model to learn semantic features rather than local, low-level image correlations.

Experiment 7. Finally, we investigate images under the learned EBMs. Samples from the FMNIST dataset can be found in Figure 4.23a. We optimize the likelihood of these samples under the model and visualize samples for unsupervised EBM in Figure 4.23b and for supervised EBM in Figure 4.23c.

We observe that while the semantic content of samples under the unsupervised model becomes almost indistinguishable, the samples under the supervised model preserve their class semantics.

This result once more highlights that low-level features are the driving factor for high likelihood in unsupervised EBMs, while supervised EBMs learn a notion of semantics.



(a) Dataset samples.

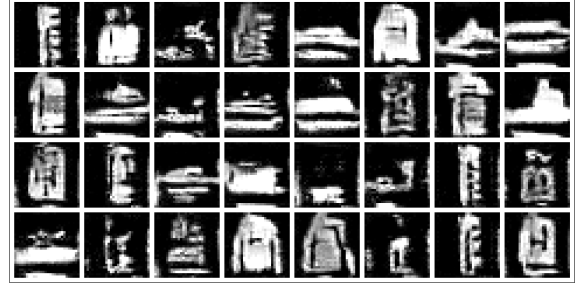
(b) Optimized samples under **unsupervised** EBMs.(c) Optimized samples under **supervised** EBMs.

Figure 4.23.: Comparison of samples from the FMNIST dataset.

4.2.5. Conclusion

Overall, we find that **(1)** EBMs struggle with OOD detection on high-dimensional data but to a lower degree than Normalizing Flows, **(2)** incorporating task-specific priors such as supervision significantly improves OOD detection on *natural* OOD data in line with what has been recently suggested by Lan et al. [LD21] and Schirrmeister et al. [Sch+20] for other generative models, and **(3)** architectural modifications can be used to improve the OOD detection performance.

5. Conclusion

We conclude this thesis by summarizing our contributions in Section 5.1 and providing ideas for future work in Section 5.2.

5.1. Summary

In this work, we derived a connection between Energy-based model and Dirichlet Prior Network (DPN). We then leverage this connection to define Energy-Prior Network (EPN) and an optimization scheme for training based on existing EBM training techniques. In comparison to Prior Networks, EPN does not require an OOD dataset or additional hyperparameters defining the target Dirichlet distribution during training. We then show the efficacy of EPN in detecting OOD samples, distribution shifts, and adversarial attacks.

In a second part of experiments, we investigate the overall properties enabling better OOD detection of EBMs versus other generative models. We find that unsupervised EBMs suffer similar problems as Normalizing Flows, however, one can use supervision and architectural modifications to improve the OOD detection performance.

5.2. Future Work

There are multiple avenues for improving or extending the ideas presented in this work. Concerning, EPN one could expand on the underconfidence issue presented in Section 4.1.5 and why this happens only in some cases. Based on initial observations regularizing the normalizing constant $Z(\theta)$ might provide a way forward.

Additionally, it would be interesting to investigate the issue of the energy increasing far from the training data when training with the factorization $p_{\theta}(\mathbf{x}, y) = p_{\theta}(y | \mathbf{x}) \times p_{\theta}(\mathbf{x})$ since both, JEMs [Gra+20] and EPN, use this type of factorization. In particular, other factorizations such as the joint $p_{\theta}(\mathbf{x}, y)$ could be a compelling direction since it might not lead to degenerate solutions. Initial results optimizing the joint distribution directly can be found in Kelly et al. [KG21]. In a similar vein, one could explore the observation in Section 4.2.2 that enforcing the asymptotic constraint on the energy using Theorem 1 improves the OOD detection with EBMs not only on *non-natural* but also *natural* OOD data.

Since EPN only relies on a point estimate of $p(\theta)$, estimating epistemic uncertainty is only possible on a limited basis. Thus, one could extend EPN with a full Bayesian treatment of

$p(\theta)$ such as deep ensembles [LPB17] or BNN [Mad+19].

Finally, regarding our findings in Section 4.2.3, investigating which and why some architectural modifications yield improved OOD detection in EBMs might yield further insights for learning high-level features in an unsupervised setting with EBMs.

A. General Addenda

In this chapter, we present the proof of Theorem 1 in Appendix A.1, additional details on the experiments in Appendix A.2, complementary results in Appendix A.3, and other research directions with initial results in Appendix A.4.

A.1. Proof of Theorem 1

Theorem 1. *Let $\mathbf{x} \in \mathbb{R}^D, \mathbf{x} \neq \mathbf{0}$ and let $g : \mathbb{R}^D \mapsto \mathbb{R}^K$ be a ReLU-network with parameters $\boldsymbol{\phi}$ where the last layer explicitly contains a ReLU activation. By Lemma 1, there exists a finite set of polytopes $\{Q_r\}_r$ on which g is affine. Denote by Q_t the polytope such that $\beta\mathbf{x} \in Q_t$ for all $\beta \geq \alpha$ with $\alpha \in \mathbb{R}$ and by $g(\mathbf{z}) = U\mathbf{z} + \mathbf{d}$ with $U \in \mathbb{R}^{K \times D}$ and $\mathbf{d} \in \mathbb{R}^K$ be the output of g for $\mathbf{z} \in Q_t$. Finally, let $f : \mathbb{R}^D \mapsto \mathbb{R}^C, f(\mathbf{x}) = Wg(\mathbf{x}) + \mathbf{b}$ be the Energy-based model where the last weight matrix $W \in \mathbb{R}^{C \times K}$ is component-wise negative and $\mathbf{b} \in \mathbb{R}^C$. If $U\mathbf{x} \neq \mathbf{0}$, then*

$$\lim_{\beta \rightarrow \infty} E_{\theta}(\beta\mathbf{x}) = \lim_{\beta \rightarrow \infty} -\log \sum_{c=1}^C e^{(f(\beta\mathbf{x}))_c} = \infty$$

where $\theta = \{\boldsymbol{\phi}, W, \mathbf{b}\}$ are the learnable parameters.

Furthermore, $\lim_{\beta \rightarrow \infty} p_{\theta}(\beta\mathbf{x}) = 0$.

The proof follows a very similar structure as the result in Meinke et al. [MBH21].

Proof. By Lemma 1, it holds that $\beta\mathbf{x} \in Q_t$ for $\beta \geq \alpha$. Thus, we can write the marginal energy as

$$E_{\theta}(\beta\mathbf{x}) = -\log \sum_{c=1}^C e^{(f(\beta\mathbf{x}))_c} \tag{A.1}$$

$$= -\log \sum_{c=1}^C e^{\langle (W)_c, U\beta\mathbf{x} + \mathbf{d} \rangle + (\mathbf{b})_c} \tag{A.2}$$

where $(W)_c$ denotes the c -th row of W .

We have $(g(\mathbf{x}))_i \geq 0$ for all $\mathbf{x} \in \mathbb{R}^D$ since the last layer of g contains a ReLU activation. Thus, it has to hold $(U\beta\mathbf{x} + \mathbf{d})_i \geq 0$ for all $\beta \geq \alpha$ and $i \in 1, \dots, K$. Therefore, $(U\mathbf{x})_i \geq 0$ and as

$U\mathbf{x} \neq 0$ there needs to exist a i^* with $(Ux)_{i^*} > 0$. Thus, for all $\beta \geq \alpha$ and $c \in \{1, \dots, C\}$ it holds

$$(f(\beta\mathbf{x}))_c = \langle (W)_c, U\beta\mathbf{x} + \mathbf{d} \rangle + (\mathbf{b})_c \quad (\text{A.3})$$

$$= \beta \langle (W)_c, U\mathbf{x} \rangle + \langle (W)_c, \mathbf{d} \rangle + (\mathbf{b})_c \quad (\text{A.4})$$

As $(W)_{ck} < 0$, i.e., W has strictly negative components, and $U\mathbf{x} > 0$, we have $\langle (W)_c, U\mathbf{x} \rangle < 0$ and thus

$$\lim_{\beta \rightarrow \infty} (f(\beta\mathbf{x}))_c = -\infty. \quad (\text{A.5})$$

Plugging into Equation (A.1) yields the result.

As $\lim_{\beta \rightarrow \infty} E_\theta(\beta\mathbf{x}) = 0$, we have

$$\lim_{\beta \rightarrow \infty} p_\theta(\mathbf{x}) = \lim_{\beta \rightarrow \infty} \frac{e^{-E_\theta(\beta\mathbf{x})}}{Z(\boldsymbol{\theta})} = 0 \quad (\text{A.6})$$

□

A.2. Training details

In this section, we provide further details on the training procedures and hyperparameters for individual methods in Chapter 4. Unless we specify otherwise, we use the Adam optimizer with default parameters $\beta_1 = 0.9$ and $\beta_2 = 0.999$. Further, we use learning rate warm-up with 2500 steps across all models. We train the models on the tabular datasets for 10,000 steps and on the image datasets for 50 and 100 epochs for the FMNIST and CIFAR-10 datasets, respectively. For the experiments in Section 4.2, we perform model selection based on the AUC-PR on an OOD validation dataset. For CIFAR-10, we use the validation sets of CelebA and CIFAR-100, while for FMNIST we use the validation sets of MNIST and KMNIST. For the tabular dataset, we use 10% of the hold-out OOD data for model selection. To obtain the results in Section 4.1, we use the accuracy for model selection. For all datasets, we use the original train/validation/test splits if available. In the other cases, we use 10% of the training set as the validation set.

Contrastive Divergence. Following [Gra+20; DM19], we use persistent contrastive divergence [Tie08] which significantly reduces computation time compared to seeding new chains at every iteration as in Nijkamp et al. [Nij+19]. For the parameters of the SGLD sampler, we use the settings of W. Grathwohl et al. [Gra+20], set the step size α to 1, and reinitialize

samples from the replay buffer with probability 0.05. The size of the buffer is 10000. In contrast to [Gra+20], we find that training with 20 SGLD steps consistently diverges, thus, we set the number of SGLD steps to 100 for tabular datasets and 30 for image datasets which leads to stable convergence in our experiments. Further, we set the initial learning rate to 0.001. Following Du et al. [DM19] and Nijkamp et al. [Nij+19], we add additive Gaussian noise with variance 0.1 to the inputs to stabilize training.

VERA. We use the default hyperparameters proposed in W. S. Grathwohl et al. [Gra+21] and initialize the variance of the variational approximation η with 0.1 while clamping η into the range $[0.01, 0.3]$ during training. We perform a grid search for the entropy regularizer in $[10^{-4}, 1]$ and find 10^{-4} to yield the best results in terms for training stability. Further, we set the learning rate of the EBM to $3 \cdot 10^{-4}$ and the learning rate of the generator to $6 \cdot 10^{-4}$. We use the Adam optimizer with parameters $\beta_1 = 0.0$ and $\beta_2 = 0.9$ to train the generator.

For the generator architecture, we use a 5-layer MLP with hidden dimension 100 and leaky ReLU activations with slope 0.2 for the tabular datasets. The latent distribution is a 16-dim. isotropic Normal distribution. For the image datasets, we follow [Gra+21] and use the generator from [Miy+18] based on ResNet [He+16] blocks with latent dimension 128.

Sliced Score Matching. We set the distribution p_v to a multivariate Rademacher distribution which enable the use of the variance reduced objective (SSM-VR) [Son+20]. That is, since one can compute the expectation $\mathbb{E}_{p_v} [\mathbf{v}^T \boldsymbol{\psi}_\theta(\mathbf{x})]^2 = \|\boldsymbol{\psi}_\theta(\mathbf{x})\|_2^2$ analytically [Son+20]. During training, we use a single projection vector \mathbf{v} from p_v to compute the objective.

Normalizing Flow. We train Normalizing Flow models with maximum likelihood and learning rate 10^{-3} . We perform early stopping based on the log-likelihood of the validation set with patience 10.

Cross-entropy classifier. We train the cross-entropy baseline with learning rate 10^{-3} on the tabular and 10^{-4} on the image datasets. Further, we use weight decay with weight 5×10^{-4} and perform early stopping based on the accuracy of the model.

EnergyOOD. For the *EnergyOOD* model, we use $m_{\text{in}} = -23$ and $m_{\text{out}} = -5$ as suggested in W. Liu et al. [Liu+20b] and set the weighting for the margin loss L_{Energy} to 0.1. We first train models based on a cross-entropy objective. Then, we finetune the model for 10 epochs on the image datasets with learning rate 10^{-4} and 10000 iterations with learning rate 10^{-3} on the tabular datasets. We perform model selection based on the the overall combined loss of cross-entropy and L_{Energy} .

Outlier-Exposure. For the *OE* model, we use a weighting of 0.5 for the L_{OE} loss term. Similar to *EnergyOOD*, we finetune models trained with cross-entropy loss for 10 epochs on the image datasets and 10000 iterations on the tabular datasets with the same learning rates.

Dirchlet Prior Network. For DPN, we use learning rate 10^{-4} on the image and 10^{-3} on the tabular datasets. Further, we set the concentration of the target class $\beta_y = 100$ and use the reverse KL divergence divergence training [MG19]. Finally, we use a weighting of 1 to balance the ID and OOD loss terms.

Posterior Network. We use learning rate 10^{-4} and use the class counts of the training dataset for the budget function. Further, we set the weight for the entropy regularizer to 10^{-5} . We set the dimensionality of the latent space to 10 and use 8 stacked radial transforms [RM15] for the Normalizing Flows. We perform model selection based on the accuracy.

Energy-Prior Network. For EPN, we use learning rate $3 \cdot 10^{-5}$ on the image datasets and 10^{-3} on the tabular datasets. We set the weighting of the KL divergence term to 1.0 for the *EPN-M* and 100.0 for the *EPN-V* model after performing grid search in $\{0.1, 1.0, 10, 100\}$. Further, we weight the entropy regularizer with 10^{-4} . For the EBM optimization, we use the default parameters of VERA for *EPN-V* and of contrastive divergence for *EPN-M*, as described before. We perform model selection based on the accuracy on the validation set.

A.2.1. Implementation & Configuration

We implement all models with PyTorch [Pas+19] and train on a single GPU with either *Nvidia GeForce RTX 2080Ti* or *Nvidia GeForce GTX 1080Ti*. We provide the full implementation of all models together with training configurations for reproducing the results in this work at <https://github.com/selflein/MA-EBM>.

A.3. Additional results

In this section, we add complementary results for the OOD detection with EPN in Section 4.1.2. OOD detection results for the Sensorless dataset, we add in Table A.1 and for the CIFAR-10 dataset in Table A.2. EPN remains competitive, however, we find that the *EPN-V* variant starts to outperform the *EPN-M* variant on the CIFAR-10 dataset. We explain this observation with better capabilities of VERA for estimating the marginal data distribution compared to Contrastive Divergence (CD) training with MCMC. These results are consistent with results in W. S. Grathwohl et al. [Gra+21] for JEM models.

For completeness in Section 4.2, we report the tables measuring OOD detection on *natural* datasets in Table A.4 and on *non-natural* datasets in Table A.5. Models with *-E* suffix

Table A.1.: AUC-PR for OOD detection on the Sensorless dataset.

Model	OOD dataset Score	Constant	Noise	Sensorless OOD
CE Baseline	$\max p(y \mathbf{x})$	35.93 ± 5.09	33.52 ± 1.38	40.02 ± 5.41
EnergyOOD	$p_{\theta}(\mathbf{x})$	100.0 ± 0.0	100.0 ± 0.0	97.7 ± 1.2
Ensemble	Variance	99.32	94.82 ± 0.59	77.72
JEM	$p_{\theta}(\mathbf{x})$	100.0 ± 0.0	100.0 ± 0.0	77.89 ± 12.39
MC Dropout	Variance	64.27 ± 9.1	52.45 ± 0.76	34.57 ± 0.17
OE	$\max p(y \mathbf{x})$	99.96 ± 0.01	100.0 ± 0.0	60.93 ± 17.18
PostNet	$\max p(y \mathbf{x})$	99.99 ± 0.01	99.99 ± 0.01	80.05 ± 1.45
R-PriorNet	$\mathcal{H}(p(\boldsymbol{\mu} \mathbf{x}, \boldsymbol{\theta}))$	99.99 ± 0.0	99.99 ± 0.0	85.18 ± 12.3
EPN-M	$\mathcal{H}(p(\boldsymbol{\mu} \mathbf{x}, \boldsymbol{\theta}))$	99.99 ± 0.0	99.99 ± 0.0	94.88 ± 2.82
	$p_{\theta}(\mathbf{x})$	99.99 ± 0.0	99.99 ± 0.0	95.57 ± 1.87
EPN-V	$\mathcal{H}(p(\boldsymbol{\mu} \mathbf{x}, \boldsymbol{\theta}))$	99.99 ± 0.0	98.05 ± 3.61	60.43 ± 0.91
	$p_{\theta}(\mathbf{x})$	99.99 ± 0.0	98.2 ± 3.36	82.48 ± 15.26

correspond to models trained on classifier embeddings, while models with the -S suffix correspond to models trained with additional supervision in the form of cross-entropy objective weighted with parameter $\gamma = 1$. We also present the full results of Section 4.2.3 for different choices of the bottleneck size in Table A.6.

In addition to the results for the effect of γ on OOD detection on FMNIST in Section 4.2.2, we add results for the Segment dataset in Figure A.1, the Sensorless dataset in Figure A.2 and CIFAR-10 in Figure A.3. Our main finding holds that the choice of γ heavily affects the OOD detection performance, particularly on high-dimensional datasets.

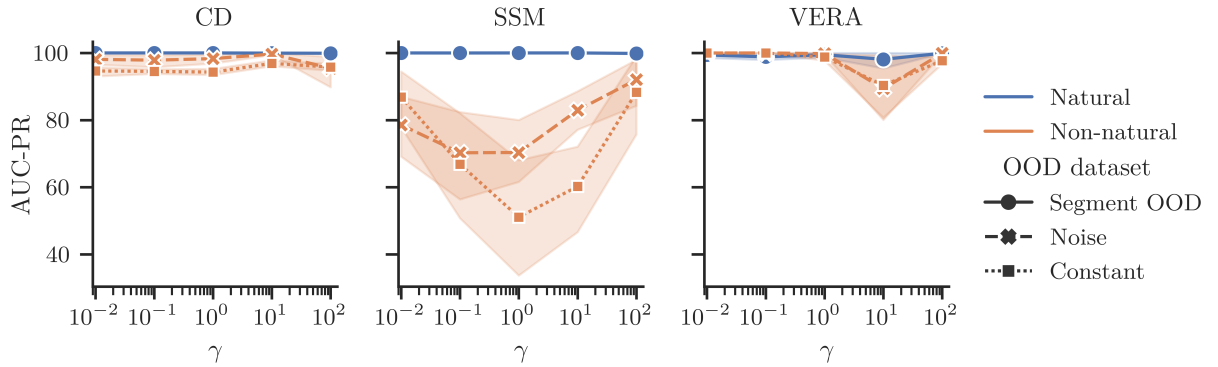
Finally, we report the full OOD detection results in Table A.3 for the experiment where we enforce the asymptotic convergence of the energy using Theorem 1 in Section 4.2.2. We add the baselines of SSM training (SSM) and SSM training with additional supervision (SSM-S) for reference. As we mentioned before, the asymptotic guarantee leads to surprising improvements on the *natural* datasets.

Table A.2.: AUC-PR for OOD detection on the CIFAR-10 dataset.

Model	OOD dataset Score	SVHN	LSUN	CIFAR-100	CelebA	Textures	Noise	Constant	OODomain
CE Baseline	$\max p(y \mathbf{x})$	87.54 ± 0.11	85.94 ± 0.53	98.66 ± 0.14	91.9 ± 0.41	98.4 ± 0.9	38.12 ± 0.56	94.08 ± 0.52	95.72 ± 0.74
EnergyOOD	$p_\theta(\mathbf{x})$	84.34 ± 0.34	85.3 ± 4.15	99.94 ± 0.08	91.75 ± 1.45	100.0 ± 0.0	76.8 ± 7.21	98.01 ± 1.71	93.38 ± 5.67
Ensemble	Variance	56.33	67.99	34.7	61.46	68.35 ± 31.47	99.62	56.45	41.3
JEM	$p_\theta(\mathbf{x})$	55.67 ± 1.14	79.66 ± 2.73	31.96 ± 0.07	65.66 ± 1.75	31.13 ± 0.38	31.45 ± 0.37	60.64 ± 2.56	42.61 ± 5.1
MC Dropout	Variance	87.43 ± 0.02	89.98 ± 0.93	89.54 ± 0.05	90.67 ± 0.03	92.31 ± 0.27	36.37 ± 0.71	89.9 ± 0.15	89.99 ± 0.53
OE	$\max p(y \mathbf{x})$	87.55 ± 0.14	89.4 ± 0.34	99.17 ± 0.99	92.6 ± 0.39	100.0 ± 0.0	36.18 ± 1.43	93.88 ± 0.17	96.59 ± 0.57
PostNet	$\max p(y \mathbf{x})$	83.34 ± 0.88	89.98 ± 0.5	97.66 ± 1.11	87.49 ± 0.91	99.24 ± 0.24	100.0 ± 0.0	92.1 ± 0.52	91.54 ± 2.43
R-PriorNet	$\mathcal{H}(p(\mu \mathbf{x}, \theta))$	79.41 ± 0.55	79.02 ± 1.59	94.47 ± 0.93	84.42 ± 1.82	100.0 ± 0.0	85.1 ± 11.29	86.91 ± 0.98	77.99 ± 2.37
EPN-M	$\mathcal{H}(p(\mu \mathbf{x}, \theta))$	66.29 ± 15.88	63.98 ± 1.33	83.01 ± 5.52	70.48 ± 11.38	100.0 ± 0.0	100.0 ± 0.0	76.85 ± 12.55	85.16 ± 2.44
	$p_\theta(\mathbf{x})$	53.53 ± 0.97	58.83 ± 0.73	67.31 ± 7.38	54.76 ± 0.23	100.0 ± 0.0	100.0 ± 0.0	65.38 ± 6.66	84.04 ± 3.24
EPN-V	$\mathcal{H}(p(\mu \mathbf{x}, \theta))$	80.07 ± 0.06	87.04 ± 0.2	84.21 ± 5.75	83.77 ± 0.2	100.0 ± 0.0	69.88 ± 3.62	85.8 ± 1.15	73.25 ± 0.71
	$p_\theta(\mathbf{x})$	79.58 ± 0.11	87.22 ± 0.26	78.96 ± 6.87	83.6 ± 0.31	100.0 ± 0.0	30.74 ± 0.04	83.85 ± 1.85	69.18 ± 0.45

Table A.3.: AUC-PR for OOD detection with EBMs trained using SSM. SSM uses plain SSM training, SSM-S uses an additional cross-entropy loss, and SSM-S-A additionally leverages the parameterization with asymptotic guarantee following Theorem 1.

ID	CIFAR-10								FMNIST					
OOD	SVHN	LSUN	CelebA	CIFAR-100	Textures	Noise	Constant	OODomain	KMNIST	MNIST	NotMNIST	Noise	Constant	OODomain
SSM	45.75	52.79	57.72	53.82	48.82	70.23	47.2	68.57	58.98	67.86	57.27	49.5	47.59	76.76
SSM-S	46.54	68.77	57.15	62.71	43.51	64.15	37.83	30.69	93.77	99.22	84.93	33.7	37.52	70.03
SSM-S-A	70.95	68.14	81.93	66.22	76.0	84.23	84.61	100.0	96.51	89.06	89.66	99.69	96.39	100.0

Figure A.1.: AUC-PR for OOD detection for different settings of the weighting hyperparameter γ of the cross entropy objective. Segment is used as the in-distribution dataset.

A. General Addenda

Table A.4.: AUC-PR for OOD detection on the natural datasets when trained on the respective in-distribution dataset.

ID	CIFAR-10					FMNIST			Segment	Sensorless
OOD	CIFAR-100	CelebA	LSUN	SVHN	Textures	KMNIST	MNIST	NotMNIST	OOD	OOD
CE	62.76 \pm 1.46	64.47 \pm 2.44	65.18 \pm 5.79	47.51 \pm 4.58	39.17 \pm 2.28	69.07 \pm 6.73	82.5 \pm 12.27	50.9 \pm 6.73	33.35 \pm 1.82	33.02 \pm 1.32
NF	58.34	74.68	62.99	31.58	50.23	62.22	49.03	93.68	99.12	94.35
CD	50.51 \pm 2.13	43.86 \pm 5.85	54.43 \pm 11.37	60.72 \pm 24.59	76.21 \pm 17.44	50.52 \pm 9.39	31.69 \pm 0.9	76.85 \pm 2.66	98.18 \pm 2.18	72.83 \pm 16.19
CD-E	77.88 \pm 1.61	66.21 \pm 1.94	80.61 \pm 4.26	97.38 \pm 1.15	98.6 \pm 0.56	90.53 \pm 3.38	93.05 \pm 2.88	88.05 \pm 4.5	-	-
CD-S	49.81 \pm 1.15	50.15 \pm 4.24	53.09 \pm 1.04	45.14 \pm 7.55	46.55 \pm 4.37	93.88 \pm 1.44	83.47 \pm 2.93	98.03 \pm 0.53	100.0 \pm 0.0	94.48 \pm 2.11
SSM	53.82 \pm 3.12	57.72 \pm 7.0	52.79 \pm 3.16	45.75 \pm 7.24	48.82 \pm 4.34	58.98 \pm 5.48	67.86 \pm 11.4	57.27 \pm 13.73	79.43 \pm 24.29	67.13 \pm 20.31
SSM-E	84.73 \pm 0.67	78.62 \pm 2.23	89.4 \pm 1.18	74.69 \pm 2.76	69.8 \pm 2.72	97.88 \pm 0.66	95.57 \pm 0.97	96.44 \pm 0.83	-	-
SSM-S	62.71 \pm 0.98	57.15 \pm 2.18	68.77 \pm 4.5	46.54 \pm 3.54	43.51 \pm 2.74	93.77 \pm 1.08	99.22 \pm 0.19	84.93 \pm 2.07	100.0 \pm 0.0	81.99 \pm 21.79
VERA	55.95 \pm 2.68	73.97 \pm 2.63	67.39 \pm 2.57	37.27 \pm 4.66	46.29 \pm 8.1	78.11 \pm 21.05	67.53 \pm 21.63	76.22 \pm 22.11	94.63 \pm 7.22	45.66 \pm 10.55
VERA-E	76.66 \pm 3.23	73.41 \pm 6.68	81.31 \pm 3.92	83.6 \pm 7.45	78.52 \pm 7.98	85.8 \pm 15.18	88.52 \pm 13.91	79.58 \pm 15.61	-	-
VERA-S	61.37 \pm 0.74	85.02 \pm 2.38	58.91 \pm 3.66	38.35 \pm 1.08	36.68 \pm 0.52	98.89 \pm 0.61	99.64 \pm 0.53	97.75 \pm 1.72	99.35 \pm 1.08	90.38 \pm 3.78

Table A.5.: AUC-PR for OOD detection on the non-natural datasets when trained on the respective in-distribution dataset.

ID	CIFAR-10			FMNIST			Segment		Sensorless	
OOD	Constant	Noise	OODomain	Constant	Noise	OODomain	Constant	Noise	Constant	Noise
CE	45.26 \pm 8.8	61.13 \pm 21.02	30.69 \pm 0.0	35.5 \pm 3.08	55.84 \pm 22.32	30.74 \pm 0.11	42.57 \pm 18.3	33.82 \pm 3.14	32.42 \pm 1.04	31.96 \pm 1.28
NF	30.87	83.65	100.0	71.07	98.04	100.0	99.97	100.0	100.0	100.0
CD	58.75 \pm 28.17	100.0 \pm 0.0	58.41 \pm 37.96	70.59 \pm 12.84	100.0 \pm 0.0	100.0 \pm 0.0	96.13 \pm 2.55	95.43 \pm 3.58	100.0 \pm 0.0	100.0 \pm 0.0
CD-E	99.92 \pm 0.07	87.5 \pm 24.31	30.69 \pm 0.0	96.63 \pm 7.53	86.7 \pm 26.75	35.83 \pm 7.8	-	-	-	-
CD-S	31.32 \pm 0.29	98.01 \pm 0.93	70.86 \pm 30.57	71.17 \pm 10.16	97.79 \pm 1.02	100.0 \pm 0.0	94.57 \pm 2.11	98.68 \pm 1.9	99.97 \pm 0.06	99.98 \pm 0.03
SSM	47.24 \pm 15.56	70.28 \pm 31.39	68.57 \pm 25.2	47.57 \pm 15.18	49.45 \pm 21.19	76.76 \pm 21.1	74.86 \pm 23.37	80.35 \pm 17.38	69.66 \pm 6.12	64.81 \pm 17.03
SSM-E	65.64 \pm 3.66	64.5 \pm 4.05	42.74 \pm 6.73	82.51 \pm 4.95	87.54 \pm 2.17	98.49 \pm 1.94	-	-	-	-
SSM-S	37.8 \pm 3.49	64.24 \pm 12.88	30.69 \pm 0.0	37.61 \pm 1.83	33.71 \pm 1.07	70.03 \pm 17.45	51.57 \pm 25.04	70.09 \pm 17.57	37.5 \pm 13.23	41.6 \pm 12.05
VERA	31.51 \pm 0.66	100.0 \pm 0.0	63.48 \pm 34.37	53.24 \pm 22.65	79.34 \pm 27.34	72.42 \pm 37.61	100.0 \pm 0.0	100.0 \pm 0.0	100.0 \pm 0.0	99.88 \pm 0.25
VERA-E	83.95 \pm 8.71	36.19 \pm 4.43	30.69 \pm 0.0	77.82 \pm 21.24	60.28 \pm 10.11	60.29 \pm 28.5	-	-	-	-
VERA-S	31.7 \pm 0.55	45.32 \pm 25.14	92.1 \pm 8.59	36.01 \pm 4.24	33.73 \pm 3.21	100.0 \pm 0.0	99.01 \pm 1.45	99.9 \pm 0.3	100.0 \pm 0.0	100.0 \pm 0.01

Table A.6.: AUC-PR for OOD detection of EBMs with different dimensions of the bottleneck introduced into the WideResNet-10-2 architecture.

Model	ID	CIFAR-10							FashionMNIST						
	OOD Bottleneck	SVHN	LSUN	CelebA	CIFAR-100	Textures	Noise	OODomain	Constant	KMNIST	MNIST	NotMNIST	Noise	OODomain	Constant
CD	0.05	81.29	42.16	42.82	53.09	59.13	100.0	76.77	78.4	65.27	43.26	80.72	100.0	100.0	73.18
	0.10	67.93	48.3	52.71	53.47	61.99	100.0	62.19	70.85	73.8	53.23	83.25	100.0	100.0	78.27
	0.20	77.97	43.8	42.19	51.85	63.53	100.0	85.99	79.71	73.46	51.8	81.2	99.99	100.0	64.49
	1.00	60.72	54.43	43.86	50.51	76.21	100.0	58.41	58.75	50.52	31.69	76.85	100.0	100.0	70.59
SSM	0.05	53.6	49.44	54.06	53.47	43.3	51.57	89.8	67.7	56.79	62.09	49.05	42.48	77.2	46.42
	0.10	52.51	49.4	57.4	51.54	40.74	40.81	87.05	62.91	58.32	69.04	48.75	46.52	65.72	42.82
	0.20	52.69	49.29	59.96	52.37	49.31	49.26	71.39	57.82	62.31	53.76	68.8	67.07	65.84	56.88
	1.00	45.75	52.79	57.72	53.82	48.82	70.28	68.57	47.24	58.98	67.86	57.27	49.45	76.76	47.57
VERA	0.05	33.34	89.65	82.69	55.22	58.13	72.28	86.14	30.92	87.52	80.64	75.22	74.43	100.0	33.09
	0.10	34.52	80.64	79.4	54.44	54.84	45.02	84.56	33.65	86.85	85.65	66.3	75.58	96.28	31.54
	0.20	33.95	73.29	76.1	54.03	45.01	48.29	73.57	31.31	88.7	89.06	60.7	59.56	100.0	36.01
	1.00	37.27	67.39	73.97	55.95	46.29	100.0	63.48	31.51	78.11	67.53	76.22	79.34	72.42	53.24

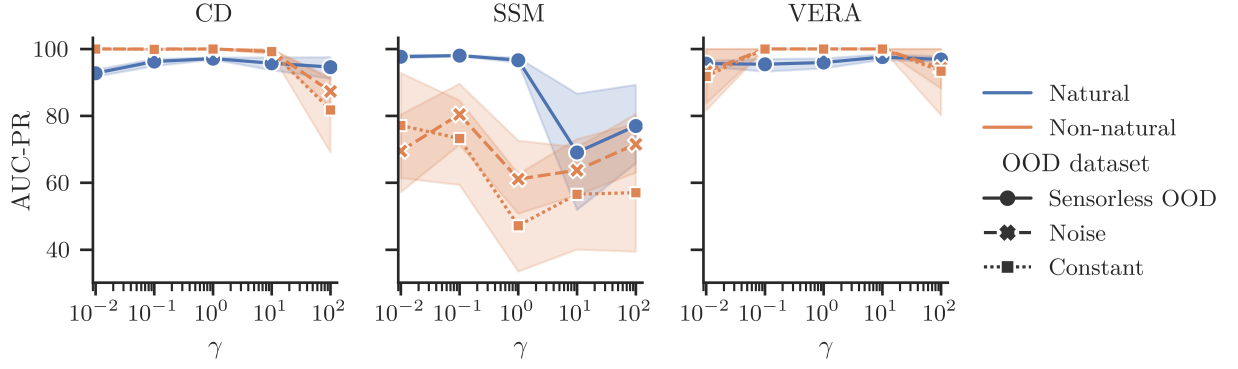


Figure A.2.: AUC-PR for OOD detection for different settings of the weighting hyperparameter γ of the cross entropy objective. Sensorless is used as the in-distribution dataset.

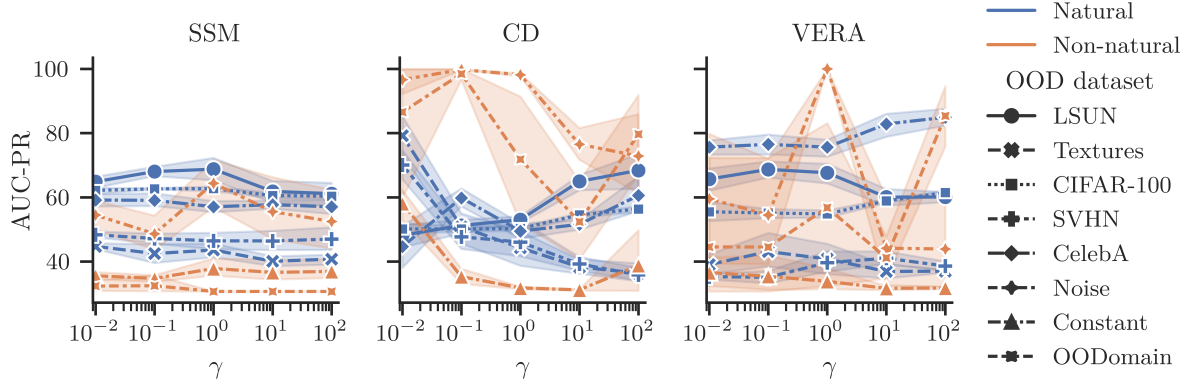


Figure A.3.: AUC-PR for OOD detection for different settings of the weighting hyperparameter γ of the cross entropy objective. CIFAR-10 is used as the in-distribution dataset.

A.4. Other directions

In addition to the work in the main thesis, we pursued several other research directions which do not fit into the existing thesis structure. For completeness, we report the ideas and results in the following.

A.4.1. Noise Contrastive Estimation for Energy-based model training

There are several other methods proposed in the literature for training EBMs based on contrastive learning. Noise Contrastive Estimation (NCE) [GH10] uses a noise distribution for training the EBM. However to be effective, NCE relies on the noise distribution being close to the data distribution. Obviously, this is problematic since we want to estimate the data distribution in the first place.

Instead, Conditional NCE [CG18] conditions the noise distribution on the data samples, thus reducing the amount of assumptions necessary to obtain a noise distribution similar to the data distribution.

We train EBMs with Conditional NCE with the noise distribution set to a Gaussian $N(\mathbf{x} \mid \sigma \mathbb{I}_D)$ centered at the datapoint $\mathbf{x} \in \mathbb{R}^D$ on the CIFAR-10 dataset.

In Table A.7, we report OOD detection results for different settings of σ . We find that Conditional NCE does not yield EBMs with satisfying OOD detection results, especially on SVHN, which are comparable to other EBM training methods on high-dimensional datasets. Therefore, we omitted NCE and Conditional NCE in further experiments.

Table A.7.: AUC-PR for OOD detection with EBMs trained with conditional NCE.

	SVHN	LSUN	Noise	OODomain
Empirical variance	16.49	68.21	100.00	100.00
$\sigma = 1.0$	17.68	67.68	100.00	100.00
$\sigma = 0.1$	19.52	82.43	100.00	99.08
$\sigma = 0.0001$	22.95	64.24	100.00	99.83
$\sigma = 10^{-6}$	31.53	54.84	93.79	24.61

A.4.2. Role of transformation in Normalizing Flows for out-of-distribution detection

In addition to the work in Section 4.2, we also investigate certain hypotheses potentially influencing the OOD detection with Normalizing Flows. In particular, we consider dimensionality reduction and the expressiveness of transformations in Normalizing Flows in the following.

Table A.8.: AUC-PR for OOD detection with \mathcal{M} -Flow

Score	CIFAR-100	CelebA	LSUN	SVHN	Textures	Noise
$p_\theta(\mathbf{x})$	53.2	61	75.2	22.5	50	100
$\ x' - x\ $	49.6	51.7	71.4	15.5	45.7	100

Dimensionality reduction. To investigate whether the gap in OOD detection between EBMs and Normalizing Flows is caused by EBMs being able to project to lower dimensions while Normalizing Flows operate in the original data space \mathbb{R}^D , we considered \mathcal{M} -Flows [BC20]. \mathcal{M} -Flows are able to simultaneously learn a lower-dimensional manifold of the data and a density on that manifold with a Normalizing Flow.

For this, Brehmer et al. [BC20] introduce a diffeomorphism between the latent space and data space as

$$f : U \times V \mapsto X, \quad \mathbf{u}, \mathbf{v} \mapsto f(\mathbf{u}, \mathbf{v}) \quad (\text{A.7})$$

They then define the manifold \mathcal{M} as a level set

$$g : U \mapsto \mathcal{M} \subset X, \quad \mathbf{u} \mapsto g(\mathbf{u}) = f(\mathbf{u}, \mathbf{0}) \quad (\text{A.8})$$

For training, they minimize the reconstruction error $\|\mathbf{x} - g(g^{-1}(\mathbf{x}))\|$ to learn the manifold while training a Normalizing Flow on the subspace U with maximum likelihood.

We train \mathcal{M} -Flow on the CIFAR-10 dataset with latent dimension $\dim(U) = 128$ and report OOD detection results using the density $p_\theta(\mathbf{x})$ and reconstruction error $\|\mathbf{x}' - \mathbf{x}\|$ in Table A.8.

Comparing with a vanilla Normalizing Flow, which does not leverage dimensionality reduction before density estimation, in Table 4.6, we observe no significant improvements. This further validates our hypotheses in Section 4.2.1 that the ability of a model to perform dimensionality reduction does not necessarily directly lead to improvements on the task of OOD detection.

Expressiveness of transformations. Another advantage of EBMs over Normalizing Flows is that EBMs are not restricted in their transformations. As introduced in Section 2.3.1, Normalizing Flows rely on invertible transformations where the determinant of the Jacobian $\frac{\partial f}{\partial \mathbf{z}}$ is easy to compute, reducing the expressiveness of individual transformations. We hypothesize that the lower expressiveness reduces the capability of Normalizing Flows to fit the true density, in turn worsening OOD detection.

Table A.9.: Log-likelihood of Normalizing Flow models on different datasets. Rows with * denote log-likelihoods estimated with numerical integration.

Model	3-Gaussians	Two Moons	Checkerboard	Swiss Roll
NF (Radial)	-2.16	-2.53	-4.23	-4.22
NF (IAF)	-0.88	-2.42	-3.76	-3.69
NF (Planar)	-1.34	-2.42	-3.77	-3.30
iResNet	-1.34	-2.53	-3.95	-4.18
Approx. Flow*	-3.13	-3.34	-4.51	-5.35

We investigate the hypotheses by comparing with Normalizing Flow variants which have less restrictions on individual transformations. Behrmann et al. [Beh+19] propose *iResNet* introducing a ResNet architecture [He+16] with invertible transformations. In particular, iResNet contains general transformations of ResNets, while invertibility is enforced during training.

Additionally, we propose a variant of Normalizing Flows where we add a regularization term on the weight matrices $W \in \mathbb{R}^{D \times D}$ to be orthogonal

$$L_{reg} = \|\mathbb{I}_D - W^T W\|_F \quad (\text{A.9})$$

where $\|\cdot\|_F$ denotes the Frobenius norm. This is based on a similar regularization in Charles et al. [Cha+17]. It holds that W is orthogonal $\Leftrightarrow L_{reg} = 0$. Thus, the Jacobian determinant is given as $|\det(\frac{df}{dz})| \approx 1$ given $L_{reg} \approx 0$ for $f(x) = Wx + b$ and $f^{-1}(z) = W^T z - b$. We call this variant *Approximate Flow* since it does not provide exact likelihoods depending on the convergence of the regularization term L_{reg} . In this model, the individual transformations are also freely specified, however, during training the weight matrices are pushed to be orthogonal. We introduce leaky ReLU activations as non-linearities in between the layers since they are invertible.

We compare against traditional Normalizing Flow models where the transformations are defined in a way such that $\det(\frac{df}{dz})$ is tractable (*Radial*, *IAF*, *Planar*) [RM15; Kin+16]. Further, we consider the two Normalizing Flow models above where the transformations are freely specified (*iResNet*, *Approx. Flow*). For all models, we consider 20 stacked transformations.

In Table A.9, we report the log-likelihood of the test set under the different models. We observe that there is no significant difference between models with restricted and free transformations. In some cases the models with restricted transformations even outperform non-restricted models.

We conclude that the expressiveness of individual transformations is not significant when the overall network is sufficiently deep.

A.4.3. Generating low-entropy samples using SGLD

Hein et al. [HAB19] attempted to fix the issue of overly confident predictions in ReLU networks by adding an additional loss term enforcing high-entropy predictions for samples randomly obtained from a noise distribution covering the domain of the classifier, e.g., $\mathcal{U}(-1, 1)$. We deem this approach to be inefficient since it causes the classifier to be evaluated even in regions outside that training data which might already have high-entropy predictions.

Thus, we propose to extend this approach by guiding the sampling into low-entropy regions. For this, we define the entropy function \mathcal{H} over the domain of the classifier $p_\theta(y | \mathbf{x})$ as

$$\mathcal{H}(p_\theta(y|x)) = - \sum_y p_\theta(y|x) \log p_\theta(y|x) \quad (\text{A.10})$$

We then leverage SGLD to obtain low-entropy samples from \mathcal{H}

$$x_0 \sim p_0(x), \quad x_{i+1} = x_i - \frac{\alpha}{2} \frac{\partial H_\theta}{\partial x_i} + \epsilon, \quad \epsilon \sim N(0, \alpha) \quad (\text{A.11})$$

similar to what we introduced in Section 2.3.2 for EBM training. For our experiments we consider $p_0 = \mathcal{U}(-10, 10)$.

We then follow Hein et al. [HAB19] and maximize the entropy at these positions

$$\max_{\theta} \mathbb{E}_{\mathbf{x} \sim \mathcal{H}} - \sum_y p_\theta(y|\mathbf{x}) \log p_\theta(y|\mathbf{x}) \quad (\text{A.12})$$

as additional loss term.

From Figure A.4, we observe that indeed this additional term can ensure that the model makes confident predictions only close to the training data. However, when considering out-of-domain inputs as it can be seen in Figure A.4c, the confidence again tends to 1 for samples far from the training data resulting in possibly confident wrong predictions.

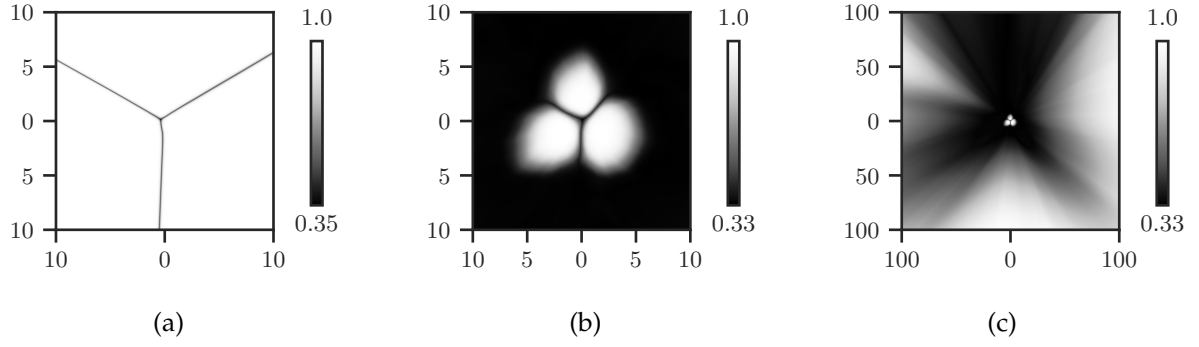


Figure A.4.: (a) Confidence of the cross-entropy model. (b, c) Confidence on two domains for the model trained with additional entropy objective.

List of Figures

1.1. Inference in a classification model for an ID input (<i>car</i>) and OOD input (<i>bird</i>).	2
2.1. Posterior Dirichlet distributions $p(\boldsymbol{\mu} \mid \mathbf{x}, \mathcal{D})$ with desired behavior.	8
2.2. Example density estimate of dataset of images of cars and trucks. Darker shades of blue indicates higher density.	11
3.1. Illustrative example on how the EBM training acts on the posterior $p(\boldsymbol{\mu} \mid \mathbf{x}, \mathcal{D})$ for ID and OOD samples.	22
3.2. Illustrative example on how the KL divergence term acts on the posterior $p(\boldsymbol{\mu} \mid \mathbf{x}, \mathcal{D})$ for a particular sample with target class in the corner of the Dirichlet distribution.	22
3.3. Induced target Dirichlet distribution for the forward KL-divergence.	24
3.4. Visualization of the regions in \mathbb{R}^2 on which the output of a 2-layer ReLU-network is an affine transformation of the input. We use code from Jordan et al. [JLD19] for plotting.	26
4.1. Visualization of the 3-Gaussian dataset with a subset of the dataset samples plotted in white.	29
4.2. Visualization of the confidence of the cross-entropy baseline.	29
4.3. Visualization of distributions of the cross-entropy baseline using the interpretation of logits in W. Grathwohl et al. [Gra+20]. Colors correspond to the different classes.	30
4.4. Visualization of the confidence of EPN.	30
4.5. Visualization of distributions of EPN which also corresponds to the parameters of the predictive Dirichlet distribution as shown in Section 3.1. Colors correspond to the different classes.	31
4.6. Visualization of the differential entropy of EPN on the 3-Gaussians dataset. . .	31
4.7. Variant of the 3-Gaussians dataset with overlapping classes.	32
4.8. Different types of uncertainty estimated by EPN.	32
4.9. Examples for the Gaussian noise, Uniform noise, and Constant images. . . .	33
4.10. $\tilde{p}_{\theta}(\mathbf{x})$ for inputs \mathbf{x} moving away from the training data.	35
4.11. Embeddings and respective density for MNIST vs. KMNIST datasets.	36
4.12. Example of a dataset shift of the <i>fog</i> augmentation for severity 1 to 5.	36
4.13. Accuracy and relative confidence for different models under dataset shift. . .	37
4.14. Example for adversarial attack with PGD on image (a) transformed to image (b). 37	

4.15. Histograms of unnormalized density $\tilde{p}_\theta(\mathbf{x})$ for the clean dataset and with PGD adversarially attacked samples.	38
4.16. Calibration curves of EPN-V before and after temperature scaling.	39
4.17. AUC-PR for OOD detection for different settings of the weighting hyperparameter γ of the cross entropy objective. We use FMNIST as the ID dataset. . .	42
4.18. Unnormalized density $\tilde{p}_\theta(\mathbf{x})$ of inputs with increasing L_2 -norm computed with models trained with SSM and supervision with different γ	43
4.19. Unnormalized density $\tilde{p}_\theta(\mathbf{x})$ of inputs with increasing L_2 -norm for EBMs with the adjusted architecture trained with different values of γ	45
4.20. Example images generated with pooling sizes 2, 3, 4, and 16. Note that the images become smoother with higher pooling sizes.	47
4.21. Density histograms of generated dataset of noise images with different smoothness under different EBMs. Higher pooling corresponds to higher smoothness of the input images as visualized in Figure 4.20.	48
4.22. Comparison of density histogram of ID test set of FMNIST vs. low-level features for unsupervised EBMs with and without bottleneck.	48
4.23. Comparison of samples from the FMNIST dataset.	49
A.1. AUC-PR for OOD detection for different settings of the weighting hyperparameter γ of the cross entropy objective. Segment is used as the in-distribution dataset.	57
A.2. AUC-PR for OOD detection for different settings of the weighting hyperparameter γ of the cross entropy objective. Sensorless is used as the in-distribution dataset.	59
A.3. AUC-PR for OOD detection for different settings of the weighting hyperparameter γ of the cross entropy objective. CIFAR-10 is used as the in-distribution dataset.	59
A.4. (a) Confidence of the cross-entropy model. (b, c) Confidence on two domains for the model trained with additional entropy objective.	64

List of Tables

4.1.	AUC-PR for OOD detection on the Segment dataset.	34
4.2.	AUC-PR for OOD detection on the FMNST dataset.	35
4.3.	AUC-PR for adversarial attacks generated using PGD and FGM.	37
4.4.	Accuracy (\uparrow) and calibration in terms of ECE (\downarrow).	38
4.5.	Ablation experiments on the Sensorless dataset. Gray cells denote significant drops in performance.	40
4.6.	AUC-PR for OOD detection on the respective ID datasets.	42
4.7.	% relative improvement in AUC-PR for OOD detection when using additional supervision during training.	44
4.8.	% relative improvement in AUC-PR for OOD detection with SSM training when using supervision and the parameterization with asymptotic guarantee.	45
4.9.	% relative improvement in AUC-PR for OOD detection when training on embeddings.	46
4.10.	% relative improvement in AUC-PR for OOD detection after introducing bottlenecks.	46
A.1.	AUC-PR for OOD detection on the Sensorless dataset.	56
A.2.	AUC-PR for OOD detection on the CIFAR-10 dataset.	57
A.3.	AUC-PR for OOD detection with EBMs trained using SSM. SSM uses plain SSM training, SSM-S uses an additional cross-entropy loss, and SSM-S-A additionally leverages the parameterization with asymptotic guarantee following Theorem 1.	57
A.4.	AUC-PR for OOD detection on the natural datasets when trained on the respective in-distribution dataset.	58
A.5.	AUC-PR for OOD detection on the non-natural datasets when trained on the respective in-distribution dataset.	58
A.6.	AUC-PR for OOD detection of EBMs with different dimensions of the bottleneck introduced into the WideResNet-10-2 architecture.	58
A.7.	AUC-PR for OOD detection with EBMs trained with conditional NCE.	60
A.8.	AUC-PR for OOD detection with \mathcal{M} -Flow	61
A.9.	Log-likelihood of Normalizing Flow models on different datasets. Rows with * denote log-likelihoods estimated with numerical integration.	62

Bibliography

- [OMa+20] N. O’Mahony, S. Campbell, A. Carvalho, S. Harapanahalli, G. V. Hernandez, L. Krpalkova, D. Riordan, and J. Walsh. “Deep Learning vs. Traditional Computer Vision”. en. In: *Advances in Computer Vision*. Ed. by K. Arai and S. Kapoor. Advances in Intelligent Systems and Computing. Cham: Springer International Publishing, 2020, pp. 128–144. ISBN: 978-3-030-17795-9. DOI: 10/gmfckp.
- [Tor+21] A. Torfi, R. A. Shirvani, Y. Keneshloo, N. Tavaf, and E. A. Fox. *Natural Language Processing Advancements By Deep Learning: A Survey*. 2021. arXiv: 2003.01200 [cs.CL].
- [Gri+20] S. Grigorescu, B. Trasnea, T. Cocias, and G. Macesanu. “A Survey of Deep Learning Techniques for Autonomous Driving”. en. In: *Journal of Field Robotics* 37.3 (2020), pp. 362–386. ISSN: 1556-4967. DOI: 10/gg9ztb.
- [SWS17] D. Shen, G. Wu, and H.-I. Suk. “Deep Learning in Medical Image Analysis”. In: *Annual Review of Biomedical Engineering* 19.1 (2017), pp. 221–248. DOI: 10/gcgmb4.
- [Zha+21] C. Zhang, S. Bengio, M. Hardt, B. Recht, and O. Vinyals. “Understanding Deep Learning (Still) Requires Rethinking Generalization”. In: *Communications of the ACM* 64.3 (Feb. 2021), pp. 107–115. ISSN: 0001-0782. DOI: 10/gh57fd.
- [HAB19] M. Hein, M. Andriushchenko, and J. Bitterwolf. “Why ReLU Networks Yield High-Confidence Predictions Far Away from the Training Data and How to Mitigate the Problem”. In: *Proceedings of the IEEE/CVF Conference on Computer Vision and Pattern Recognition*. 2019, pp. 41–50.
- [LPB17] B. Lakshminarayanan, A. Pritzel, and C. Blundell. “Simple and Scalable Predictive Uncertainty Estimation using Deep Ensembles”. In: *Advances in Neural Information Processing Systems*. Ed. by I. Guyon, U. V. Luxburg, S. Bengio, H. Wallach, R. Fergus, S. Vishwanathan, and R. Garnett. Vol. 30. Curran Associates, Inc., 2017. URL: <https://proceedings.neurips.cc/paper/2017/file/9ef2ed4b7fd2c810847ffa5fa85bce38-Paper.pdf>.
- [Gal16] Y. Gal. “Uncertainty in Deep Learning”. In: 2016.
- [Ruf+21] L. Ruff, J. R. Kauffmann, R. A. Vandermeulen, G. Montavon, W. Samek, M. Kloft, T. G. Dietterich, and K.-R. Müller. “A Unifying Review of Deep and Shallow Anomaly Detection”. In: *Proceedings of the IEEE* (2021), pp. 1–40. ISSN: 0018-9219, 1558-2256. DOI: 10.1109/JPROC.2021.3052449. arXiv: 2009.11732.
- [RM15] D. Rezende and S. Mohamed. “Variational inference with normalizing flows”. In: *International Conference on Machine Learning*. PMLR. 2015, pp. 1530–1538.

- [Nal+19a] E. Nalisnick, A. Matsukawa, Y. W. Teh, D. Gorur, and B. Lakshminarayanan. “Do Deep Generative Models Know What They Don’t Know?” In: *International Conference on Learning Representations*. 2019.
- [KIW20] P. Kirichenko, P. Izmailov, and A. G. Wilson. “Why Normalizing Flows Fail to Detect Out-of-Distribution Data”. In: *Advances in Neural Information Processing Systems*. Ed. by H. Larochelle, M. Ranzato, R. Hadsell, M. F. Balcan, and H. Lin. Vol. 33. Curran Associates, Inc., 2020, pp. 20578–20589.
- [Ver+21] A. Verine, B. Negrevergne, F. Rossi, and Y. Chevaleyre. *On the expressivity of bi-Lipschitz normalizing flows*. 2021. arXiv: 2107.07232 [cs.LG].
- [Lec+06] Y. Lecun, S. Chopra, R. Hadsell, M. Ranzato, and F. Huang. “A tutorial on energy-based learning”. English (US). In: *Predicting structured data*. Ed. by G. Bakir, T. Hofman, B. Scholkopt, A. Smola, and B. Taskar. MIT Press, 2006.
- [Gra+20] W. Grathwohl, K.-C. Wang, J.-H. Jacobsen, D. Duvenaud, M. Norouzi, and K. Swersky. “Your classifier is secretly an energy based model and you should treat it like one”. In: *International Conference on Learning Representations*. 2020.
- [GG16] Y. Gal and Z. Ghahramani. “Dropout as a Bayesian Approximation: Representing Model Uncertainty in Deep Learning”. In: *Proceedings of The 33rd International Conference on Machine Learning*. Ed. by M. F. Balcan and K. Q. Weinberger. Vol. 48. Proceedings of Machine Learning Research. New York, New York, USA: PMLR, June 2016, pp. 1050–1059. URL: <http://proceedings.mlr.press/v48/gal16.html>.
- [MG18] A. Malinin and M. Gales. “Predictive Uncertainty Estimation via Prior Networks”. In: *Advances in Neural Information Processing Systems*. Ed. by S. Bengio, H. Wallach, H. Larochelle, K. Grauman, N. Cesa-Bianchi, and R. Garnett. Vol. 31. Curran Associates, Inc., 2018. URL: <https://proceedings.neurips.cc/paper/2018/file/3ea2db50e62ceefceaf70a9d9a56a6f4-Paper.pdf>.
- [MG19] A. Malinin and M. Gales. “Reverse KL-Divergence Training of Prior Networks: Improved Uncertainty and Adversarial Robustness”. In: *Advances in Neural Information Processing Systems*. Ed. by H. Wallach, H. Larochelle, A. Beygelzimer, F. d’Alché-Buc, E. Fox, and R. Garnett. Vol. 32. Curran Associates, Inc., 2019. URL: <https://proceedings.neurips.cc/paper/2019/file/7dd2ae7db7d18ee7c9425e38df1af5e2-Paper.pdf>.
- [CZG20] B. Charpentier, D. Zügner, and S. Günnemann. “Posterior Network: Uncertainty Estimation without OOD Samples via Density-Based Pseudo-Counts”. In: *Advances in Neural Information Processing Systems*. Ed. by H. Larochelle, M. Ranzato, R. Hadsell, M. F. Balcan, and H. Lin. Vol. 33. Curran Associates, Inc., 2020, pp. 1356–1367. URL: <https://proceedings.neurips.cc/paper/2020/file/0ea690d7059a8de4b48e90f14510391-Paper.pdf>.

- [Blu+15] C. Blundell, J. Cornebise, K. Kavukcuoglu, and D. Wierstra. “Weight Uncertainty in Neural Network”. In: *Proceedings of the 32nd International Conference on Machine Learning*. Ed. by F. Bach and D. Blei. Vol. 37. Proceedings of Machine Learning Research. Lille, France: PMLR, July 2015, pp. 1613–1622. URL: <http://proceedings.mlr.press/v37/blundell15.html>.
- [Mad+19] W. J. Maddox, P. Izmailov, T. Garipov, D. P. Vetrov, and A. G. Wilson. “A Simple Baseline for Bayesian Uncertainty in Deep Learning”. In: *Advances in Neural Information Processing Systems*. Ed. by H. Wallach, H. Larochelle, A. Beygelzimer, F. d’Alché-Buc, E. Fox, and R. Garnett. Vol. 32. Curran Associates, Inc., 2019. URL: <https://proceedings.neurips.cc/paper/2019/file/118921efba23fc329e6560b27861f0c2-Paper.pdf>.
- [RBB18] H. Ritter, A. Botev, and D. Barber. “A Scalable Laplace Approximation for Neural Networks”. In: *International Conference on Learning Representations*. 2018. URL: <https://openreview.net/forum?id=Skdvd2xAZ>.
- [Van+20] J. Van Amersfoort, L. Smith, Y. W. Teh, and Y. Gal. “Uncertainty Estimation Using a Single Deep Deterministic Neural Network”. In: *Proceedings of the 37th International Conference on Machine Learning*. Ed. by H. D. III and A. Singh. Vol. 119. Proceedings of Machine Learning Research. PMLR, July 2020, pp. 9690–9700. URL: <http://proceedings.mlr.press/v119/van-amersfoort20a.html>.
- [BL88] D. Broomhead and D. Lowe. “Radial Basis Functions, Multi-Variable Functional Interpolation and Adaptive Networks”. In: 1988.
- [Liu+20a] J. Liu, Z. Lin, S. Padhy, D. Tran, T. Bedrax Weiss, and B. Lakshminarayanan. “Simple and Principled Uncertainty Estimation with Deterministic Deep Learning via Distance Awareness”. In: *Advances in Neural Information Processing Systems*. Ed. by H. Larochelle, M. Ranzato, R. Hadsell, M. F. Balcan, and H. Lin. Vol. 33. Curran Associates, Inc., 2020, pp. 7498–7512. URL: <https://proceedings.neurips.cc/paper/2020/file/543e83748234f7cbab21aa0ade66565f-Paper.pdf>.
- [vAme+21] J. van Amersfoort, L. Smith, A. Jesson, O. Key, and Y. Gal. *On Feature Collapse and Deep Kernel Learning for Single Forward Pass Uncertainty*. 2021. arXiv: 2102.11409 [cs.LG].
- [Tit09] M. Titsias. “Variational Learning of Inducing Variables in Sparse Gaussian Processes”. en. In: *Artificial Intelligence and Statistics*. PMLR, Apr. 2009, pp. 567–574.
- [HG17] D. Hendrycks and K. Gimpel. “A Baseline for Detecting Misclassified and Out-of-Distribution Examples in Neural Networks”. In: *Proceedings of International Conference on Learning Representations* (2017).
- [LLS18] S. Liang, Y. Li, and R. Srikant. “Enhancing The Reliability of Out-of-distribution Image Detection in Neural Networks”. In: *International Conference on Learning Representations*. 2018. URL: <https://openreview.net/forum?id=H1VGkIxRZ>.

- [Hsu+20] Y.-C. Hsu, Y. Shen, H. Jin, and Z. Kira. “Generalized odin: Detecting out-of-distribution image without learning from out-of-distribution data”. In: *Proceedings of the IEEE/CVF Conference on Computer Vision and Pattern Recognition*. 2020, pp. 10951–10960.
- [HMD19] D. Hendrycks, M. Mazeika, and T. Dietterich. “Deep Anomaly Detection with Outlier Exposure”. en. In: *arXiv:1812.04606 [cs, stat]* (Jan. 2019). arXiv: 1812.04606 [cs, stat].
- [Lee+18a] K. Lee, H. Lee, K. Lee, and J. Shin. “Training Confidence-calibrated Classifiers for Detecting Out-of-Distribution Samples”. In: *International Conference on Learning Representations*. 2018. URL: <https://openreview.net/forum?id=ryiAv2xAZ>.
- [SS18] K. Sricharan and A. Srivastava. *Building robust classifiers through generation of confident out of distribution examples*. 2018. arXiv: 1812.00239 [stat.ML].
- [Lee+18b] K. Lee, K. Lee, H. Lee, and J. Shin. “A Simple Unified Framework for Detecting Out-of-Distribution Samples and Adversarial Attacks”. In: *Advances in Neural Information Processing Systems*. Ed. by S. Bengio, H. Wallach, H. Larochelle, K. Grauman, N. Cesa-Bianchi, and R. Garnett. Vol. 31. Curran Associates, Inc., 2018. URL: <https://proceedings.neurips.cc/paper/2018/file/abdeb6f575ac5c6676b747bca8d09cc2-Paper.pdf>.
- [ZT20] E. Zisselman and A. Tamar. “Deep residual flow for out of distribution detection”. In: *Proceedings of the IEEE/CVF Conference on Computer Vision and Pattern Recognition*. 2020, pp. 13994–14003.
- [Ren+19] J. Ren, P. J. Liu, E. Fertig, J. Snoek, R. Poplin, M. Depristo, J. Dillon, and B. Lakshminarayanan. “Likelihood Ratios for Out-of-Distribution Detection”. In: *Advances in Neural Information Processing Systems*. Ed. by H. Wallach, H. Larochelle, A. Beygelzimer, F. d’Alché-Buc, E. Fox, and R. Garnett. Vol. 32. Curran Associates, Inc., 2019. URL: <https://proceedings.neurips.cc/paper/2019/file/1e79596878b2320cac26dd792a6c51c9-Paper.pdf>.
- [Ser+20] J. Serrà, D. Álvarez, V. Gómez, O. Slizovskaia, J. F. Núñez, and J. Luque. “Input Complexity and Out-of-distribution Detection with Likelihood-based Generative Models”. In: *International Conference on Learning Representations*. 2020. URL: <https://openreview.net/forum?id=SyxIWpVYvr>.
- [Nal+19b] E. Nalisnick, A. Matsukawa, Y. W. Teh, and B. Lakshminarayanan. *Detecting Out-of-Distribution Inputs to Deep Generative Models Using Typicality*. 2019. arXiv: 1906.02994 [stat.ML].
- [CJA19] H. Choi, E. Jang, and A. A. Alemi. *WAIC, but Why? Generative Ensembles for Robust Anomaly Detection*. 2019. arXiv: 1810.01392 [stat.ML].
- [Mor+21] W. Morningstar, C. Ham, A. Gallagher, B. Lakshminarayanan, A. Alemi, and J. Dillon. “Density of states estimation for out of distribution detection”. In: *International Conference on Artificial Intelligence and Statistics*. PMLR. 2021, pp. 3232–3240.

- [DM19] Y. Du and I. Mordatch. “Implicit Generation and Modeling with Energy Based Models”. In: *Advances in Neural Information Processing Systems*. Ed. by H. Wallach, H. Larochelle, A. Beygelzimer, F. d’Alché-Buc, E. Fox, and R. Garnett. Vol. 32. Curran Associates, Inc., 2019. URL: <https://proceedings.neurips.cc/paper/2019/file/378a063b8fdb1db941e34f4bde584c7d-Paper.pdf>.
- [Zha+16] S. Zhai, Y. Cheng, W. Lu, and Z. Zhang. “Deep Structured Energy Based Models for Anomaly Detection”. In: *Proceedings of the 33rd International Conference on International Conference on Machine Learning - Volume 48*. ICML’16. New York, NY, USA: JMLR.org, 2016, pp. 1100–1109.
- [Gra+21] W. S. Grathwohl, J. J. Kelly, M. Hashemi, M. Norouzi, K. Swersky, and D. Duvenaud. “No {MCMC} for me: Amortized sampling for fast and stable training of energy-based models”. In: *International Conference on Learning Representations*. 2021. URL: <https://openreview.net/forum?id=ixpSx09f1k3>.
- [Sch+20] R. Schirrmeister, Y. Zhou, T. Ball, and D. Zhang. “Understanding Anomaly Detection with Deep Invertible Networks through Hierarchies of Distributions and Features”. In: *Advances in Neural Information Processing Systems*. Ed. by H. Larochelle, M. Ranzato, R. Hadsell, M. F. Balcan, and H. Lin. Vol. 33. Curran Associates, Inc., 2020, pp. 21038–21049. URL: <https://proceedings.neurips.cc/paper/2020/file/f106b7f99d2cb30c3db1c3cc0fde9ccb-Paper.pdf>.
- [GBC16] I. Goodfellow, Y. Bengio, and A. Courville. *Deep Learning*. MIT Press, 2016.
- [Sri+14] N. Srivastava, G. Hinton, A. Krizhevsky, I. Sutskever, and R. Salakhutdinov. “Dropout: A Simple Way to Prevent Neural Networks from Overfitting”. In: *The Journal of Machine Learning Research* 15.1 (Jan. 2014), pp. 1929–1958. ISSN: 1532-4435.
- [Bis06] C. Bishop. *Pattern Recognition and Machine Learning*. en. Information Science and Statistics. New York: Springer-Verlag, 2006. ISBN: 978-0-387-31073-2.
- [KL51] S. Kullback and R. A. Leibler. “On Information and Sufficiency”. In: *The Annals of Mathematical Statistics* 22.1 (1951), pp. 79–86. ISSN: 0003-4851. DOI: 10/bm59cw.
- [Jay57] E. T. Jaynes. “Information Theory and Statistical Mechanics”. In: *Physical Review* 106.4 (May 1957), pp. 620–630. DOI: 10/b435gs.
- [Dep+18] S. Depeweg, J.-M. Hernandez-Lobato, F. Doshi-Velez, and S. Udluft. “Decomposition of Uncertainty in Bayesian Deep Learning for Efficient and Risk-sensitive Learning”. In: *Proceedings of the 35th International Conference on Machine Learning*. Ed. by J. Dy and A. Krause. Vol. 80. Proceedings of Machine Learning Research. PMLR, July 2018, pp. 1184–1193. URL: <http://proceedings.mlr.press/v80/depeweg18a.html>.
- [Sha48] C. E. Shannon. “A Mathematical Theory of Communication”. In: *The Bell System Technical Journal* 27.3 (July 1948), pp. 379–423. ISSN: 0005-8580. DOI: 10/b39t.

- [Pim+14] M. A. F. Pimentel, D. A. Clifton, L. Clifton, and L. Tarassenko. “A Review of Novelty Detection”. en. In: *Signal Processing* 99 (June 2014), pp. 215–249. issn: 0165-1684. doi: 10/f5wndg.
- [Sil17] B. W. Silverman. *Density Estimation for Statistics and Data Analysis*. Boca Raton: Routledge, Oct. 2017. isbn: 978-1-315-14091-9. doi: 10.1201/9781315140919.
- [DSB17] L. Dinh, J. Sohl-Dickstein, and S. Bengio. “Density estimation using Real NVP”. In: *International Conference on Learning Representations*. 2017.
- [KD18] D. P. Kingma and P. Dhariwal. “Glow: Generative Flow with Invertible 1x1 Convolutions”. In: *Advances in Neural Information Processing Systems*. Ed. by S. Bengio, H. Wallach, H. Larochelle, K. Grauman, N. Cesa-Bianchi, and R. Garnett. Vol. 31. Curran Associates, Inc., 2018. URL: <https://proceedings.neurips.cc/paper/2018/file/d139db6a236200b21cc7f752979132d0-Paper.pdf>.
- [DKB15] L. Dinh, D. Krueger, and Y. Bengio. *NICE: Non-linear Independent Components Estimation*. 2015. arXiv: 1410.8516 [cs.LG].
- [Hyv05] A. Hyvärinen. “Estimation of Non-Normalized Statistical Models by Score Matching”. In: *The Journal of Machine Learning Research* 6 (Dec. 2005), pp. 695–709. issn: 1532-4435.
- [Son+20] Y. Song, S. Garg, J. Shi, and S. Ermon. “Sliced Score Matching: A Scalable Approach to Density and Score Estimation”. In: *Proceedings of The 35th Uncertainty in Artificial Intelligence Conference*. Ed. by R. P. Adams and V. Gogate. Vol. 115. Proceedings of Machine Learning Research. PMLR, July 2020, pp. 574–584. URL: <http://proceedings.mlr.press/v115/song20a.html>.
- [SK21] Y. Song and D. P. Kingma. *How to Train Your Energy-Based Models*. 2021. arXiv: 2101.03288 [cs.LG].
- [WT11] M. Welling and Y. W. Teh. “Bayesian Learning via Stochastic Gradient Langevin Dynamics”. In: *Proceedings of the 28th International Conference on International Conference on Machine Learning*. ICML’11. Madison, WI, USA: Omnipress, June 2011, pp. 681–688. isbn: 978-1-4503-0619-5.
- [Hin02] G. E. Hinton. “Training Products of Experts by Minimizing Contrastive Divergence”. In: *Neural Computation* 14.8 (Aug. 2002), pp. 1771–1800. issn: 0899-7667. doi: 10.1162/089976602760128018.
- [Tie08] T. Tieleman. “Training Restricted Boltzmann Machines Using Approximations to the Likelihood Gradient”. In: *Proceedings of the 25th International Conference on Machine Learning*. ICML ’08. Helsinki, Finland: Association for Computing Machinery, 2008, pp. 1064–1071. isbn: 9781605582054. doi: 10.1145/1390156.1390290. URL: <https://doi.org/10.1145/1390156.1390290>.
- [Die+19] A. B. Dieng, F. J. R. Ruiz, D. M. Blei, and M. K. Titsias. *Prescribed Generative Adversarial Networks*. 2019. arXiv: 1910.04302 [stat.ML].

- [TR19] M. K. Titsias and F. Ruiz. “Unbiased Implicit Variational Inference”. In: *Proceedings of the Twenty-Second International Conference on Artificial Intelligence and Statistics*. Ed. by K. Chaudhuri and M. Sugiyama. Vol. 89. Proceedings of Machine Learning Research. PMLR, Apr. 2019, pp. 167–176. URL: <http://proceedings.mlr.press/v89/titsias19a.html>.
- [GH10] M. Gutmann and A. Hyvärinen. “Noise-contrastive estimation: A new estimation principle for unnormalized statistical models”. In: *Proceedings of the Thirteenth International Conference on Artificial Intelligence and Statistics*. Ed. by Y. W. Teh and M. Titterton. Vol. 9. Proceedings of Machine Learning Research. Chia Laguna Resort, Sardinia, Italy: PMLR, May 2010, pp. 297–304. URL: <http://proceedings.mlr.press/v9/gutmann10a.html>.
- [CG18] C. Ceylan and M. U. Gutmann. “Conditional Noise-Contrastive Estimation of Unnormalised Models”. In: *Proceedings of the 35th International Conference on Machine Learning*. Ed. by J. Dy and A. Krause. Vol. 80. Proceedings of Machine Learning Research. PMLR, July 2018, pp. 726–734. URL: <http://proceedings.mlr.press/v80/ceylan18a.html>.
- [Liu+20b] W. Liu, X. Wang, J. Owens, and Y. Li. “Energy-based Out-of-distribution Detection”. In: *Advances in Neural Information Processing Systems*. Ed. by H. Larochelle, M. Ranzato, R. Hadsell, M. F. Balcan, and H. Lin. Vol. 33. Curran Associates, Inc., 2020, pp. 21464–21475. URL: <https://proceedings.neurips.cc/paper/2020/file/f5496252609c43eb8a3d147ab9b9c006-Paper.pdf>.
- [BCG19] M. Biloš, B. Charpentier, and S. Günnemann. “Uncertainty on Asynchronous Time Event Prediction”. In: *Advances in Neural Information Processing Systems*. Ed. by H. Wallach, H. Larochelle, A. Beygelzimer, F. d’Alché-Buc, E. Fox, and R. Garnett. Vol. 32. Curran Associates, Inc., 2019. URL: <https://proceedings.neurips.cc/paper/2019/file/78efce208a5242729d222e7e6e3e565e-Paper.pdf>.
- [UC21] D. Ulmer and G. Cinà. *Know Your Limits: Uncertainty Estimation with ReLU Classifiers Fails at Reliable OOD Detection*. 2021. arXiv: 2012.05329 [cs.LG].
- [MBH21] A. Meinke, J. Bitterwolf, and M. Hein. *Provably Robust Detection of Out-of-distribution Data (almost) for free*. 2021. arXiv: 2106.04260 [cs.LG].
- [JLD19] M. Jordan, J. Lewis, and A. G. Dimakis. “Provable Certificates for Adversarial Examples: Fitting a Ball in the Union of Polytopes”. In: *Advances in Neural Information Processing Systems*. Ed. by H. Wallach, H. Larochelle, A. Beygelzimer, F. d’Alché-Buc, E. Fox, and R. Garnett. Vol. 32. Curran Associates, Inc., 2019. URL: <https://proceedings.neurips.cc/paper/2019/file/ae3f4c649fb55c2ee3ef4d1abdb79ce5-Paper.pdf>.
- [DG17] D. Dua and C. Graff. *UCI Machine Learning Repository*. 2017. URL: <http://archive.ics.uci.edu/ml>.
- [XRV17] H. Xiao, K. Rasul, and R. Vollgraf. *Fashion-MNIST: a Novel Image Dataset for Benchmarking Machine Learning Algorithms*. 2017. arXiv: 1708.07747 [cs.LG].

- [Lec+98] Y. Lecun, L. Bottou, Y. Bengio, and P. Haffner. "Gradient-Based Learning Applied to Document Recognition". In: *Proceedings of the IEEE* 86.11 (Nov. 1998), pp. 2278–2324. ISSN: 1558-2256. DOI: 10.1109/5.726791.
- [Bul11] Y. Bulatov. *Machine Learning, Etc: notMNIST Dataset*. Sept. 2011.
- [Cla+18] T. Clanuwat, M. Bober-Irizar, A. Kitamoto, A. Lamb, K. Yamamoto, and D. Ha. "Deep Learning for Classical Japanese Literature". In: *arXiv:1812.01718 [cs, stat]* (2018). DOI: 10.20676/00000341. arXiv: 1812.01718 [cs, stat].
- [Kri09] A. Krizhevsky. *Learning multiple layers of features from tiny images*. Tech. rep. 2009.
- [Yu+16] F. Yu, A. Seff, Y. Zhang, S. Song, T. Funkhouser, and J. Xiao. *LSUN: Construction of a Large-scale Image Dataset using Deep Learning with Humans in the Loop*. 2016. arXiv: 1506.03365 [cs.CV].
- [Hua+20] Y. Huang, C. Qiu, X. Wang, S. Wang, and K. Yuan. "A Compact Convolutional Neural Network for Surface Defect Inspection". In: *Sensors* (2020). DOI: 10.3390/s20071974.
- [Net+11] Y. Netzer, T. Wang, A. Coates, A. Bissacco, B. Wu, and A. Y. Ng. "Reading Digits in Natural Images with Unsupervised Feature Learning". In: *NIPS Workshop on Deep Learning and Unsupervised Feature Learning 2011*. 2011. URL: http://ufldl.stanford.edu/housenumbers/nips2011_housenumbers.pdf.
- [Liu+15] Z. Liu, P. Luo, X. Wang, and X. Tang. "Deep Learning Face Attributes in the Wild". In: *2015 IEEE International Conference on Computer Vision (ICCV)*. 2015, pp. 3730–3738. DOI: 10.1109/ICCV.2015.425.
- [ZK16] S. Zagoruyko and N. Komodakis. "Wide Residual Networks". In: *Proceedings of the British Machine Vision Conference (BMVC)*. Ed. by E. R. H. Richard C. Wilson and W. A. P. Smith. BMVA Press, Sept. 2016, pp. 87.1–87.12. ISBN: 1-901725-59-6. DOI: 10.5244/C.30.87. URL: <https://dx.doi.org/10.5244/C.30.87>.
- [vdMH08] L. van der Maaten and G. Hinton. "Visualizing Data Using T-SNE". In: *Journal of Machine Learning Research* 9.86 (2008), pp. 2579–2605. ISSN: 1533-7928.
- [LCB10] Y. LeCun, C. Cortes, and C. Burges. "MNIST handwritten digit database". In: *ATT Labs [Online]*. Available: <http://yann.lecun.com/exdb/mnist> 2 (2010).
- [HD19] D. Hendrycks and T. Dietterich. "Benchmarking Neural Network Robustness to Common Corruptions and Perturbations". In: *International Conference on Learning Representations*. 2019. URL: <https://openreview.net/forum?id=HJz6tiCqYm>.
- [Mad+18] A. Madry, A. Makelov, L. Schmidt, D. Tsipras, and A. Vladu. "Towards Deep Learning Models Resistant to Adversarial Attacks". In: *International Conference on Learning Representations*. 2018. URL: <https://openreview.net/forum?id=rJzIBfZAb>.
- [GSS15] I. J. Goodfellow, J. Shlens, and C. Szegedy. *Explaining and Harnessing Adversarial Examples*. 2015. arXiv: 1412.6572 [stat.ML].

- [Guo+17] C. Guo, G. Pleiss, Y. Sun, and K. Q. Weinberger. “On Calibration of Modern Neural Networks”. In: *Proceedings of the 34th International Conference on Machine Learning*. Ed. by D. Precup and Y. W. Teh. Vol. 70. Proceedings of Machine Learning Research. PMLR, Aug. 2017, pp. 1321–1330. URL: <http://proceedings.mlr.press/v70/guo17a.html>.
- [FMN16] C. Fefferman, S. Mitter, and H. Narayanan. “Testing the Manifold Hypothesis”. In: *Journal of the American Mathematical Society* 29.4 (2016), pp. 983–1049.
- [LD21] C. L. Lan and L. Dinh. *Perfect Density Models cannot Guarantee Anomaly Detection*. 2021. arXiv: 2012.03808 [cs.LG].
- [KG21] J. Kelly and W. S. Grathwohl. “No Conditional Models for Me: Training Joint EBMs on Mixed Continuous and Discrete Data”. In: *Energy Based Models Workshop - ICLR 2021*. 2021.
- [Nij+19] E. Nijkamp, M. Hill, S.-C. Zhu, and Y. N. Wu. “Learning Non-Convergent Non-Persistent Short-Run MCMC Toward Energy-Based Model”. In: *Advances in Neural Information Processing Systems*. Ed. by H. Wallach, H. Larochelle, A. Beygelzimer, F. d’Alché-Buc, E. Fox, and R. Garnett. Vol. 32. Curran Associates, Inc., 2019. URL: <https://proceedings.neurips.cc/paper/2019/file/2bc8ae25856bc2a6a1333d1331a3b7a6-Paper.pdf>.
- [Miy+18] T. Miyato, T. Kataoka, M. Koyama, and Y. Yoshida. “Spectral Normalization for Generative Adversarial Networks”. In: *International Conference on Learning Representations*. 2018. URL: <https://openreview.net/forum?id=B1QRgziT->.
- [He+16] K. He, X. Zhang, S. Ren, and J. Sun. “Deep Residual Learning for Image Recognition”. In: *2016 IEEE Conference on Computer Vision and Pattern Recognition (CVPR)*. 2016, pp. 770–778. DOI: 10.1109/CVPR.2016.90.
- [Pas+19] A. Paszke, S. Gross, F. Massa, A. Lerer, J. Bradbury, G. Chanan, T. Killeen, Z. Lin, N. Gimelshein, L. Antiga, A. Desmaison, A. Köpf, E. Yang, Z. DeVito, M. Raison, A. Tejani, S. Chilamkurthy, B. Steiner, L. Fang, J. Bai, and S. Chintala. “PyTorch: An Imperative Style, High-Performance Deep Learning Library”. In: *arXiv:1912.01703 [cs, stat]* (Dec. 2019). arXiv: 1912.01703 [cs, stat].
- [BC20] J. Brehmer and K. Cranmer. “Flows for simultaneous manifold learning and density estimation”. In: *Advances in Neural Information Processing Systems*. Ed. by H. Larochelle, M. Ranzato, R. Hadsell, M. F. Balcan, and H. Lin. Vol. 33. Curran Associates, Inc., 2020, pp. 442–453. URL: <https://proceedings.neurips.cc/paper/2020/file/051928341be67dcba03f0e04104d9047-Paper.pdf>.
- [Beh+19] J. Behrmann, W. Grathwohl, R. T. Q. Chen, D. Duvenaud, and J.-H. Jacobsen. “Invertible Residual Networks”. In: *Proceedings of the 36th International Conference on Machine Learning*. Ed. by K. Chaudhuri and R. Salakhutdinov. Vol. 97. Proceedings of Machine Learning Research. PMLR, June 2019, pp. 573–582. URL: <http://proceedings.mlr.press/v97/behrmann19a.html>.

- [Cha+17] R. Q. Charles, H. Su, M. Kaichun, and L. J. Guibas. “PointNet: Deep Learning on Point Sets for 3D Classification and Segmentation”. In: *2017 IEEE Conference on Computer Vision and Pattern Recognition (CVPR)*. 2017, pp. 77–85. doi: 10.1109/CVPR.2017.16.
- [Kin+16] D. P. Kingma, T. Salimans, R. Jozefowicz, X. Chen, I. Sutskever, and M. Welling. “Improved Variational Inference with Inverse Autoregressive Flow”. In: *Advances in Neural Information Processing Systems*. Ed. by D. Lee, M. Sugiyama, U. Luxburg, I. Guyon, and R. Garnett. Vol. 29. Curran Associates, Inc., 2016. URL: <https://proceedings.neurips.cc/paper/2016/file/ddeebdeefdb7e7e7a697e1c3e3d8ef54-Paper.pdf>.